Astronomy Reports, Vol. 47, No. 10, 2003, pp. 797–808. Translated from Astronomicheskiĭ Zhurnal, Vol. 80, No. 10, 2003, pp. 867–878.

Methanol Emission in Distant Protoplanetary Disks

I. E. Val'tts and S. Yu. Lyubchenko

Astro Space Center, Lebedev Physical Institute, Russian Academy of Sciences, Profsoyuznaya ul. 84/32, Moscow, 117997 Russia

Received April 28, 2003; in final form, May 8, 2003

Abstract—Thirty four-frequency line profiles of Class II methanol masers have been analyzed to investigate carefully the coincidences of various spectral features. Data at 6.7, 12.2, 107, and 156.6 GHz have been analyzed. Two clusters of Class II methanol maser lines at 6.7 and 12.2 GHz are observed in the spectra of many sources. These maser-line clusters are located on either side of the thermal methanol lines at 107 and 156.6 GHz. To avoid the effect of amplification in these thermal methanol lines, a similar analysis was performed for 80 sources having both maser emission at 6.7 GHz and thermal CS emission. The relative distributions of the methanol maser lines and the thermal CS line confirm on the basis of richer statistics that the maser lines are located in two clusters on either side of the thermal feature. It is proposed that the two maser-line clusters correspond to two edges of a Keplerian disk. The thermal methanol and CS emission is formed in dense molecular cores, whose centers are coincident with the disk centers. © *2003 MAIK "Nauka/Interperiodica"*.

1. INTRODUCTION

Maser emission of the complex organic molecule CH_3OH (methanol) is observed in star-forming regions. The mechanism giving rise to these masers is not fully understood. However, it is obvious that studies of these methanol lines can yield information about the evolution of the molecular-cloud material and the physical conditions in the interstellar medium, since the masing process is extremely sensitive to changes of these conditions. The methanol molecule has a multitude of allowed transitions, and studies of methanol masers can be carried out at many different frequencies corresponding to these transitions. Multifrequency studies are very profitable from the viewpoint of obtaining homogeneous information about the molecular-cloud fragments in which the masers are formed. Methanol masers are divided into two classes according to the dominant pumping mechanism [1, 2]. The levels of the methanol molecule responsible for Class I maser emission are excited by collisional interactions between the molecules. Class II emission requires the action of an external source of radiation on the ensemble of molecules. The relationship between Class I methanol masers and specific astronomical objects is unclear, whereas Class II methanol masers are associated with the early stages of the formation of protoplanetary systems (see, e.g., [3–5]). In this paper, we will present additional evidence for this hypothesis. Let us proceed to an analysis of the currently available observational data.

2. OBSERVATIONAL DATA

Figure 1 shows a level diagram for methanol. The arrows denote transitions and frequencies corresponding to Class II masers. Note that the A and E states of methanol differ in the mutual orientations of the spins of the hydrogen nuclei with respect to the rotational axis of the molecule, and consequently have different systems of rotational levels. However, astrophysical observations of these molecules can be interpreted jointly, since such differences simply enrich the overall methanol spectrum. Class II methanol masers were first discovered in the 2_0–$3_{-1}E$ transition at 12.2 GHz on the 43-m telescope of the National Radio Astronomy Observatory by Batrla *et al*. [1]. Their intensity typically reaches 3000 Jy. The brightest and most widespread Class II masers radiate in the 5_1–6_0A^+ transition at 6.7 GHz, and were discovered by Menten [6] using the same radio telescope. At present, more than 400 such masers are known [6–11]. The brightest of them, 9.62+0.20, has a peak flux density of about 5000 Jy [6]. Many of these masers radiate at 12.2 GHz (see, e.g., [12]), but maser emission in the J_0–$J_{-1}E$ series of transitions at 157 GHz has been detected in only four [13]. Twenty-five 107-GHz masers have been detected in transitions of A methanol in the J_1–$(J+1)_0A^+$ ladder [14–16]; the methanol emission at 156.6 GHz is mainly thermal [16], and only four masers have been discovered to the present [13, 16].

These observations have been published in plots made on various scales and in tables given in various formats, hindering direct comparisons and analyses.

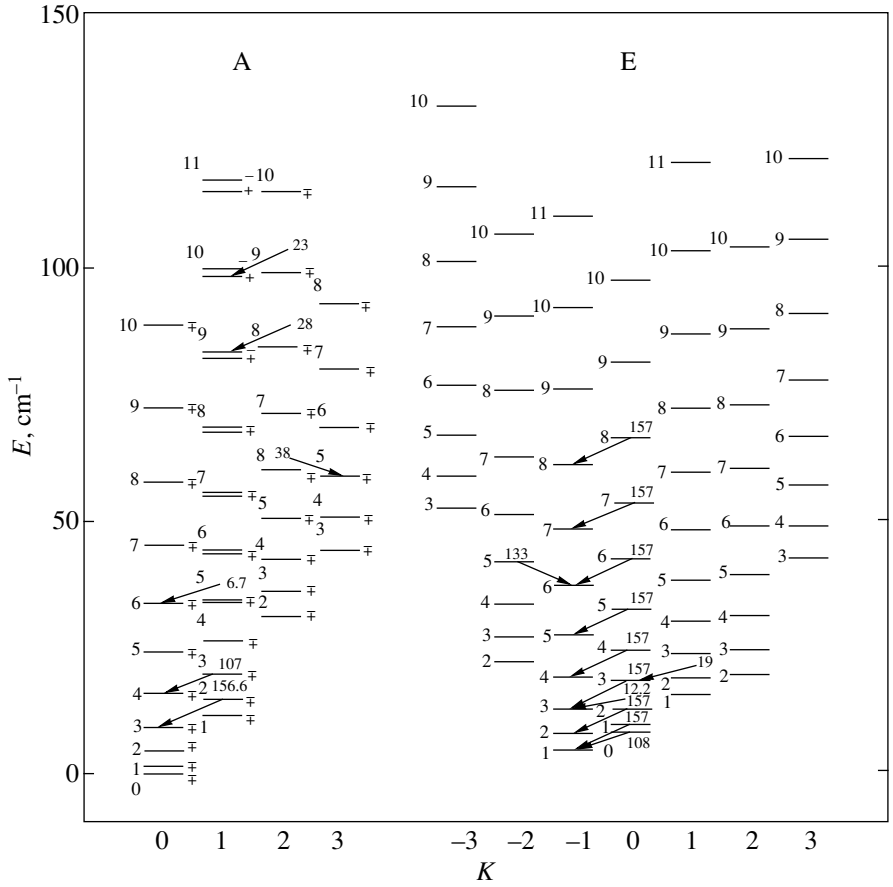

Fig. 1. Level diagram for the methanol molecule and transitions yielding Class II emission. The numbers at the base of the arrows indicate the transition frequencies in GHz.

Therefore, we have taken the most homogeneous data from two surveys, at 6.7 and 12.2 GHz [12] and 107 and 156.6 GHz [16], and replotted the available spectra using a single radial-velocity scale for all 30 sources with line profiles published in [16]. The table lists these 30 sources together with parameters of their thermal 107-GHz methanol lines and CS(2–1) lines. The 107-GHz masers in the table are marked with asterisks. All the four-frequency spectra are presented in electronic form at ftp://ftp.asc.rssi.ru/outgoing/stella; Fig. 2 presents typical examples. In this figure, the horizontal axis plots the line-of-sight velocity in km/s and the vertical axis the flux in Janskys. The transition frequency is given in the upper left corner of each panel. This means of presenting the spectra is fairly common, and is most convenient for careful analyses of the coincidences of individual spectral features at various frequencies.

3. ANALYSIS of FOUR-FREQUENCY METHANOL-LINE PROFILES

It is generally accepted that the thermal lines are formed in the quiescent gas of the parent molecular cloud, and consequently have the same velocity as the unperturbed surrounding medium. It is also known that the velocities of the Class II methanol maser lines differ from the molecular-cloud velocity. This fact is illustrated by our set of spectra. The thermal lines at 107 and 156.6 GHz do not coincide visually with the maser lines at 6.7 and 12.2 GHz, if we consider the line peak velocities. In some cases, the maser lines are located on one side of the thermal lines (at lower velocities in 328.808+0.633, 340.054–0.244, and 9.621+0.196, and at higher velocities in 188.946+0.886, 351.775–0.536, and 12.909–0.260); in some sources (approximately twice as many as display maser lines to either the right or the left), the thermal lines are located between groups of maser features (322.158+0.636, 323.740–0.263, 337.404–0.402, 340.785–0.096, 344.227–0.569, 345.010–1.792, 348.703–1.043, 351.417+0.645, 10.47+0.03, 23.010–0.410, and 35.201–1.736). For the remaining sources in the

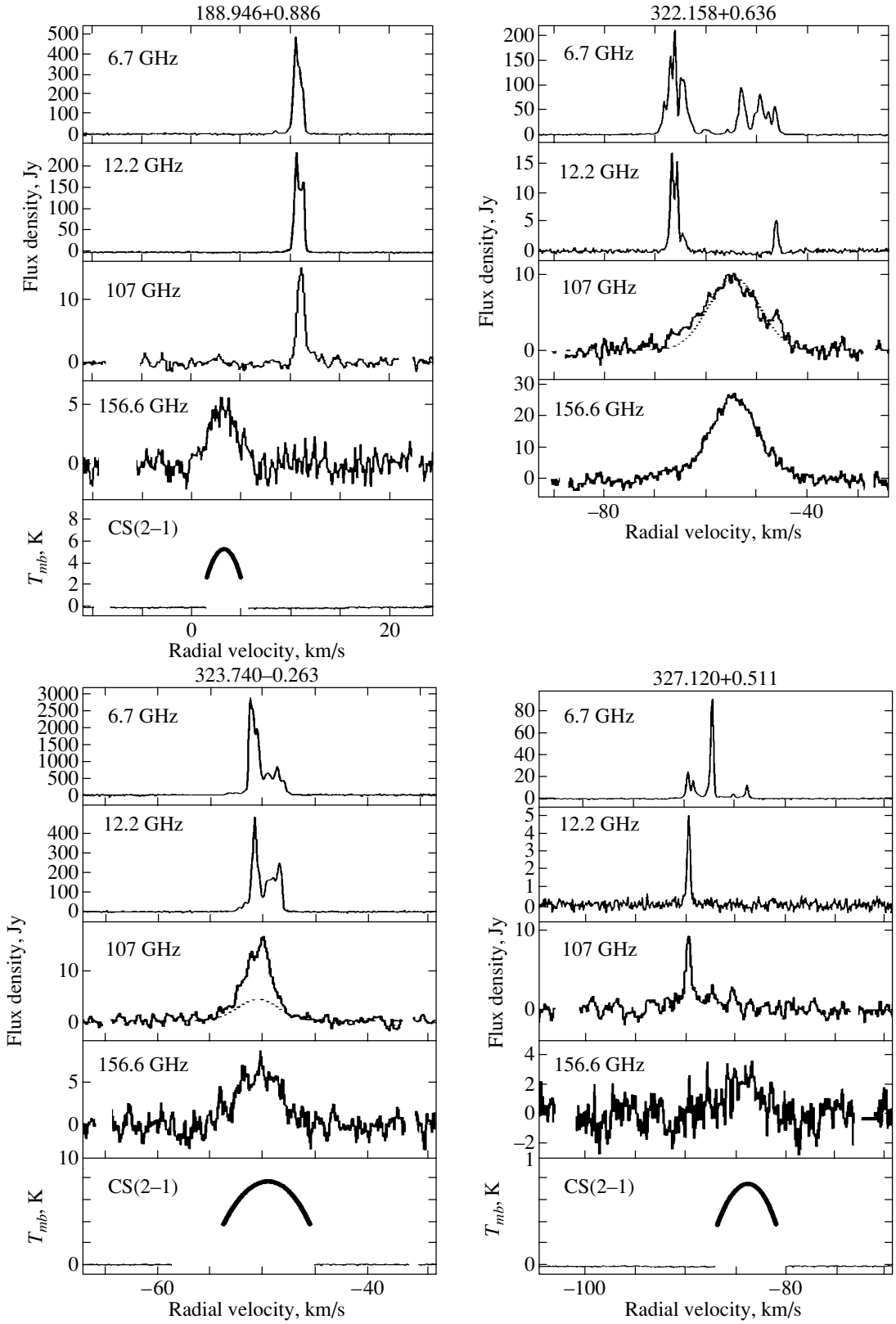

Fig. 2. Four-frequency spectra of the methanol emission. A conditional CS line profile is shown when this line was observed (see text for explanation). Two CS lines are observed toward 345.003−0.223 [17]; the velocity of the weaker line is closer to those of the thermal methanol lines. The CS line parameters for 345.01+1.79 were taken from [18].

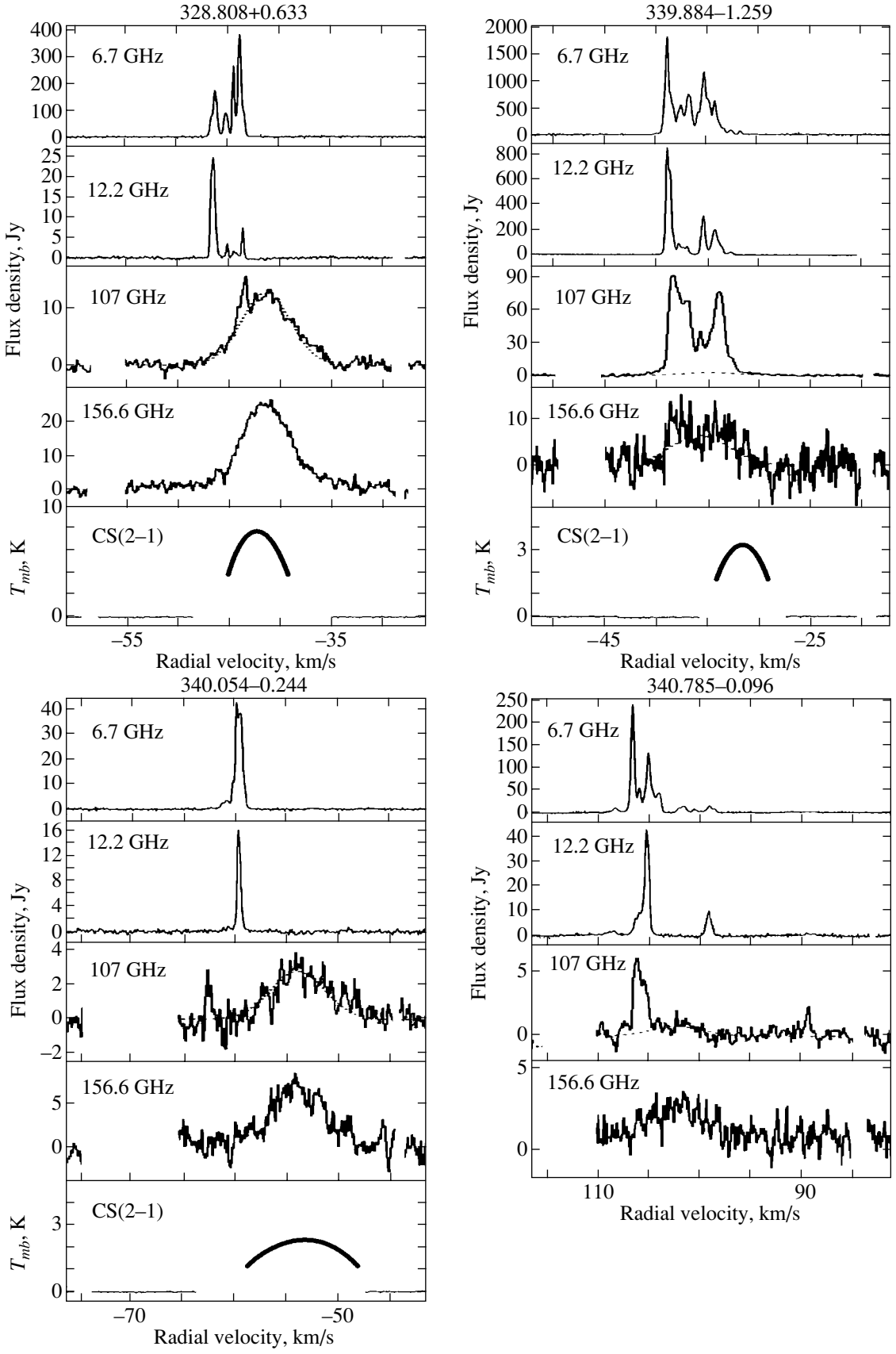
328.808+0.633
6.7 GHz
12.2 GHz
107 GHz
156.6 GHz
CS(2–1)
Flux density, Jy
T_{mb}, K
Radial velocity, km/s
339.884–1.259
340.054–0.244
340.785–0.096

Fig. 2. (Contd.)

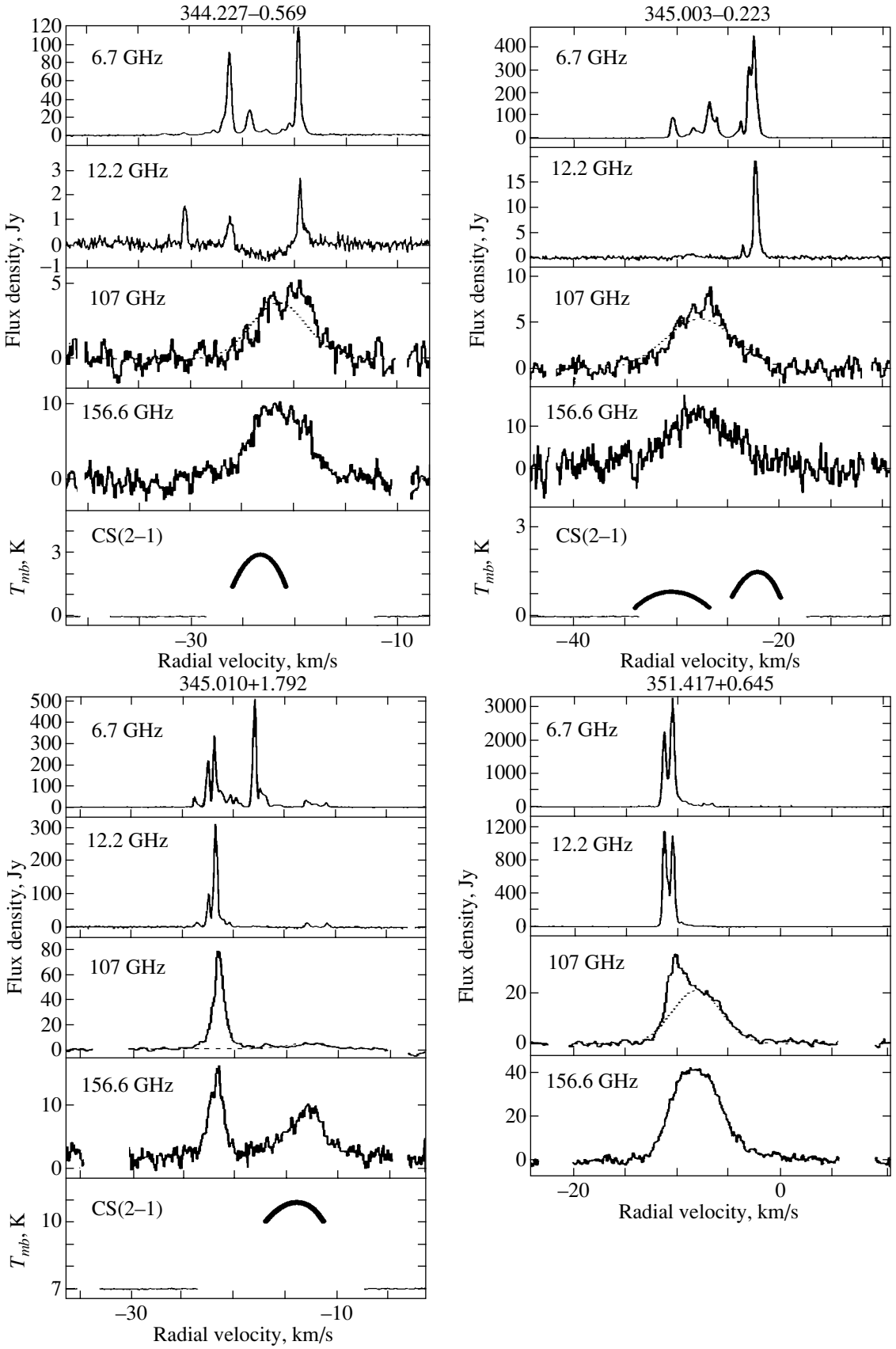
344.227–0.569
345.003–0.223
345.010+1.792
351.417+0.645
6.7 GHz
12.2 GHz
107 GHz
156.6 GHz
CS(2–1)
Flux density, Jy
T_{mb}, K
Radial velocity, km/s

Fig. 2. (Contd.)

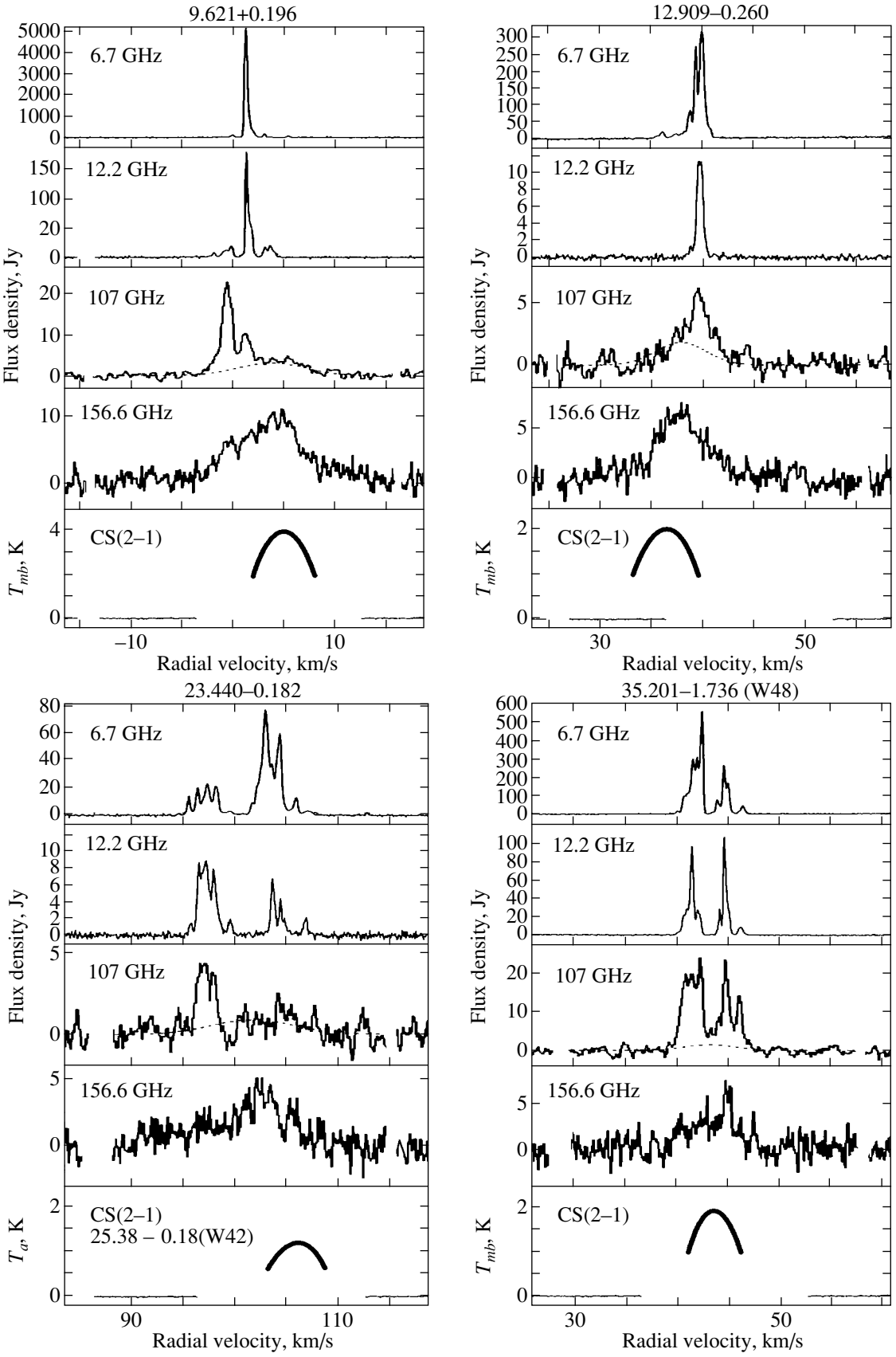
9.621+0.196
6.7 GHz
12.2 GHz
107 GHz
156.6 GHz
CS(2–1)
Flux density, Jy
T_{mb}, K
Radial velocity, km/s
12.909–0.260
23.440–0.182
CS(2–1)
25.38 – 0.18(W42)
T_a, K
35.201–1.736 (W48)

Fig. 2. (Contd.)

Parameters of thermal 107-GHz methanol lines and thermal CS lines for 30 Class II methanol masers.

Source	V_{LSR} of the thermal 107-GHz line [16], km/s	V_{LSR} of the CS(2–1) line [17], km/s	$V_{107} - V_{CS}$, km/s	CS linewidth, km/s
188.946+0.886*	3.1	3.1	0.0	3.7
192.600–0.048*	7.1	–	–	–
310.144+0.760*	–55.5	–55.3	0.2	5.6
318.948–0.196*	–34.0	–	–	–
322.158+0.636	57.2	–	–	–
323.740–0.263*	–50.4	–49.5	0.9	7.8
327.120+0.511*	–84.0	–83.6	0.4	5.5
328.808+0.633*	–41.2	–42.3	1.1	5.5
336.018–0.827*	–47.0	–	–	4.0
337.404–0.402	–40.4	–41.4	1.0	5.9
337.705–0.053	–48.8	–48.1	0.7	8.0
339.884–1.259*	–34.6	–31.6	3.0	4.7
340.054–0.244*	–53.9	–53.1	0.8	11.7
340.785–0.096*	–102.0	–	–	–
344.227–0.569	–21.5	–23.2	1.7	5.3
345.003–0.223*	–27.8	–30.5	2.7	7.4
345.010+1.792*	13.7	–14.0[1]	0.3	4.5
345.504+0.348*	–17.2	–	–	–
348.703–1.0438	–13.4	–	–	–
351.417+0.645*	–8.1	–6.9	1.2	5.8
351.445+0.660	–3.5	–	–	–
351.581–0.353	–95.9	–98.5	2.6	3.9
351.775–0.536	–2.9	–3.4	0.5	7.1
353.410–0.360*	–17.2	–16.7	0.5	9.1
9.621+0.196*	3.6	5.0	1.4	6.2
10.47+0.03	66.5	68.9	2.4	9.0
12.909–0.260*	37.8	36.6	1.2	8.6
23.010–0.410*	77.1	–	–	–
23.440–0.182*	–	–	–	–
35.201–1.736*	43.2	43.9	0.7	5.7

[1] According to [18].

table, the relative arrangement of the thermal and maser features is not obvious (one exception is 345.504+0.348, in which the velocity intervals of the thermal and maser features coincide). In spite of the poor statistics, these spectra suggested to us that the maser lines are actually located not on one or the other side of the thermal lines, but always on both sides, producing two clusters of lines. In this picture, the intensities of the two maser clusters are

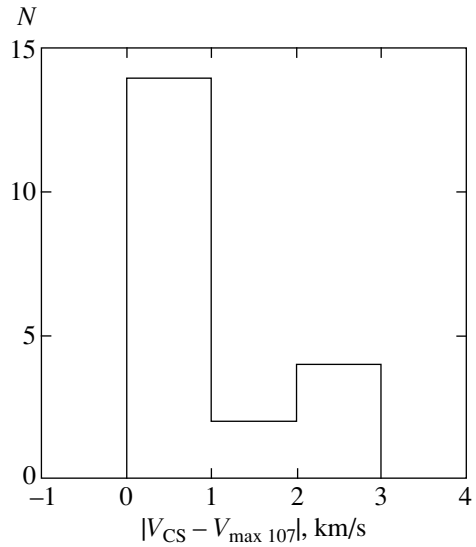

Fig. 3. Distribution of the absolute value of the velocity separation between the CS line peaks and the thermal 107-GHz methanol lines. The data were taken from the catalog of Bronfman *et al.* [17] and Caswell *et al.* [16].

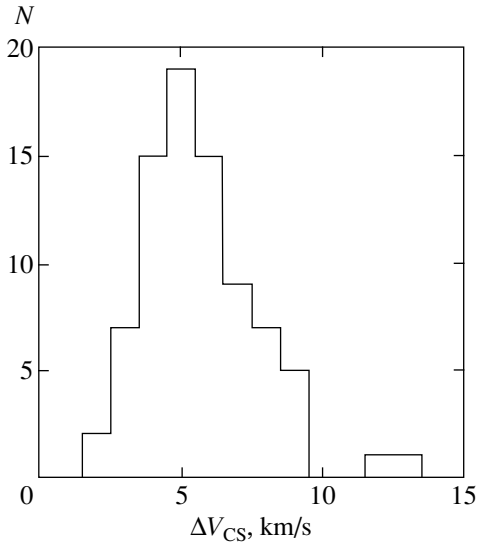

Fig. 4. CS linewidth distribution for 80 Class II methanol masers.

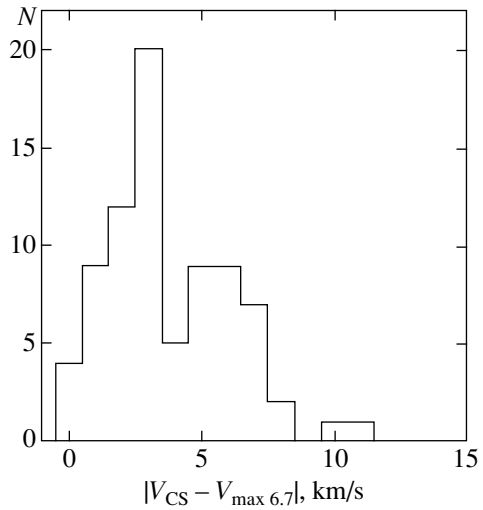

Fig. 5. Distribution of the absolute value of the velocity difference between the CS line and the strongest 6.7-GHz methanol maser feature for 80 sources.

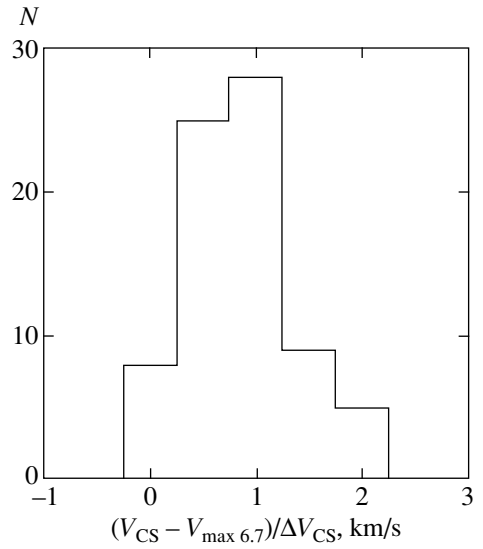

Fig. 6. Same as Fig. 6 but normalized to the CS linewidth.

unequal for some reason, giving rise to the frequently asymmetric appearance of the spectra.

However, we must take into account the fact that broad lines at 107 and 156.6 GHz can be quasi-masers, or groups of weak maser lines. In this case, they do not directly reflect the parameters of the surrounding medium; for example, their radial velocities, like the velocities of the maser lines, can be shifted relative to the quiescent-gas velocity. To eliminate this uncertainty, we used known thermal CS lines to verify the arrangement of the methanol maser lines relative to the thermal lines formed in the stationary gas–dust medium of the molecular clouds. The most complete catalog of CS-line data is that of Bronfman *et al.* [17], and such data are available for 20 of the 30 sources whose spectra we have analyzed. In [17], the line parameters are given only in tabular form, and the conditional CS-line profiles in our graphs have been reconstructed based on these data. The position of the CS peaks, the half-power linewidths, and the line intensities (vertical axis) correspond to their real values. The velocities of the thermal 107- and 156.6-GHz methanol lines and of the CS lines coincide to within about 1 km/s (the mean halfwidth

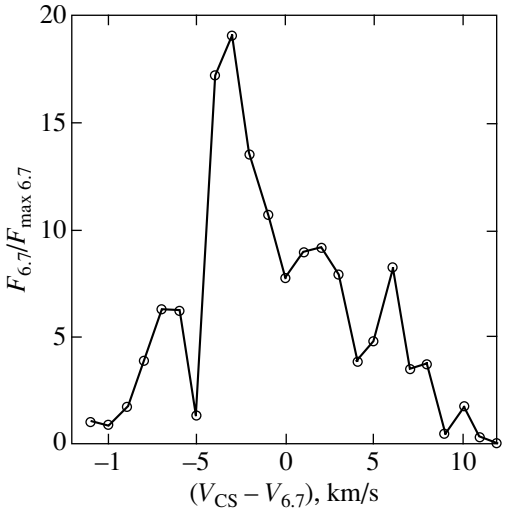

Fig. 7. Total average spectrum of the 6.7-GHz methanol maser emission with respect to the CS line. The line-of-sight velocity of the CS line in each source is taken to be zero. The spectrum was calculated in the velocity interval from −12 to +12 km/s with a step of 1 km/s. The averaging was carried out over the features in each interval. In each spectrum, we took into account features with intensities exceeding the noise in the figures of Caswell *et al.* [12] by a factor of three. In total, we analyzed 386 spectral features for 80 masers from [12].

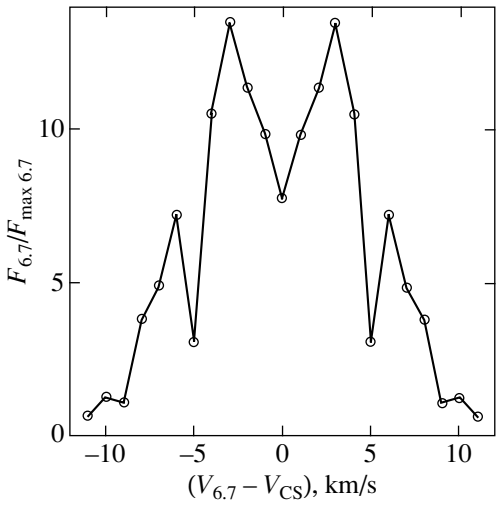

Fig. 8. Transformed total spectrum: the vertical axis is the relative intensity averaged between the positive and negative shifts of the velocities of maser features relative to the CS-line velocities.

of the CS line for these sources is 3.4 km/s); this does not exceed typical errors in the positions of the thermal lines and their widths (table, Fig. 3). The only possible exception is 339.884−1.259, in which the positions of the CS line and of the profile of the quasithermal 156.6-GHz line do not coincide. A considerable amplification in the 107-GHz line is observed in this source, and the 156.6-GHz line may be a blend of multiple maser features. The other two sources for which large differences in the velocities of the 107-GHz thermal line and CS line are observed are 345.003−0.223 and 10.47+0.03; the CS line of 345.003−0.223 is double, indicating that the gas–dust medium has a complex configuration, and 10.47+0.03 itself has a complex structure (see the spectrum in electronic form at the web address noted above). It is more difficult to determine the velocities of more complex profiles.

Although we have noted the presence of two clusters of lines in some sources, and in spite of the observed scatter in the velocities of the maser and thermal features in our spectra, it would be reasonable to suppose that, in a larger sample of sources, the number of sources with maser-line clusters to the right of, to the left of, and coincident with the thermal lines could be the same, with the mean intensities of the clusters also being approximately equal. Of the 135 methanol sources listed by Caswell *et al.* [12], 80 display emission in the CS line. Figure 4 presents the CS half-power linewidths for these 80 sources, while Fig. 5 shows the distribution of the absolute value of the difference between the CS-line velocity and the velocity of the strongest feature in the 6.7-GHz methanol maser line; Fig. 6 is the same as Fig. 5, but with each value of $(|V_{CS} - V_{\max 6.7}|)$ normalized to the corresponding CS linewidth. We can extract the following information from these figures. The average CS linewidth for the 80 sources is 5.52 km/s. In approximately one-third of the sources, the brightest maser feature at 6.7 GHz is separated from the maximum of the CS line by the mean CS-line halfwidth, and for only 5% of the sources do the CS-line velocity and the velocity of the strongest 6.7-GHz maser feature coincide. We can see from Fig. 6 that the separation between the CS-line maximum and the peak of the brightest 6.7-GHz maser feature is equal to either the full width or the halfwidth of the CS line.

We have plotted the total mean spectrum of the 6.7-GHz methanol maser emission (Fig. 7) relative to the CS line [17] for a large sample using the data of [12] as follows. In each of the 80 spectra, the line-of-sight velocity of the CS line was adopted as the zero point. We then calculated for each 6.7-GHz maser feature in a given source the velocity relative to its own conditional zero point. To eliminate the effect of the source distance on the line intensity, we took the intensity of the brightest maser feature in each source to be equal to unity, and the intensities of all the remaining features were measured as fractions of this intensity. We calculated the spectrum at velocities from −12 to +12 km/s in steps of 1 km/s, averaging over the features falling in each interval. In each spectrum, we took into account features whose intensities

exceeded the noise in the figures of Caswell *et al.* [12] by a factor of three. We analyzed 386 spectral features in 80 masers from [12] in this way. The total spectrum does not look uniform or symmetric about the position of the CS line. At lower velocities, at a separation of one CS-line halfwidth from the conditional zero point, there is a maximum exceeding the mean level of the normalized intensities by more than 3σ. At higher velocities, at the same distance from the zero point, this maximum is less pronounced and does not exceed 3σ. Two secondary maxima can be noted at 1.5 CS linewidths on either side of the zero point.

Proceeding from the expected symmetry of the total spectrum relative to the conditional zero point, we added the right-hand and left-hand parts of Fig. 7, divided the resulting intensities by two, and arranged them symmetrically about the conditional zero point. The result is presented in Fig. 8. The addition of the two portions of the spectrum has not smoothed the features visible in Fig. 7. On the contrary, it has become obvious that the maxima and minima in the distribution of the maser features alternate with a period of approximately 2.5 km/s, in multiples of the CS half-power linewidth.

The statistical significance of this result is not high, and the total spectrum we have obtained (Figs. 7, 8) can be considered to be fairly undistinguished with respect to the CS-line position, with a small chance maximum in the distribution of the total relative maser-line intensities at a velocity slightly lower than the conditional zero point.

We will discuss all the features noted in Figs. 3–8 in Section 5. The 6.7-GHz methanol maser features never change their position in the spectrum, though their intensities are variable [12]. Being thermal, the CS lines do not change either their intensities or positions in the spectrum.

4. 107 AND 156.6-GHz MASERS

Before discussing the results of our analysis, let us make some comments concerning the maser features at 107 and 156.6 GHz to supplement the detailed discussion of these masers in [16]. First, according to [16], the coordinates of the strongest 107-GHz masers coincide with those of the 6.7-GHz masers dominating in the spectrum to within 5″. Meanwhile, in the spectra of at least 11 sources—i.e., about 50% of all masers detected at 107 GHz (188.946+0.886, 192.600−0.048, 322.158+0.636, 323.740−0.263, 327.120+0.511, 348.703−1.043, 345.003−0.223, 345.01+1.79, 9.621+0.196, 12.909−0.260, 23.440−0.182)—the dominant emission is observed at 107 GHz; this emission usually corresponds to the weaker 6.7-GHz features but corresponds to the stronger 12.2-GHz features in some cases. In the SEST observations of W48 [16] we analyze here, as well as in Onsala observations of this source [14], a strongly blended feature at 107 GHz that corresponds to a stronger 6.7-GHz maser is brighter, although Mopra observations [15] have yielded the opposite result. However, the stronger 156.6-GHz maser in this source definitely corresponds to a weaker 6.7-GHz feature and a stronger 12.2-GHz feature [5, 13]. Second, based on the general appearance of the spectra of 322.158+0.636, 337.705−0.053 and 344.227−0.569, we can conclude that they display maser amplification, at least at 107 GHz, since the coincidence of the 107-GHz features with features at 6.7 and 12 GHz is obvious. This can be taken to be indirect evidence for amplification at 107 GHz, although Caswell *et al.* [16] consider the presence of 107-GHz masers in these sources to be disputable. In any case, the 107-GHz feature of 322.158+0.636 is virtually identical to the feature at this frequency in 328.808+0.633 with respect to the maser features at other frequencies; however, the verification of such assertions requires observations on more sensitive radio telescopes (which could enable confirmation of the hint of maser amplification at 15.6 GHz in 323.740−0.263 and 344.227−0.569).

Unfortunately, we cannot plot the relationships between the fluxes in the lines at 6.7 and 107 GHz or at 12.2 and 107 GHz, since these data are not given in tabular form for all the spectral features at 6.7 and 12.2 GHz.

The coincidence or lack of coincidence of spectral features at various frequencies may be relevant for the maser pumping and the physical conditions in the maser condensations. However, a detailed discussion of these questions must be based on interferometric observations to determine their mutual spatial arrangement, which is beyond the scope of this paper.

5. DISCUSSION

Let us try to answer the most interesting question: why do the velocities of the maser and thermal lines not coincide? It is obvious that, in most of the cases we have considered (386 maser features in 80 sources), the maser lines and thermal lines do not coincide in radial velocity. The maser lines are concentrated in two clusters at lower and higher velocities relative to the thermal features. Precisely this pattern with two clusters of maser lines is most typical.

If a source displays CS line emission, this implies the presence of a dense molecular core. At what stage of the development of this dense region do the maser velocities begin to differ from the velocity of the core, where the thermal methanol and CS lines continue to form? Does the fact that the velocities of the thermal

features lie between those of the maser features imply that the CS sources are spatially located between the masers, i.e., that there exist favorable conditions for pumping at the CS line halfwidth, although the masers remain fixed relative to the dense core? Or are the masers accelerated when they become masers? In other words, are the masers revolving around the dense cores or flying in all directions? To answer these questions, we must have a model for the source and high-angular-resolution observations of the relative positions of the maser condensations relative to each other and to the dense core.

Slysh *et al*. [4] have discussed the hypothesis that the maser lines are formed in the atmospheres of protoplanets revolving around protostars or very young stars, whose emission maintains the complex pumping of the molecular levels. The locations of such pumping centers were not specifically identified, but they were assumed to be in some obvious region, such as a nearby young ultracompact HII region associated with the masers. Many authors (see, e.g., [21]) have discussed the possibility that a protostar or very young star may be concealed by a dust envelope, and manifest itself only as the invisible center of an ultracompact HII region and a source of maser pumping. Our analysis of maser and thermal spectra has shown that, if maser condensations associated with the atmospheres of protoplanets revolve around some object embedded in a dense molecular cocoon, we can determine the velocity of this cocoon. In this picture, the velocities of the maser and thermal emission are correlated; the velocities of the maser features represent the Keplerian velocities of the orbital motion, whereas the cocoon radiating the thermal methanol and CS lines represents the center of mass of the maser sources + dense molecular core system. In this situation, the presence of two clusters of maser lines (on either side of the thermal feature) is due to maser emission on opposite parts of the orbit. If each maser feature is formed in the atmosphere of a particular protoplanet and each protoplanet has its own orbit, we can imagine a model in which the maser features with higher velocities are closer to the system's center, and vice versa. In an alternative model, the protoplanets revolve in one ring, with the spectrum of methanol maser lines reflecting the projections of the positions of the protoplanets in their orbits onto the line connecting the system's center and the tangent to the ring made by the line of sight. In this case, the spectral feature farthest from the thermal line will correspond to the most distant part of the ring, i.e., to the ring's size.

These models have been analyzed in detail by Norris *et al*. [3] and Minier *et al*. [19]. The asymmetry of the intensity distributions for the total spectrum presented in Fig. 7 can be explained by the fact that conditions in which the maser emission is beamed toward the observer, rather than in the opposite direction, or in which the line-of-sight motion of the masers toward the observer leads to amplification, are preferential for an external observer, i.e., the pumping conditions can have preferential directions. If the thermal lines were not associated with dense cores, which play the role of central bodies and centers of symmetry, the total spectrum of the maser and thermal lines for a large sample of spectral features should have a smoother appearance, and should not contain peaks and minima in any interval, including the region of the CS line. The quasiperiodicity of the total spectrum and the intensity minimum at the simulated CS-line position may provide indirect evidence that we have distinguished the dense cores relative to the maser condensations, while the location of the methanol feature relative to the thermal CS line serves as a demonstration of its maser nature.

6. CONCLUSIONS

Our analysis and comparison of the maser and thermal methanol emission at 6.7, 12, 107, and 156.6 GHz leads us to the following conclusions.

(1) In many sources, two clusters of Class II methanol maser lines at 6.7 and 12 GHz are observed in the spectra.

(2) These clusters of maser lines are located on either side of the thermal methanol lines at 107 and 156.6 GHz.

(3) Analysis of the positions of the thermal CS line has shown that the velocities of this line and those of the thermal methanol lines coincide.

(4) The relative distribution of the methanol maser lines and thermal CS lines confirms based on richer statistics that the maser lines are located in two clusters about the thermal feature.

(5) We have suggested that the two clusters of maser lines correspond to two edges of a Keplerian disk.

(6) Like the CS lines, the thermal methanol emission is formed in dense molecular cores, whose centers coincide with the centers of these disks.

ACKNOWLEDGMENTS

The authors are grateful to V.I. Slysh for useful discussions. This work was partially supported by the Russian Foundation for Basic Research (project code 01-02-16902), a CRDF grant (RP1-2392-MO-02), and the Program of the Physical Sciences Division of the Russian Academy of Sciences "Extended Objects in the Universe." The work was carried out as part of the preparation of a program of observations of masers in star-forming regions on the Kalyazin Radio Telescope.

REFERENCES

1. W. Batrla, H. E. Matthews, K. M. Menten, and C. M. Walmsley, Nature **326**, 49 (1987).
2. K. M. Menten, in *Proceedings of Third Haystack Observatory Conference on Atoms, Ions and Molecules*, Ed. by A. D. Hashick and P. T. P. Ho (Astronomical Society of the Pacific, San Francisco, 1991), p. 119.
3. R. P. Norris, S. E. Byleveld, P. J. Diamond, *et al.*, Astrophys. J. **508**, 275 (1998).
4. V. I. Slysh, I. E. Val'tts, S. V. Kalenskiĭ, and G. M. Larionov, Astron. Zh. **76**, 751 (1999) [Astron. Rep. **43**, 657 (1999)].
5. I. E. Val'tts and S. Yu. Lyubchenko, Astron. Zh. **79**, 328 (2002) [Astron. Rep. **46**, 293 (2002)].
6. K. M. Menten, Astrophys. J. **380**, L75 (1991).
7. G. C. MacLeod, M. J. Gaylard, and G. D. Nicolson, Mon. Not. R. Astron. Soc. **254**, 1P (1992).
8. M. J. Gaylard and G. C. MacLeod, Mon. Not. R. Astron. Soc. **262**, 43 (1993).
9. A. J. Schutte, D. J. van der Walt, M. J. Gaylard, and G. C. MacLeod, Mon. Not. R. Astron. Soc. **261**, 783 (1993).
10. J. L. Caswell, R. A. Vaile, S. P. Ellingsen, *et al.*, Mon. Not. R. Astron. Soc. **272**, 96 (1995).
11. V. I. Slysh, S. V. Kalenskii, I. E. Val'tts, *et al.*, Astron. Astrophys., Suppl. Ser. **134**, 115 (1999).
12. J. L. Caswell, R. A. Vaile, S. P. Ellingsen, and R. P. Norris, Mon. Not. R. Astron. Soc. **1126**, 274 (1995).
13. V. I. Slysh, S. V. Kalenskii, and I. E. Val'tts, Astrophys. J. **442**, 668 (1995).
14. I. E. Val'tts, A. M. Dzura, S. V. Kalenskii, *et al.*, Astron. Astrophys. **294**, 825 (1995).
15. I. E. Val'tts, S. P. Ellingsen, V. I. Slysh, *et al.*, Mon. Not. R. Astron. Soc. **310**, 1077 (1999).
16. J. L. Caswell, Y. Jiyune, R. S. Booth, and D. M. Cragg, Mon. Not. R. Astron. Soc. **313**, 599 (2000).
17. L. Bronfman, L. A. Nyman, and J. May, Astron. Astrophys., Suppl. Ser. **115**, 81 (1996).
18. M. Juvela, Astron. Astrophys., Suppl. Ser. **118**, 191 (1996).
19. V. Minier, R. S. Booth, and J. E. Conway, Astron. Astrophys. **362**, 1093 (2000).
20. G. M. Larionov, I. E. Val'tts, A. Winnberg, *et al.*, Astron. Astrophys., Suppl. Ser. **139**, 257 (1999).
21. J. L. Caswell, Mon. Not. R. Astron. Soc. **289**, 203 (1997).

Translated by G. Rudnitskiĭ

Astronomy Reports, Vol. 47, No. 10, 2003, pp. 809–820. Translated from Astronomicheskiĭ Zhurnal, Vol. 80, No. 10, 2003, pp. 879–890.

Morphology of the Interaction Between the Stream and Cool Accretion Disk in a Semidetached Binary System

D. V. Bisikalo[1], A. A. Boyarchuk[1], P. V. Kaĭgorodov[1], and O. A. Kuznetsov[1,2]

[1] *Institute of Astronomy, Russian Academy of Sciences, ul. Pyatnitskaya 48, Moscow, 109017 Russia*

[2] *Keldysh Institute of Applied Mathematics, Russian Academy of Sciences, Miusskaya pl. 4, Moscow, 125047 Russia*

Received March 5, 2003; in final form, March 14, 2003

Abstract—We analyze heating and cooling processes in accretion disks in binaries. For realistic parameters of the accretion disks in close binaries ($\dot{M} \simeq 10^{-12}$–10^{-7} $M_\odot$/yr and $\alpha \simeq 10^{-1}$–10^{-2}), the gas temperature in the outer parts of the disk is from $\sim 10^4$ to $\sim 10^6$ K. Our previous gas-dynamical studies of mass transfer in close binaries indicate that, for hot disks (with temperatures for the outer parts of the disk of several hundred thousand K), the interaction between the stream from the inner Lagrange point and the disk is shockless. To study the morphology of the interaction between the stream and a cool accretion disk, we carried out three-dimensional modeling of the flow structure in a binary for the case when the gas temperature in the outer parts of the forming disk does not exceed 13 600 K. The flow pattern indicates that the interaction is again shockless. The computations provide evidence that, as is the case for hot disks, the zone of enhanced energy release (the "hot line") is located beyond the disk and originates due to the interaction between the circumdisk halo and the stream. © *2003 MAIK "Nauka/Interperiodica".*

1. INTRODUCTION

In 1999–2002, we developed a three-dimensional gas-dynamical model and used it to study the flow patterns in binary systems [1–14]. These studies indicate that the flow structure is substantially affected by rarefied gas of the intercomponent envelope. In particular, a self-consistent solution does not include a shock interaction between the stream from the inner Lagrange point L_1 and the forming accretion disk (a "hot spot"). The region of enhanced energy release (the "hot line") is located beyond the disk and is due to the interaction between the envelope and the stream. However, these solutions were obtained for temperatures of the outer parts of the accretion disk of 200 000–500 000 K. To check if this behavior is universal, the morphology of the flow must be considered for various disk temperatures.

First, we will study here the interval of plausible temperatures of accretion disks in close binaries. In Section 2, based on an analysis of heating and cooling in accretion disks, we will show that, for realistic parameters of the disks in close binaries, $\dot{M} \simeq 10^{-12}$–10^{-7} $M_\odot$/yr and $\alpha \simeq 10^{-1}$–10^{-2}, the gas temperature in the outer parts of the disk is between 10^4 K and $\sim 10^6$ K. This implies that cool accretion disks can form in some close binaries.

Second, we will consider the morphology of the interaction between streams of matter and cool accretion disks in semidetached binary systems (Sections 3 and 4). The basic problem here is whether the interaction between the stream and the disk remains shockless, as was shown for relatively hot disks [1, 3, 4, 8, 14]. Section 5 presents our main conclusions and a physical basis for the universal nature of the shockless interaction between the stream and disk.

2. HEATING AND COOLING IN ACCRETION DISKS

In this section, we consider the temperature of an accretion disk for various accretion rates, i.e., the dependence $T(\dot{M})$.

2.1. Basic Equations

The vertical structure of an accretion disk is specified by the balance between the vertical component of the gravitational force and the (vertical) pressure gradient, which, in turn, is specified by the balance between heating and cooling of the gas. The heating is associated with viscous dissipation of kinetic energy, and also with bulk radiative heating, which, in turn, is specified by the radiation of the central object. Cooling is brought about by several mechanisms: bulk radiative cooling, radiative heat conduction, and convection. Assuming that advective terms

1063-7729/03/4710-0809$24.00

and terms associated with adiabatic heating or cooling are small, the steady-state energy equation

$$Q^+ - Q^- = 0$$

can be written as follows.

(1) For the optically thin case, when Q^+ is specified by bulk radiative heating and viscous heating and Q^- is determined by bulk radiative cooling,

$$Q^+_{visc}(\rho, T) + n^2 \left[\Gamma(T, T_{wd}) - \Lambda(T)\right] = 0. \quad (1a)$$

Here, $\Gamma(T, T_{wd})$ is the radiative-heating function, which depends on the gas temperature T and the temperature of the central object T_{wd}, $\Lambda(T)$ is the radiative-cooling function, and $Q^+_{visc}(\rho, T)$ is the viscous heating.

(2) For the optically thick case, Q^+ is specified by viscous heating, while Q^- is specified by radiative heat conduction[1] and convection in the vertical direction:

$$Q^+_{visc}(\rho, T) - \frac{\partial F_{rad}}{\partial z} - \frac{\partial F_{conv}}{\partial z} = 0. \quad (1b)$$

Here, F_{rad} and F_{conv} are the radiative and convective energy fluxes.

To determine the functions in (1a) and (1b), we will need

—the equation of continuity

$$-\dot{M} = 2\pi \int r\rho v_r \mathrm{d}z = \mathrm{const}, \quad (2)$$

—the equation of angular-momentum balance $\lambda \equiv r^2\Omega_K$ in the radial direction

$$\frac{\partial}{\partial r}\left(r\rho v_r \lambda\right) = \frac{\partial}{\partial r}\left(\nu\rho r^2 \frac{\partial \Omega_K}{\partial r}\right), \quad (3)$$

from which it follows that

$$|v_r| = -\nu \frac{\partial \Omega_K}{\partial r}\Omega_K^{-1} r^{-1} \simeq \nu r^{-1}, \quad (4)$$

—and the viscous heating

$$Q^+_{visc} = \rho\nu\left(r\frac{\partial \Omega_K}{\partial r}\right)^2. \quad (5)$$

Here, $\dot{M}$ is the accretion rate, $\Omega_K = \sqrt{GM/r^3}$ is the angular velocity of the Keplerian rotation of the disk, M is the mass of the central object, G is the gravitational constant, ρ is the density, v_r is the radial velocity, and ν is the coefficient of kinematic viscosity. Note that the molecular viscosity cannot provide the necessary dissipation, and dissipation processes are usually considered to be associated with turbulent or magnetic viscosity.

To determine the vertical pressure gradient, we will use the equation of hydrostatic balance in the vertical direction

$$\frac{1}{\rho}\frac{\partial P}{\partial z} = \frac{\partial}{\partial z}\left(\frac{GM}{\sqrt{r^2 + z^2}}\right) \simeq -\Omega_K^2 z, \quad (6)$$

as well as the equation of state of an ideal gas with radiation

$$P = \rho\mathcal{R}T + {}^1/_3 aT^4.$$

Here, P is the pressure, T is the temperature, $\mathcal{R}$ is the gas constant, and a is the radiation constant. All equations are given in cylindrical coordinates, (r, z).

2.2. The Solution Method

To determine the dependence $T(\dot{M})$, we will use (2) and (4) together with the expression for the viscosity coefficient ν. We will use the formula for ν suggested by Shakura [15], $\nu = \alpha c_s H$, where H is the height of the disk and $c_s \simeq \sqrt{\mathcal{R}T + {}^1/_3 aT^4/\rho}$ is the sound speed. If we neglect the z dependence of the density and use $\bar{\rho}$ averaged over the height (further, we will denote this quantity simply as ρ), the integration of (6) yields the height of the disk H:

$$H = c_s \Omega_K^{-1}.$$

We will determine c_s from the temperature in the equatorial plane of the disk, $z = 0$. This approach is sufficiently correct for our purposes due to the uncertainty in the parameter α. As a result, we obtain an equation relating $\dot{M}$, $T|_{z=0}$, and ρ for the specified r and α,

$$\dot{M} = 2\pi\alpha\Omega_K^{-2}\rho c_s^3 = 2\pi\alpha\Omega_K^{-2} \times \left(\mathcal{R}T\rho^{2/3} + {}^1/_3 aT^4\rho^{-1/3}\right)^{3/2}. \quad (7)$$

This equation reduces to a cubic equation in the variable $\rho^{1/3}$, and its solution has two branches: one with a negative real root and two complex ones, and one with three real roots, one of which is negative. Only positive real roots for the density are physically meaningful. For such roots to exist, the following condition must be satisfied:

$$\dot{M} > \frac{\sqrt{3}\pi\sqrt{\mathcal{R}}a\alpha T^{9/2}}{\Omega_K^2}, \quad (8)$$

which yields the minimum accretion rate for the given T, r, and α. When deriving this condition, we used the equation of state taking into account the radiation pressure.

[1] We neglect molecular heat conduction since it is very small compared with the radiative heat conduction.

This estimate can also be written in the form

$$T < 7 \times 10^5 \left(\frac{r}{R_{wd}}\right)^{-2/3} \times \left(\frac{\dot{M}}{10^{-9}\ M_\odot/\mathrm{yr}}\right)^{2/9} \times \left(\frac{\alpha}{0.1}\right)^{-2/9}\ \mathrm{K},$$

where $R_{wd} = 10^9$ cm is the radius of the accretor (white dwarf).

Let us consider the condition (8) for the outer parts of the accretion disk. Let us take $r = A/5$, where A is the distance between the components of the binary ($A = 1.42\ R_\odot$), which corresponds to the situation for the dwarf nova IP Peg; as a result, we obtain

$$\dot{M} > 10^{-9} \left(\frac{T}{10^5\ \mathrm{K}}\right)^{9/2} \left(\frac{\alpha}{0.1}\right) \quad M_\odot/\mathrm{yr}. \qquad (9)$$

If (8) is satisfied, the roots of Eq. (7) relating ρ, T, and $\dot{M}$ for a given r and α can be written

$$\rho = (\mathcal{R}T)^{-3/4} \left(\frac{\dot{M}\Omega_K^2}{2\pi\alpha}\right) \times \sin^3\left({}^1\!/_3 \arcsin\left(\sqrt{\mathcal{R}} a T^{9/2} \frac{2\pi\alpha}{\dot{M}\Omega_K^2}\right)\right),$$

$$\rho = (\mathcal{R}T)^{-3/4} \left(\frac{\dot{M}\Omega_K^2}{2\pi\alpha}\right) \times \cos^3\left({}^1\!/_3 \arcsin\left(\sqrt{\mathcal{R}} a T^{9/2} \frac{2\pi\alpha}{\dot{M}\Omega_K^2}\right) + \frac{\pi}{6}\right)$$

(for simplicity, we have omitted numerical factors $\frac{\sqrt{3}}{2} \simeq 1$). The first of these corresponds to disks with dominant radiation pressure ($\beta = {}^1\!/_3 aT^4/\rho\mathcal{R}T > 1$) and the second to disks with dominant gas pressure ($\beta < 1$).

These formulas describe the two branches of the two-parameter dependence $\rho(\dot{M}, T)$. To calculate the dependence $T(\dot{M})$, we must use the additional heat balance equation (1). As follows from Section 2.1, the form of (1) depends on the optical depth of the disk, which, accordingly, must be calculated.

2.3. Optical Depth

The optical depth τ is specified by the product of the absorption coefficient κ, the density, and the geometrical depth of the layer, $\tau = \kappa\rho l$. For disk accretion, the basic parameter is the ratio of the geometrical depth of the layer where $\tau = 1$ and the height of the disk: $l^{\tau=1}/H$. After simple manipulation, we obtain

$$\frac{l^{\tau=1}}{H} = \frac{2\pi\alpha}{\kappa\dot{M}} c_s^2 \Omega_K^{-1}. \qquad (10)$$

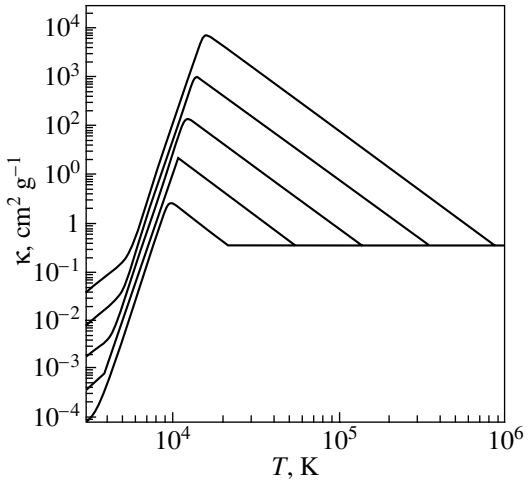

Fig. 1. The $\kappa(T)$ dependence for $n = 10^{18}$ cm^{-3}, $n = 10^{17}$ cm^{-3}, $n = 10^{16}$ cm^{-3}, $n = 10^{15}$ cm^{-3}, and $n = 10^{14}$ cm^{-3} (top to bottom) [18].

The absorption coefficient κ displays a complicated dependence on T and ρ (and also on the degree of ionization, chemical composition, etc.). Here, we adopted the simple approximation for $\kappa(T, \rho)$ [16–18]

$$\kappa(T,\rho) = \begin{cases} \kappa_1 \rho^{2/3} T^3, & \kappa_1 = 10^{-8} \quad (\kappa 1) \\ \kappa_2 \rho^{1/3} T^{10}, & \kappa_2 = 10^{-36} \quad (\kappa 2) \\ \kappa_3 \rho T^{-5/2}, & \kappa_3 = 1.5 \times 10^{20} \quad (\kappa 3) \\ \kappa_4, & \kappa_4 = 0.348. \quad (\kappa 4) \end{cases}$$

According to [18], these four subregions correspond to scattering on molecular hydrogen, scattering on atomic hydrogen, free–free and free–bound transitions, and Thompson scattering. The boundaries of the sub-regions, i.e., the transitions from one expression to another, are specified by the equality of the κ values calculated from these expressions. Figure 1 presents the dependences of κ on T and ρ. We can see regions with $d\kappa/dT > 0$, where thermal instability can develop when the dependence between the surface density and the disk temperature forms an S curve in the $(\Sigma, T_{\mathrm{eff}})$ plane. Thermal instability is often invoked to explain the phenomenon of dwarf novae (see, for example, [19, 20]); however, it is clear that this can occur only for sufficiently cool disks.

Let us return to (7), taking $\alpha = 0.1$ and $r = A/5$ and considering disks with dominant gas pressure, for which $\beta = {}^1\!/_3 aT^4/\rho\mathcal{R}T < 1$. The shaded region in the $(T, \dot{M})$ plane in Fig. 2a corresponds to all possible

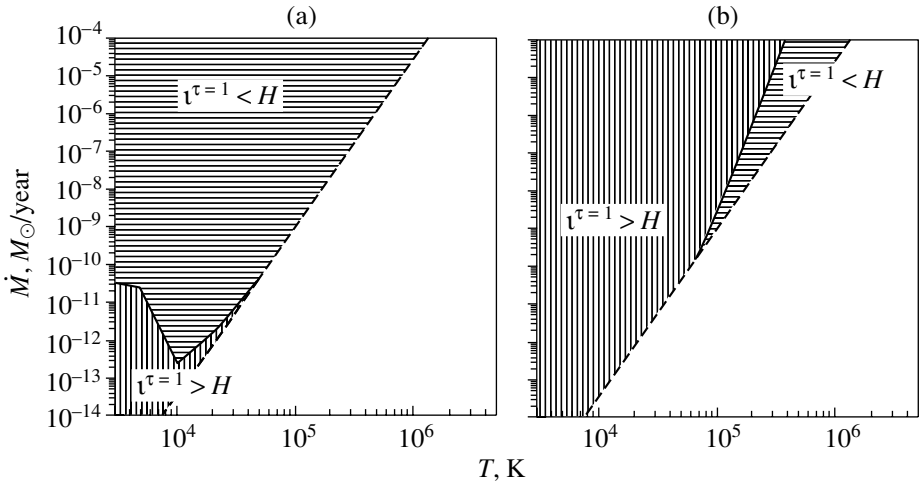

Fig. 2. (a) The domain of possible solutions of (7) for disks with dominant gas pressure in the $(T, \dot{M})$ plane for $\alpha = 0.1$ and $r = A/5$. The horizontal thick shading indicates optically thick disks, and vertical shading optically thin disks; the solid line marks the border between these regions. The dashed line corresponds to condition (9) for the existence of the solution of (7); there is no solution below this line. (b) Same as (a) for disks with dominant radiation pressure.

solutions for these disks. The dashed line corresponds to condition (9) for the existence of a solution for (7)—there is no solution below this line. The solid line indicates the boundary between the optically thick and optically thin solutions: the horizontal shading marks the region of optically thick disks, while the vertical shading marks optically thin disks. Figure 2b presents a similar pattern for disks with dominant radiation pressure ($\beta > 1$).

We can see from Fig. 2a that, for realistic values $\dot{M} \in [10^{-12}, 10^{-7}]\ M_\odot$/yr, disks with dominant gas pressure are mainly optically thick, though solutions corresponding to optically thin cool disks are possible for small $\dot{M}$. It follows from Fig. 2b that disks with dominant radiation pressure are mainly optically thin; optically thick hot disks can exist only for high $\dot{M}$.

2.4. Optically Thick Disks

In Section 2.2, we derived Eq. (7), which relates $\dot{M}$, T, and ρ for given a r and α. Using the supplementary heat-balance equation (1), we can reduce the number of unknowns and obtain the desired relation between $\dot{M}$ and T.

The vertical temperature distributions in optically thick disks are described by the equation of radiative heat conduction with a source due to viscous heating (1b), which can be written in the form

$$\frac{\partial e}{\partial t} = \frac{\partial}{\partial z}\left(\frac{1}{\kappa\rho}\frac{\partial}{\partial z}\left({}^1\!/_3 acT^4\right)\right) + \rho\alpha c_s^2\Omega_K, \quad (11)$$

where e is the specific internal energy and c is the velocity of light. To solve (11), we must specify boundary conditions. Due to the symmetry of the problem, the temperature derivative in the equatorial plane must be zero; i.e., $T'|_{z=0} = 0$. The temperature at the upper boundary of the disk is specified by the condition $\Gamma(T_*, T_{wd}) = \Lambda(T_*)$. Though the functions $\Gamma(T, T_{wd})$ and $\Lambda(T)$ are complex, they are known and can be found in the literature (see, for example, [21–23]). The temperature derived by equating these functions (for a temperature of the central object (white dwarf) of $T_{wd} = 70\,000$ K) is $T(H) = T_* = 13\,600$ K.

The solution of (11) enters a stationary regime when the characteristic heat-conduction time

$$t_{diff} \simeq \frac{\mathcal{R}\kappa\rho^2 H^2}{acT^3}$$

is comparable to the time for viscous heating

$$t_{heat} \simeq \frac{\mathcal{R}T}{\alpha c_s^2\Omega_K} \simeq \alpha^{-1}\Omega_K^{-1}.$$

Note that (11) can be integrated analytically in the steady-state case. Let us denote $U = T^4$, $U_* = T_*^4$, $U_0 = U|_{z=0}$ and again assume that ρ does not depend on z. Then,

$$\frac{d}{dz}\left(\frac{1}{\kappa\rho}\frac{d}{dz}\left(\frac{ac}{3}U\right)\right) = -\rho\alpha c_s^2\Omega_K.$$

After integrating over z, we obtain

$$\frac{1}{\kappa\rho}\frac{d}{dz}\left(\frac{ac}{3}U\right) = -\rho\alpha c_s^2\Omega_K z.$$

The integration constant is equal to zero, since $U'|_{z=0} = 0$. For convenience, we will transform this last equation to the form

$$\frac{1}{\kappa}\frac{dU}{dz} \equiv \frac{dB}{dz} = -\frac{3}{ac}\rho^2\alpha c_s^2\Omega_K z,$$

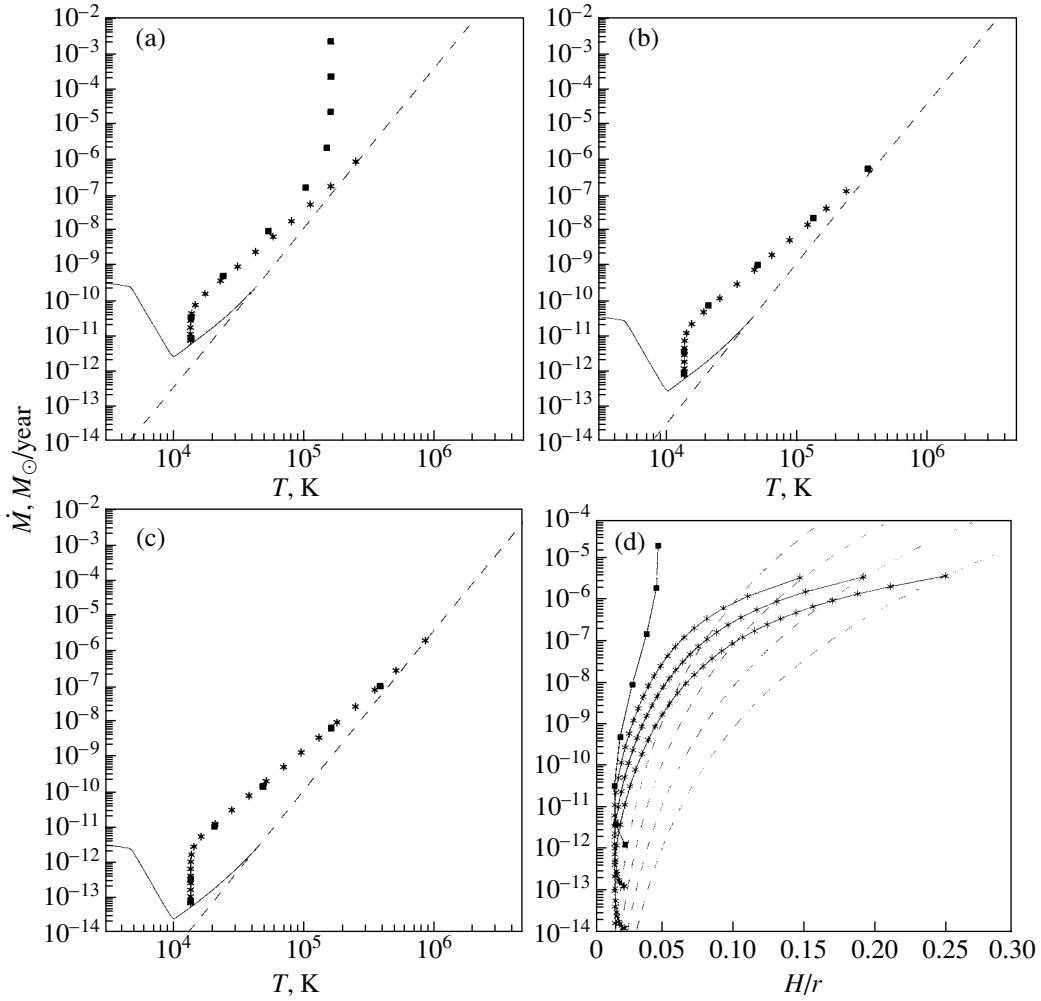

Fig. 3. (a) Solution of (11) for an optically thick disk for $\alpha = 1$ and $r = A/5$ (asterisks). Solutions of (12) taking into account convection are labeled by squares. The dashed line is a lower bound for the region in which there exist solutions of (7), and the solid line separates the regions of optically thin and optically thick disks. (b) Same as (a) for $\alpha = 0.1$. (c) Same as (a) for $\alpha = 0.01$. (d) A disk with dominant gas pressure. The solid lines indicate possible states of the disk in the $H/r - \dot{M}$ plane for $r = A/5$. Solutions of (11) taking into account radiative heat conduction and viscous heating are shown by the lines with asterisks for $\alpha = 0.1$, $\alpha = 10^{-2}$, and $\alpha = 10^{-3}$ (top to bottom). Solutions of (12) taking into account radiative heat conduction, convection, and viscous heating are shown by the lines with squares for $\alpha = 1$. The dashed lines bound from below regions in which the solution of (7) can exist for $\alpha = 1$, $\alpha = 0.1$, $\alpha = 10^{-2}$, and $\alpha = 10^{-3}$ (top to bottom).

where the function $B(U)$ is determined from the differential equation $\dfrac{dB}{dU} = \dfrac{1}{\kappa(U,\rho)}$ and can be written in an analytical form if ρ is fixed. Integrating this last equation over z, we obtain

$$B(U) = B(U_*) + \frac{3}{2ac}\rho^2\alpha c_s^2\Omega_K(H^2 - z^2)$$

or, for $z = 0$,

$$B(U_0) = B(U_*) + \frac{3}{2ac}\rho^2\alpha c_s^2\Omega_K H^2.$$

Using the expressions

$$c_s^2 = \left(\mathcal{R}U_0^{1/4} + {}^1\!/_3\frac{aU_0}{\rho}\right),$$

$$H^2 = \left(\mathcal{R}U_0^{1/4} + {}^1\!/_3\frac{aU_0}{\rho}\right)\Omega_K^{-2},$$

we obtain the algebraic equation for U_0

$$B(U_0) = B(U_*) + \frac{3}{2ac}\rho^2\alpha\Omega_K^{-1} \times \left(\mathcal{R}U_0^{1/4} + {}^1\!/_3\frac{aU_0}{\rho}\right)^2.$$

This equation implicitly specifies the dependence $U_0(\rho)$, i.e., $T(\rho)$. Expressing $\dot{M}$ in terms of ρ and T, we can derive the dependence $\dot{M}(\rho) = \dot{M}(T(\rho),\rho)$, which yields the dependence $T(\dot{M})$ in parametric form. Formally, the resulting solution can also exist

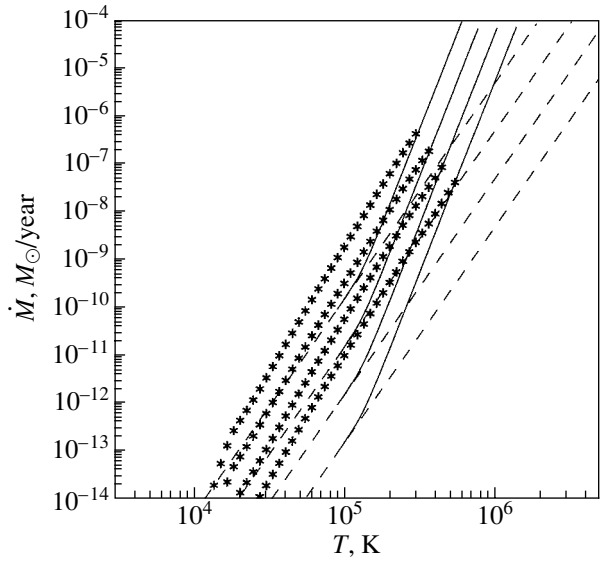

Fig. 4. Solutions for an optically thin disk for $\alpha = 1$, $\alpha = 0.1$, $\alpha = 10^{-2}$, $\alpha = 10^{-3}$ (top to bottom) and $r = A/20$ (asterisks). The dashed lines bound from below the domain in which there exists a solution of (7); the solid lines separate the regions for optically thin and optically thick disks.

in optically thin regions; however, given the adopted assumptions, these points can be rejected.

Let us consider a graphical representation of the solution derived. Figure 3a presents the dependence $T(\dot{M})$ for $\alpha = 1$ and $r = A/5$, marked by asterisks. As in Fig. 2, the dashed lines bound from below the domain in which there exist solutions of (7), while the solid line separates the domains of optically thin and optically thick disks. Figures 3b, 3c display the solutions for $\alpha = 0.1$ and $\alpha = 0.01$, respectively. Figure 3c presents the accretion rate as a function of the disk thickness. We can see that all the obtained disks are geometrically thin; i.e., $H \ll r$.

Radiative heat conduction is not the only mechanism for heat transfer into optically thin regions. Under certain conditions, convection can also play a substantial role. Neglecting the radiation pressure, the convective flux can be written in the form [24, 25]

$$F_{conv} = c_P \rho \left(\frac{|g|}{T}\right)^{1/2} \frac{l^2}{4} (\triangle\nabla T)^{3/2},$$

$$\triangle\nabla T = -\frac{T}{c_P}\frac{\partial S}{\partial z}.$$

Here, c_P is the heat capacity at constant pressure, $S = \mathcal{R}\ln(T^{3/2}/\rho)$ is the specific entropy, $g = -\Omega_K^2 z$ is the gravitational acceleration, and l is the mixing length, taken to be $l = \alpha H$. To determine the vertical temperature distribution taking convection into account, we must solve the equation

$$\frac{\partial e}{\partial t} = \frac{\partial}{\partial z}\left(\frac{1}{\kappa\rho}\frac{\partial}{\partial z}\left({}^1\!/_3 acT^4\right)\right) - \frac{\partial F_{conv}}{\partial z} + \rho\alpha c_s^2 \Omega_K \tag{12}$$

with the same boundary conditions as for (11). Equation (12) does not admit a simple analytical solution, and we solved this equation numerically using the method of establishment. The solution is denoted by the squares in Figs. 3a–3c. We can see that convection plays a significant role only when $\alpha \simeq 1$.

Summarizing, we can assert that, in the optically thick case with small $\dot{M}$, the disk displays the constant temperature $T = T_* = 13\,600$ K, while the temperature increases as $T \propto \dot{M}^{1/3}$ at larger values of $\dot{M}$. Thus, for realistic parameters of the accretion disks in close binaries, $\dot{M} \simeq 10^{-12}$–$10^{-7}\ M_\odot$/yr and $\alpha \simeq 10^{-1}$–10^{-2}, the gas temperature in the outer parts of the disk ($r \simeq A/5$–$A/10$) is from $\sim 10^4$ to $\sim 10^6$ K.

Solving (11) for various r, we can also calculate the dependences $T(r)$ and $\rho(r)$. The calculations indicate that $T \propto r^{-0.8}$ and $\rho \propto r^{-1.8}$, which is consistent with the dependence $T \propto r^{-3/4}$ obtained by Shakura and Sunyaev [26].

2.5. Optically Thin Disks

In this case, the temperature of the disk is specified by the balance between radiative heating $\Gamma(T, T_{wd})$ and viscous heating (5), on the one hand, and radiative cooling $\Lambda(T)$, on the other. The heat-balance equation (1a) can be written

$$\rho\alpha c_s^2 \Omega_K + \rho^2 m_p^2 (\Gamma(T, T_{wd}) - \Lambda(T)) = 0,$$

which can be reduced to the quadratic equation in ρ

$$\alpha(\rho\mathcal{R}T + {}^1\!/_3 aT^4)\Omega_K + \rho^2 m_p^{-2}(\Gamma(T, T_{wd}) - \Lambda(T)) = 0.$$

The solution of this equation for specified r and α yields the dependence $\rho(T)$, and thus $T(\dot{M})$. Formally, this solution can also exist in optically thick regions; however, these points were rejected by virtue of the adopted assumptions.

It is shown in Section 2.3 that disks in which gas pressure dominates are primarily optically thick, and solutions that correspond to optically thin disks are possible only for small $\dot{M}$. Disks in which radiation pressure dominates are primarily optically thin. The domination of radiation pressure is possible only in the inner parts of the disk; therefore, we will adopt $r = A/20$ for the further analysis. For the typical

dwarf nova IP Peg, this corresponds to five radii of the accretor (white dwarf).

Figure 4 presents the results of our calculations; the asterisks denote the $T(\dot{M})$ dependences for $\alpha = 1$, $\alpha = 0.1$, $\alpha = 10^{-2}$, $\alpha = 10^{-3}$ (top to bottom), and $r = A/20$. The disks obtained in these solutions are geometrically thick, $H \simeq r$. Note that the initial assumptions of the model restrict its applicability: it is suitable only for geometrically thin disks, and the solutions for geometrically thick disks are purely formal.

3. THE MODEL

We described the flow structure in a binary system using a system of gravitational gas-dynamical equations taking into account radiative heating and cooling of the gas for the optically thin case:

$$\begin{cases} \frac{\partial \rho}{\partial t} + \operatorname{div} \rho\mathbf{v} = 0 \\ \frac{\partial \rho\mathbf{v}}{\partial t} + \operatorname{div}(\rho\mathbf{v} \otimes \mathbf{v}) + \operatorname{grad} P = -\rho \operatorname{grad} \Phi \\ \frac{\partial \rho(\varepsilon + |\mathbf{v}|^2/2)}{\partial t} + \operatorname{div} \rho\mathbf{v}(\varepsilon + P/\rho + |\mathbf{v}|^2/2) = -\rho\mathbf{v} \operatorname{grad} \Phi + \rho^2 m_p^{-2} \left(\Gamma(T, T_{wd}) - \Lambda(T)\right). \end{cases} \quad (13)$$

Here, as usual, ρ is the density, $\mathbf{v} = (u, v, w)$ is the velocity vector, P is the pressure, ε is the internal energy, Φ is the Roche gravitational potential, m_p is the proton mass, and $\Gamma(T, T_{wd})$ and $\Lambda(T)$ are the radiative heating and cooling functions, respectively. The system of gas-dynamical equations was closed with the Clapeyron equation $P = (\gamma - 1)\rho\varepsilon$, where γ is the adiabatic index. We took the parameter γ to be $^5/_3$.

Our main goal here is to study the morphology of the interaction between the stream and the cool accretion disk. It follows from Section 2 that the outer parts of the accretion disk can be cool for small $\dot{M}$ and, in particular, in the case of an optically thin disk. The system of equations (13) enables us to carry out three-dimensional modeling of the flow structure in a binary within our formulation of the problem. In the model, the temperature of the disk is 13 600 K.

We solved this system of equations using the Roe–Osher method [14, 27, 28], adapted for multiprocessing computations via spatial decomposition of the computation grid (i.e., partitioning into subregions, with synchronization of the boundary conditions) [29]. We considered a semidetached binary system containing a donor with mass M_2 filling its Roche lobe and an accretor with mass M_1. The system parameters were specified to be those of the dwarf nova IP Peg: $M_1 = 1.02\,M_\odot$, $M_2 = 0.5\,M_\odot$, $A = 1.42\,R_\odot$.

The modeling was carried out in a non-inertial reference frame rotating with the binary, in Cartesian coordinates in a rectangular three-dimensional grid. Since the problem is symmetrical about the equatorial plane, only half the space occupied by the disk was modeled. To join the solutions, we specified a corresponding boundary condition at the lower boundary of the computation domain. The accretor had the form of a sphere with radius $10^{-2}A$. All matter that ended up within any of the cells forming the accretor was taken to fall onto the star. A free boundary condition was specified at the outer boundaries of the disk—the density was constant ($\rho_b = 10^{-8}\rho_{L_1}$), where ρ_{L_1} is the density at the point L_1, the temperature was 13 600 K, and the velocity was equal to zero. The stream was specified in the form of a boundary condition: matter with temperature 5800 K, density $\rho_{L_1} = 1.6 \times 10^{-8}\mathrm{g/cm^3}$ and velocity along the x axis $v_x = 6.3$ km/s was injected into a zone around L_1 with radius $0.014A$. For this rate of matter input into the system, the model accretion rate was $\approx 10^{-12} M_\odot/\mathrm{yr}$.

The size of the computation domain, $1.12A \times 1.14A \times 0.17A$, was selected so that it entirely contains both the disk and stream, including the point L_1. The computation grid with $121 \times 121 \times 62$ cells was distributed between 81 processors, which constituted a two-dimensional 9×9 matrix.

To increase the accuracy of the solution, the grid was made denser in the zone of interaction between the stream and disk, making it possible to resolve well the formed shock wave. The grid was also denser toward the equatorial plane, so that the vertical structure was resolved, even for such a cool disk.

We used the solution obtained for a model without cooling as the initial conditions [12]. The model with cooling was computed during approximately five revolutions of the system, until the solution became established. The total time of the computations was

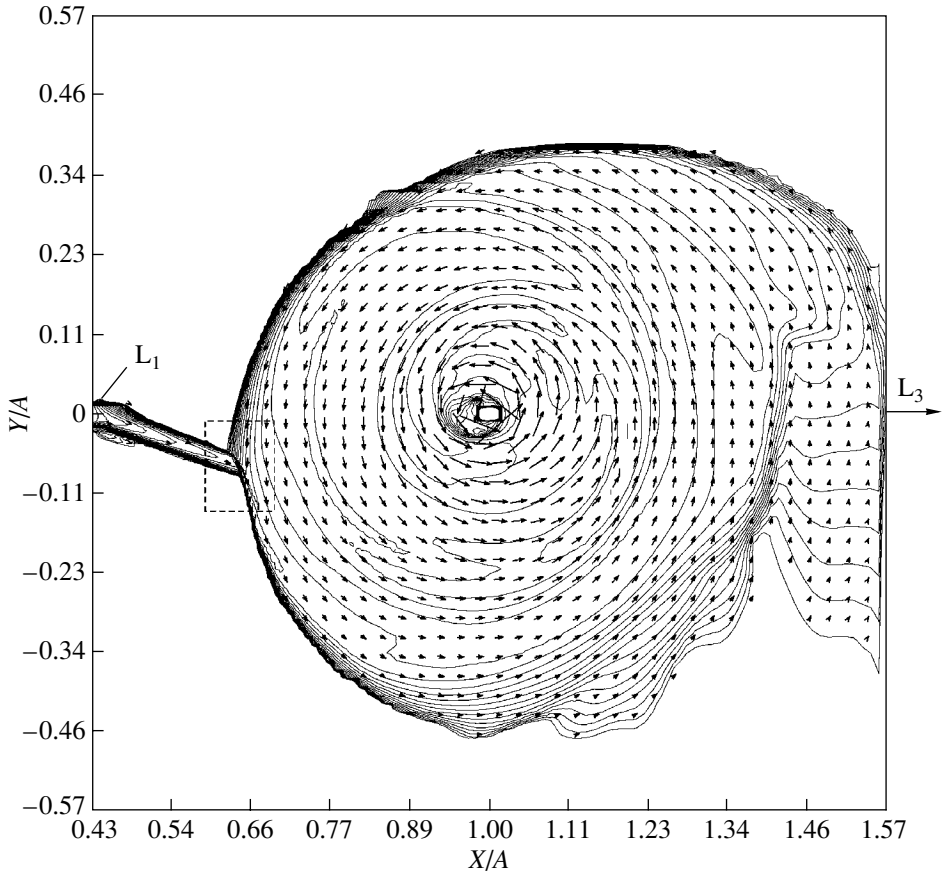

Fig. 5. Contours of constant density and velocity vectors in the equatorial plane XY of the system. The shaded rectangle indicates the zone of interaction between the stream and disk, shown in Figs. 7 and 8. The point L_1 and the direction toward L_3 are marked.

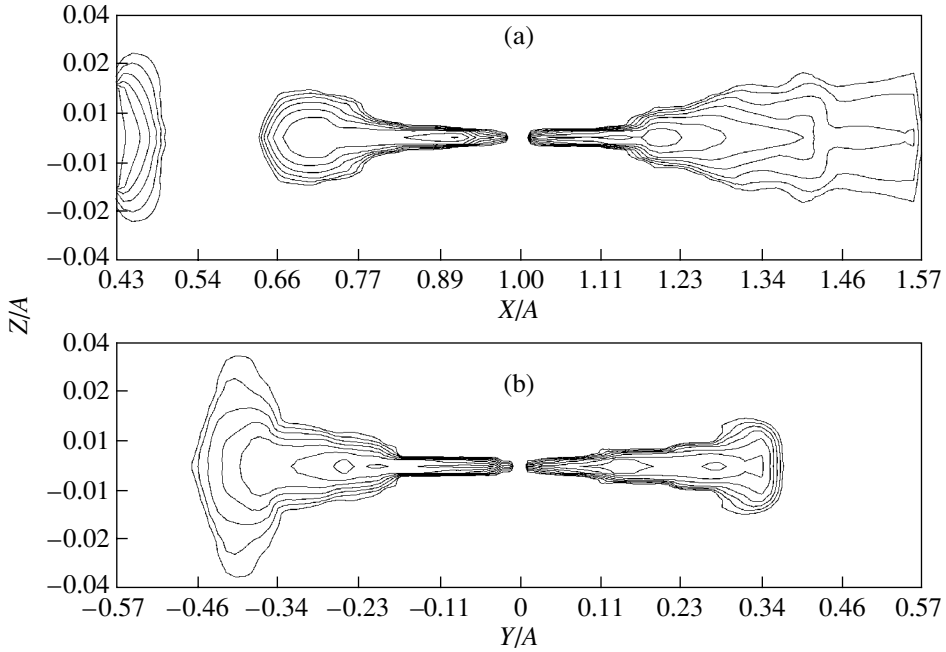

Fig. 6. (a) Density contours in the frontal plane XZ of the system. (b) Density contours in the plane YZ containing the accretor and perpendicular to the line connecting the binary components.

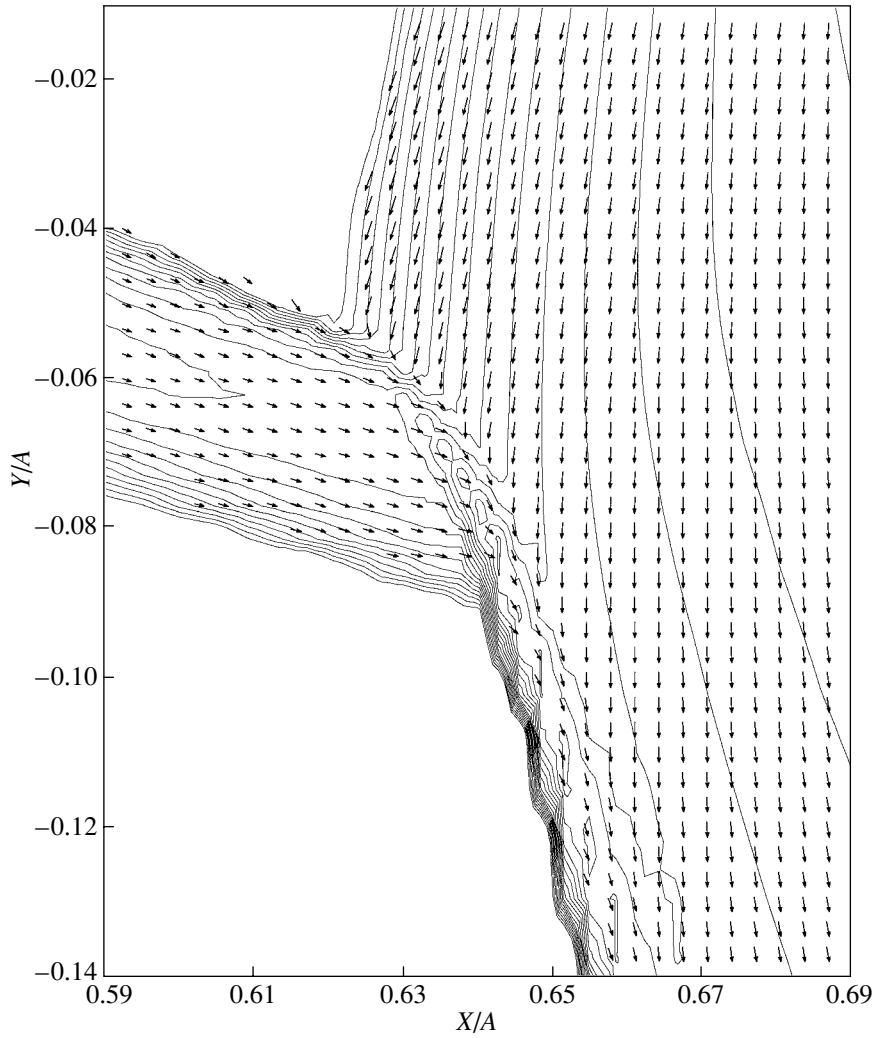

Fig. 7. Contours of constant density and velocity vectors in the zone of interaction between the stream and disk (the shaded rectangle in Fig. 5).

≈1000 h on the MBC1000A computer of the Interdepartmental Supercomputer Center (ISC).

4. COMPUTATION RESULTS

Figures 5 to 8 present the morphology of gas flows in the binary. Figure 5 shows the density and velocity-vector distributions in the equatorial plane of the system (the XY plane), while Figs. 6a and 6b present density contours in the frontal (XZ) plane and in the YZ plane containing the accretor and perpendicular to the line connecting the binary components. In spite of the small height of the forming accretion disk, use of the ISC parallel-processing computers made it possible to resolve its vertical structure (the outer parts of the disk were covered by 15 grid cells, and the inner parts by no fewer than 3 cells). Figure 7 gives an enlarged view of the density and velocity-vector distributions in the zone of interaction between the stream and the outer edge of the disk (the area in the shaded rectangle in Fig. 5). Figure 8 presents the so-called texture—a visualization of the velocity field in the zone of interaction between the stream and disk, constructed using the Line Integral Convolution procedure (LIC) [30].

According to our considerations in [8, 14], the gas-dynamical flow pattern in a semidetached binary is formed by the stream from L_1, the disk, a "circumdisk halo," and the intercomponent envelope. This subdivision is based on physical differences between these elements of the flow structure: (1) if the motion of the gas is not determined by the gravitational field of the accretor, it forms the intercomponent envelope; (2) if the gas makes one revolution around the accretor but later mixes with the initial stream, this gas does not become part of the disk, instead forming the circumdisk halo; (3) the disk is formed by that part of the

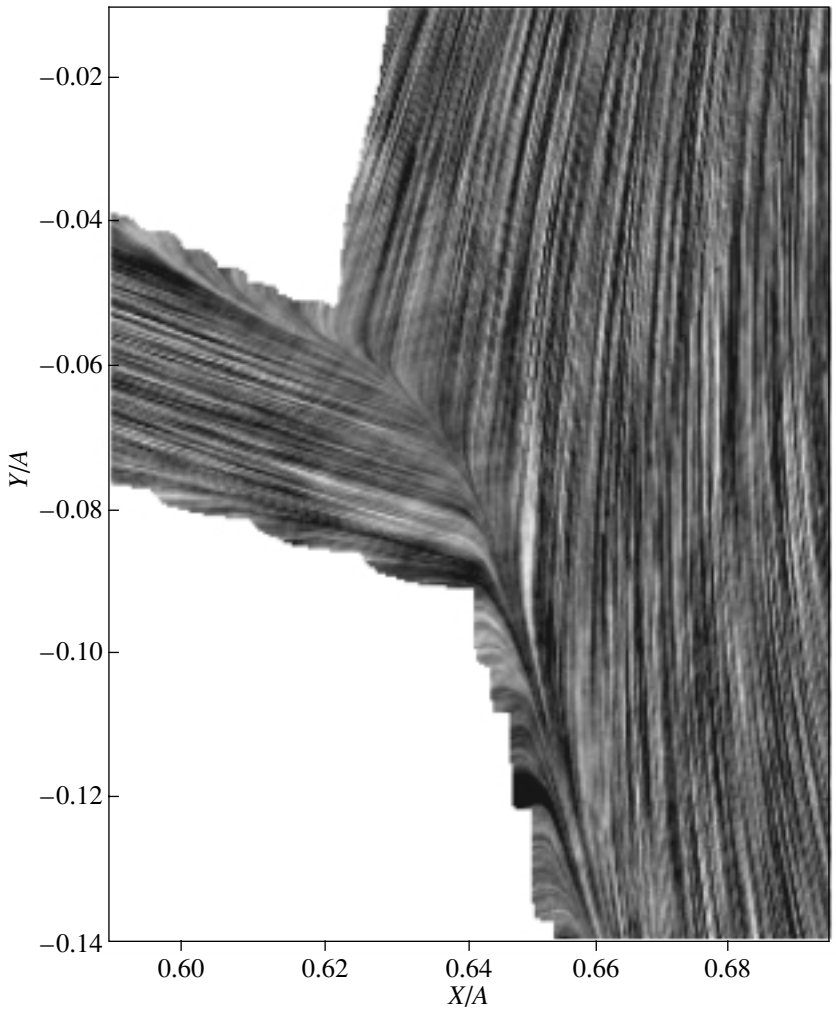

Fig. 8. Visualization of the velocity field in the zone of interaction between the stream and disk (the shaded rectangle in Fig. 5).

stream that loses its momentum and moves toward the center of gravity after entering the gravitation field of the accretor, rather than interacting with the stream.

In this framework, let us consider the morphology of the flow when the temperature decreases to 13 600 K over the entire computation domain due to cooling. Figure 5 indicates that, in this case, the intercomponent envelope is formed primarily in the vicinity of L_3 and does not affect the solution substantially. We can see from Figs. 5 and 6 that the circumdisk halo is pressed against the disk, and its density increases sharply toward the disk edge.

Figures 7 and 8 show that, in the cool-disk case, the interaction between the circumdisk halo and the stream displays all features typical of an oblique collision of two streams. We can clearly see two shock waves and a tangential discontinuity between them. The gases forming the halo and stream pass through the shocks corresponding to their flows, mix, and move along the tangential discontinuity between the two shocks. Further, this material forms the disk itself, the halo, and the envelope.

The solution for the cool case displays the same qualitative characteristics as the solution for the case when the outer parts of the disk are hot: the interaction between the stream and disk is shockless, a region of enhanced energy release is formed due to the interaction between the circumdisk halo and the stream and is located beyond the disk, and the resulting shock is fairly extended, which is particularly important for explaining the observations. However, unlike the solution with a high temperature in the outer regions of the disk [1, 12, 14], in the cool case, the shape of the zone of shock interaction between the stream and halo is more complex than a simple "hot line." This is due to the sharp increase of the halo density as the disk is approached. Those parts of the halo that are far from the disk have low density, and the shock due to their interaction with the stream

is situated along the edge of the stream. As the halo density increases, the shock bends, and eventually stretches along the edge of the disk.

5. CONCLUSIONS

Our analysis of the basic processes of heating and cooling in accretion disks in binaries has shown that, for realistic parameters of the accretion disks in close binary systems ($\dot{M} \simeq 10^{-12}$–$10^{-7}\ M_\odot$/yr and $\alpha \simeq 10^{-1}$–10^{-2}), the gas temperature in the outer parts of the disk is from 10^4 to $\sim 10^6$ K.

Previously, we carried out three-dimensional simulations of the flow structure in close binaries for the case when the temperature of the outer parts of the accretion disk was 200–500 thousand K. Those solutions showed that the interaction between the stream from the inner Lagrange point and the disk was shockless. To determine the generality of the solution, the morphology of the flow for different disk temperatures must be considered. We have presented here the results of simulations for the case when cooling decreases the temperature to 13 600 K over the entire computation domain.

Our analysis of the flow pattern for the cool outer parts of the disk confirms that the interaction between the stream and disk is again shockless. The computations indicate that the solution for the cool-disk case displays the same qualitative features as in the case when the outer parts of the disk are hot: the interaction between the stream and disk is shockless, a region of enhanced energy release formed by the interaction between the circumdisk halo and the stream is located beyond the disk, and the shock wave that is formed is fairly extended and can be considered a "hot line." The cool solution demonstrates the universal character of our previous conclusions that the interaction between the stream and disk in semidetached binaries is shockless.

6. ACKNOWLEDGMENTS

This work was supported by the Russian Foundation for Basic Research (project codes 02-02-16088, 02-02-17642, 03-02-16622, 03-01-00311), the State Science and Technology Program in Astronomy, a Presidential Grant of the Russian Federation (for support of leading scientific schools), the Programs of the Presidium of the Russian Academy of Sciences "Mathematical Modeling" and "Nonsteady State Processes in Astronomy," and the INTAS Foundation (grant 01-491).

REFERENCES

1. D. V. Bisikalo, A. A. Boyarchuk, O. A. Kuznetsov, and V. M. Chechetkin, Astron. Zh. **74**, 880 (1997) [Astron. Rep. **41**, 786 (1997)].
2. D. V. Bisikalo, A. A. Boyarchuk, O. A. Kuznetsov, and V. M. Chechetkin, Astron. Zh. **74**, 889 (1997) [Astron. Rep. **41**, 794 (1997)].
3. D. V. Bisikalo, A. A. Boyarchuk, O. A. Kuznetsov, and V. M. Chechetkin, Astron. Zh. **75**, 706 (1998) [Astron. Rep. **42**, 621 (1998)].
4. D. V. Bisikalo, A. A. Boyarchuk, V. M. Chechetkin, *et al.*, Mon. Not. R. Astron. Soc. **300**, 39 (1998).
5. D. V. Bisikalo, A. A. Boyarchuk, O. A. Kuznetsov, and V. M. Chechetkin, Astron. Zh. **76**, 270 (1999) [Astron. Rep. **43**, 229 (1999)].
6. D. V. Bisikalo, A. A. Boyarchuk, O. A. Kuznetsov, and V. M. Chechetkin, Astron. Zh. **76**, 672 (1999) [Astron. Rep. **43**, 587 (1999)].
7. D. V. Bisikalo, A. A. Boyarchuk, O. A. Kuznetsov, and V. M. Chechetkin, Astron. Zh. **76**, 905 (1999) [Astron. Rep. **43**, 797 (1999)].
8. D. V. Bisikalo, A. A. Boyarchuk, O. A. Kuznetsov, and V. M. Chechetkin, Astron. Zh. **77**, 31 (2000) [Astron. Rep. **44**, 26 (2000)].
9. D. Bisikalo, P. Harmanec, A. Boyarchuk, *et al.*, Astron. Astrophys. **353**, 1009 (2000).
10. D. V. Bisikalo, A. A. Boyarchuk, A. A. Kil'pio, *et al.*, Astron. Zh. **78**, 707 (2001) [Astron. Rep. **45**, 611 (2001)].
11. D. V. Bisikalo, A. A. Boyarchuk, A. A. Kil'pio, and O. A. Kuznetsov, Astron. Zh. **78**, 780 (2001) [Astron. Rep. **45**, 676 (2001)].
12. O. A. Kuznetsov, D. V. Bisikalo, A. A. Boyarchuk, *et al.*, Astron. Zh. **78**, 997 (2001) [Astron. Rep. **45**, 872 (2001)].
13. D. Molteni, D. V. Bisikalo, O. A. Kuznetsov, and A. A. Boyarchuk, Mon. Not. R. Astron. Soc. **327**, 1103 (2001).
14. A. A. Boyarchuk, D. V. Bisikalo, O. A. Kuznetsov, and V. M. Chechetkin, *Mass Transfer in Close Binary Stars* (Taylor and Francis, London, 2002).
15. N. I. Shakura, Astron. Zh. **49**, 921 (1972) [Sov. Astron. **16**, 756 (1972)].
16. D. N. Lin and J. Papaloizou, Mon. Not. R. Astron. Soc. **191**, 37 (1980).
17. D. R. Alexander, G. C. Augason, and H. R. Johnson, Astrophys. J. **345**, 1014 (1989).
18. K. R. Bell and D. N. C. Lin, Astrophys. J. **427**, 987 (1994).
19. J. K. Cannizzo and S. J. Kenyon, Astrophys. J. Lett. **309**, L43 (1986).
20. E. Meyer-Hofmeister and H. Ritter, in *The Realm of Interacting Binary Stars*, Ed. by J. Sahade, G. E. McCluskey, Jr., and Y. Condo (Kluwer Acad., Dordrecht, 1993), p. 143.
21. D. P. Cox and E. Daltabuit, Astrophys. J. **167**, 113 (1971).
22. J. C. Raymond, D. P. Cox, and B. W. Smith, Astrophys. J. **204**, 290 (1976).

23. L. Spitzer, Jr., *Physical Processes in the Interstellar Medium* (Wiley, New York, 1978; Mir, Moscow, 1981).
24. M. Schwarzschild, *Structure and Evolution of the Stars* (Princeton Univ. Press, Princeton, 1958; Inostr. Lit., Moscow, 1961).
25. G. S. Bisnovatyĭ-Kogan, *Physical Processes in the Theory of Stellar Evolution* (Nauka, Moscow, 1989; Springer, Berlin, 2001) [in Russian].
26. N. I. Shakura and R. A. Sunyaev, Astron. Astrophys. **24**, 337 (1973).
27. P. L. Roe, Ann. Rev. Fluid Mech. **18**, 337 (1986).
28. S. R. Chakravarthy and S. Osher, AIAA Pap. No. 85-0363 (1985).
29. P. V. Kaĭgorodov and O. A. Kuznetsov, Preprint No. 59 (Keldysh Inst. App. Math., Rus. Acad. Sci., Moscow, 2002).
30. B. Cabral and C. Leedom, in *ACM SIGGRAPH, Computer Graphics Proceedings '93* (1993), p. 263.

Translated by K. Maslennikov

Astronomy Reports, Vol. 47, No. 10, 2003, pp. 821–825. Translated from Astronomicheskiĭ Zhurnal, Vol. 80, No. 10, 2003, pp. 891–895.

The Inverse Compton Effect in a Pulsar–Be-star Binary

A. I. Bogomazov and V. M. Lipunov

Moscow State University, Moscow, Russia

Received October 10, 2002; in final form, May 8, 2003

Abstract—The Compton interaction between the optical radiation of a Be star and the relativistic wind of a radio pulsar in a binary system is investigated. The first calculations of the periodic variations of the X-ray radiation due to the anisotropic radiation field of the optical star are presented. Under favorable conditions, the Compton X-ray radiation can vary by a factor of a few. © *2003 MAIK "Nauka/Interperiodica"*.

1. INTRODUCTION

Modern scenarios for the evolution of massive close binary systems predict the existence of a subclass of binaries in which one of the components is a radio pulsar and the other is a massive optical star. Quantitative estimates indicate that roughly one of every 700 observed radio pulsars should have an OB-star companion [1, 2]. The radio pulsars PSR B1259–63 and PSR J0045–7319 discovered about ten years ago provide examples of such binary systems.

Numerical computations of evolutionary tracks of these systems have been obtained using the "Scenario Machine," both leading up to their formation and predicting their possible futures [3, 4]. The high orbital eccentricities in these systems are explained by anisotropy of the collapse during the supernova explosion. In addition, the possibility of additional angular momentum being acquired during the supernova explosion follows from precessional effects detected in the PSR J0045–7319 system [5]. At the beginning of its evolution, this system consisted of two main-sequence stars, with the rotational axis of the B-star component being perpendicular to the orbital plane. To change this configuration (i.e., to rotate the orbital plane relative to the rotational axis of the B star), the pulsar must have acquired additional angular momentum.

The best-studied such binary system contains the radio pulsar PSR B1259–63 and an optical companion that has been identified with the 10^m Be star SS 2883 [6]. PSR B1259–63 (which has a rotational period of 47.76 ms) was discovered on the 64-m Parkes telescope [6] during a high-frequency survey of the southern Galactic plane [7]. The pulsar moves along a very elongated orbit ($e \geq 0.87$) around the massive optical companion.

The PSR B1259–63 system has been observed numerous times in the X-ray. It has been demonstrated that the X-ray radiation of this system arises as a result of the inverse Compton effect [8]. The pulsar is a source of relativistic protons and electrons, while the massive optical star is a source of soft photons. The inverse Compton scattering of soft photons of the optical star on the relativistic particles produced by the pulsar wind gives rise to broadband X-ray radiation.

In the present paper, we consider the X-ray radiation of the subclass of such systems in which the radio pulsar has a Be-star companion. It was shown earlier that such systems should display orbital modulation of their X-ray luminosity [9].

A Be star is a rapidly rotating object, for which the dependence of the surface temperature on the free-fall acceleration becomes important, in accordance with the von Zeipel theorem:

$$T = T_p(g_{\text{eff}})^{0.25}, \qquad (1)$$

where T is the surface temperature of the Be star (which depends on the latitude), T_p is the temperature at the pole (taken to be 25 000 K in the computations), and $g_{\text{eff}} = g_p/g(\vartheta)$ is the effective free-fall acceleration (g_p is the free-fall acceleration at the pole, and $g(\vartheta)$ is its value at latitude ϑ).

Consequently, even if we consider a fixed distance from the star, the density of the soft radiation will not be the same in all directions, so that the hard radiation should depend on the position of the Comptonization point (CP)—the place where the inverse Compton effect occurs.

We have derived the theoretical dependence of the X-ray luminosity of a pulsar–Be-star system on the mutual positions of the two components, based on numerical computations.

2. SOFT RADIATION OF THE Be STAR

The Be star in the computed model is an ellipsoid of rotation, which is specified by the focal parameter

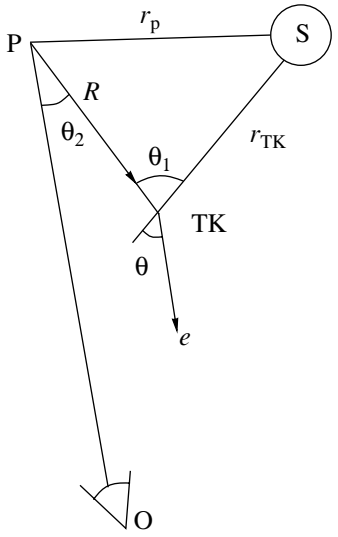

Fig. 1. Schematic of the binary system considered. See the text for an explanation of the notation.

P (for a nonrotating star, this is the radius, taken to be 7×10^{11} cm) and the eccentricity e (which depends on the rotational velocity of the star).

The intensity of the Be-star radiation in the direction of the Comptonization point is equal to the integral over the visible surface of the star:

$$I_v = \int B_v(1 - x + x\cos n)\cos n d\vartheta_{\rm Be} d\varphi. \qquad (2)$$

Here, n is the angle between the direction toward the Comptonization point and the normal to the stellar surface, B_v is the Planck function, with the temperature determined by (1), and x is the disk limb-darkening coefficient.

The free-fall acceleration at the surface of the Be star depends on the latitude as

$$g = g_p - \omega^2 r|\cos\vartheta_{\rm Be}|. \qquad (3)$$

The inequality of I_v in different directions from the star follows from the fact that the free-fall acceleration varies with the latitude at the surface, as well as the differences in the projected areas of the ellipsoid for Comptonization points located at different angles relative to the equatorial plane of the Be star.

To simplify the model, we adopted a unit normal vector directed along the radius vector and assumed that the disk limb-darkening coefficient was constant and equal to 0.35.

The density of soft radiation is equal to

$$n_v = \frac{1}{c}\int I_v d\Omega. \qquad (4)$$

Here, c is the speed of light and Ω is the solid angle subtended by the Be star.

3. THE PULSAR WIND

The pulsar is taken to be an isotropic source of relativistic electrons with a power-law spectrum [10]:

$$\frac{dN_\gamma}{d\gamma} = \frac{s-2}{\gamma_{\rm min}^{2-s} - \gamma_{\rm max}^{2-s}}\gamma^{-s}\frac{L_w}{m_e c^2}, \qquad (5)$$

where m_e is the rest mass of the electron. For definiteness, we adopt the value $s = 2.4$ and assume that the "electron" luminosity of the pulsar L_w is equal to the solar value. We take the maximum and minimum Lorentz factors γ to be 100 and 10.

The density of electrons at a distance R from the pulsar is

$$n_\gamma = \frac{dN_\gamma}{4\pi R^2 c}, \qquad (6)$$

where dN_γ is the number of electrons with Lorentz factor γ emitted by the pulsar each second.

4. THE X-RAY LUMINOSITY

Figure 1 presents a schematic of the system considered. S denotes the Be star, P the pulsar, O the observer, CP the point where the inverse Compton effect occurs, $r_{\rm P}$ the distance from the pulsar to the Be star, $r_{\rm CP}$ the distance from the star to the Comptonization point, R the distance from the pulsar to the Comptonization point, θ the angle between the directions of propagation of the photon before and after it is scattered, θ_1 the angle between the directions of motion of the relativistic particle and soft photon before scattering, and θ_2 the angle between the direction toward the observer and the direction of motion of the relativistic particle. In the general case, these points are not always located in a single plane.

In the model considered, we assume, first, that the γ factor of the electron remains constant (this will be the case if the pulsar is far from the Be star, at distances of 10^{14} cm or more, but variations in the electron Lorentz factor must be taken into account in very close binary systems) and also that $h\nu\gamma \ll m_e c^2$ (where $h\nu$ is the photon energy before scattering). Second, we assume that a relativistic particle scatters photons predominantly in the direction of its motion, so that $\theta_2 \ll 1$ and $\theta_1 \approx \theta$; therefore, $\cos\theta_2 = 1$ and $\int d(\cos\theta_2) = 1$.

The luminosity of the scattered photons per unit solid angle is

$$L = \int E n_v n_\gamma c(1 - \beta\cos\theta_1)\sigma_k dV dv d\gamma. \qquad (7)$$

Here, $\beta = v/c$, $dV = 2\pi R^2 dR d(\cos\theta_2)$, n_γ is determined by (5), n_v is determined by (4), E is the energy of the scattered photon, and σ_k is the Klein–Nishina

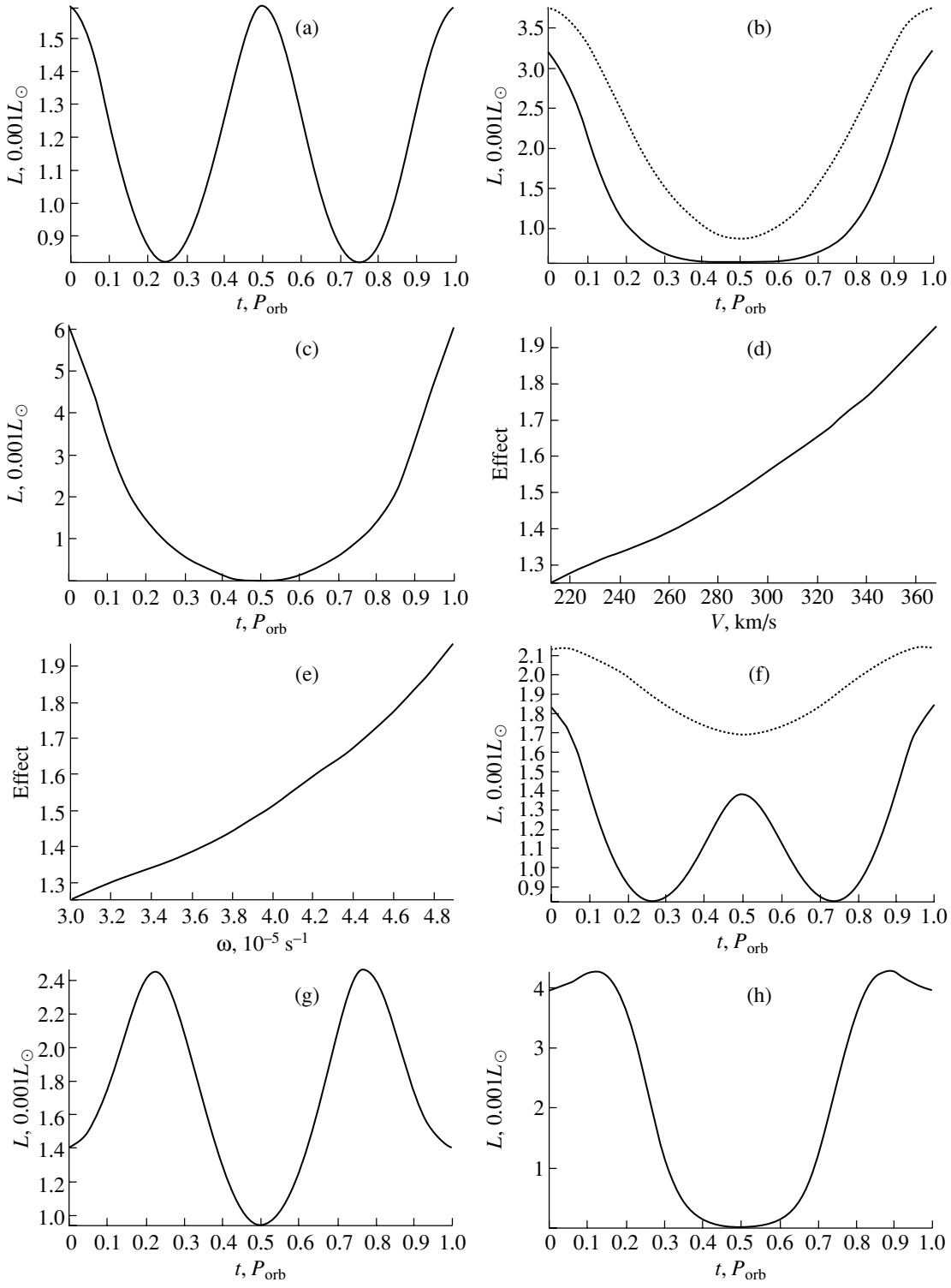

Fig. 2. The results of computations of the studied effect for various orientations of the pulsar orbit relative to the equatorial plane of the Be star. See text for more detail.

cross section, which, under the assumptions made, is equal to

$$\sigma_k = \frac{3\sigma_T}{8\pi\gamma^2}\frac{E^2}{(hv)^2}\frac{1}{(1-\beta\cos\theta_1)^2}, \qquad (8)$$

where σ_T is the Thomson cross section,

$$E = hv\frac{1-\beta\cos\theta_1}{1-\beta}. \qquad (9)$$

We obtain after substituting (4), (6), (8), and (9) into (7)

$$L=\frac{3\sigma_T h}{\pi c^3}\frac{s-2}{\gamma_{\min}^{2-s}-\gamma_{\max}^{2-s}}\left[\frac{L_w}{m_e c^2}\right]\int\gamma^{4-s}(1-\beta\cos\theta_1)^2 \tag{10}$$

$$\times\left\{\int\frac{v^3(1-x+x\cos n)\cos n d\vartheta_{\rm Be}d\varphi d\Omega}{\exp\left\{\dfrac{hv}{kT(\vartheta_{\rm Be})}\right\}-1}\right\}dRdvd\gamma.$$

We can see from (10) that the luminosity depends strongly on the angle θ_1 (as the square of $1-\beta\cos\theta_1$). The physical meaning of this dependence is that, if the photons and relativistic particles are moving in the same direction, there will be very few collisions, and if a collision does occur, little energy will be transfered from the particle to the photon. If the photons and particles move in opposite directions, the number of collisions is increased, and the transfer of energy from the relativistic particles to the photons will be much more efficient.

Thus, in addition to the studied dependence of the X-ray luminosity on the position of the Comptonization point above the Be star, there is, in general, another effect that acts in the same sense and is obviously much stronger [10]. However, we can still determine the strength of the effect in which we are interested, since the two effects will display different periodicities.

5. COMPUTATION RESULTS

When computing the X-ray luminosity, we first determined the position of the pulsar relative to the Be star, then determined the direction of the line of sight. Further, the luminosity was numerically integrated along the line of sight using (10), taking into account the variations of the relative orientation of the Comptonization point and Be star with increasing distance from the pulsar. A specialized computer program was written for the numerical solution of this problem.

Since we are interested in X-ray radiation, we considered only scattered photons with energies from 1 to 10 keV.

When constructing the X-ray light curves, we assumed that the observer views the Be star along its equatorial plane. The length of the integration along the line of sight was taken to be 10^{14} cm. The focal parameter of the pulsar orbit was 1.5×10^{14} cm for circular and 1.5×10^{15} cm for elliptical orbits.

The computation results are presented as a set of plots for various orientations of the pulsar orbit relative to the equatorial plane of the Be star (Fig. 2), as listed below.

(1) The orbit is inclined 90°, and the plane of the orbit is perpendicular to the line of sight. The luminosity does not depend on the angle θ_1, since this angle is the same for any position of the pulsar (Fig. 2a).

(2) The orbit is inclined 60°, and both effects are superimposed (Fig. 2b). The curve for a nonrotating star (dotted) is presented for comparison.

(3) The pulsar orbit lies in the equatorial plane of the Be star (рис. 2c). Only the dependence on the angle θ_1 can be seen (the opposite situation to Fig. 2a).

(4) For the orbit from case 1, plots of the dependence of the relative magnitude of the studied effect on the linear (at the equator) and angular speeds of rotation of the Be star are shown (Figs. 2d, 2e). All the other curves were computed for the maximum speed (368.3 km/hour, or 0.000049 s^{-1}) for the angular frequency).

(5) The pulsar orbit is inclined 85° (Fig. 2f). The two effects are comparable; consequently, their differing periodicities should be easily visible. The light curve for a stationary star (dotted) is shown for comparison. The pulsar orbit was taken to be circular in the computations shown in Figs. 2a–2f.

(6) The pulsar orbit is elliptical and inclined 90°. The configuration of the system is chosen so that the pericenter is located above the equator of the Be star. In Fig. 2g, the eccentricity is equal to 0.1, while the eccentricity in Fig. 2h is equal to that of the PSR B1259–63 system (0.87).

6. CONCLUSIONS

It is clear from the plots that the studied theoretical dependence of the X-ray radiation on the mutual positions of the components of the system is indeed present. The maximum relative magnitude of this effect $L_{\max}/L_{\min}$ grows appreciably with increasing rotational velocity of the Be star and can reach the value two.

When the X-ray luminosity depends strongly on the angle θ_1, the X-ray light curve that is obtained taking into account the uneven heating of the Be star has a different shape than the curve that is obtained for a B-star companion (as long as the plane of rotation of the Be star and the orbital plane of the pulsar are not coincident): the rise and fall of the light curve before and after the maximum are more rapid. If both effects are of the same order, their different periodicities are manifest—a second maximum appears in addition to the main maximum.

If the orbit is very eccentric (but the inclination of the pulsar orbit is about 90°), the studied effect is still observed. In the case of small orbital inclinations, the

shape of the X-ray light curve will remain different from that for a B-star companion, but there will not be a secondary maximum or minimum.

REFERENCES

1. V. G. Kornilov and V. M. Lipunov, Astron. Zh. **61**, 686 (1984) [Sov. Astron. **28**, 402 (1984)].
2. V. M. Lipunov and M. E. Prokhorov, Astron. Zh. **64**, 1189 (1987) [Sov. Astron. **31**, 624 (1987)].
3. V. M. Lipunov, K. A. Postnov, and M. E. Prokhorov, Astrophys. Space Phys. Rev. **17**, 1 (1996).
4. N. V. Raguzova and V. M. Lipunov, Astron. Zh. **75**, 857 (1998) [Astron. Rep. **42**, 757 (1998)].
5. D. Lai, in *Proceedings of the 18th Texas Symp. on Relativistic Astrophysics, Chicago, 1998*.
6. S. Johnston, R. N. Manchester, A. G. Lyne, *et al.*, Astrophys. J. **387**, L37 (1992).
7. S. Johnston, A. G. Lyne, R. N. Manchester, *et al.*, Mon. Not. R. Astron. Soc. **255**, 401 (1992).
8. M. A. Chernyakova and A. F. Illarionov, Mon. Not. R. Astron. Soc. **304**, 359 (1999).
9. A. I. Bogomazov, in *Proceedings of International Conference of Undergraduate and Post-Graduate Students on Abstract Sciences "Lomonosov 2001," Moscow, 2001*; Diploma Work (Moscow State Univ., Sternberg Astronomical Institute, Moscow, 2001).
10. M. A. Chernyakova, Candidate's Dissertation in Physics and Mathematics (Astro Space Center, Lebedev Physical Institute, Moscow, 2000).

Translated by D. Gabuzda

Astronomy Reports, Vol. 47, No. 10, 2003, pp. 826–830. Translated from Astronomicheskiĭ Zhurnal, Vol. 80, No. 10, 2003, pp. 896–901.

Rotational Mass Loss by Be Stars

A. V. Tutukov and A. V. Fedorova

Institute of Astronomy, Moscow, Russia

Received March 27, 2003; in final form, May 8, 2003

Abstract—We have carried out a numerical study of rotational mass loss by rapidly rotating Be stars assuming preservation of rigid-body rotation during their main-sequence evolution. Evolutionary models are computed for stars with solar chemical composition and initial masses of 3, 10 and 30 $M_\odot$. As a result of their rapid initial rotation, these stars can lose one to four percent of their initial mass during the main-sequence stage. The amount of mass lost increases with the initial mass of the star. The matter lost by Be stars can form gas–dust disks with masses comparable to the masses of planets, which, in principle, makes possible the formation of planetary systems around such stars. © *2003 MAIK "Nauka/Interperiodica".*

1. INTRODUCTION

The classical topics of modern observational astronomy include Be stars, in which the usual spectra of B stars are superposed with emission lines, indicating the presence of a large amount of gas in the vicinity of the star. This gas forms a circumstellar gaseous disk. Emission lines can be found in the spectra of main-sequence (MS) stars of almost all spectral types. For instance, Oe, Ae, Fe, Ge, and Me stars are known. Thus, the presence of circumstellar disks is, to various extents, characteristic of almost all MS stars. For this reason, we will assume that Be stars are MS stars with rotationally supported circumstellar disks. The masses of Be stars are confined to the range 3–18 $M_\odot$. The fraction of B stars with emission lines in their spectra is $\sim$20% [1, 2]. It is possible that this fraction depends on the abundance of metals. For the stars of the Small Magellanic Cloud, this fraction increases to $\sim$40% [2], for reasons that remain unclear.

At least for some Be stars, it is likely that the formation of their circumstellar envelopes is due to mass loss. The mass-loss rates of several Be stars have been estimated. For X Persei with $T_{\rm eff} = 31\,000$ K, $\log g = 4$, and $R = 9\ R_\odot$ the mass-loss rate is $\sim 5 \times 10^{-9}\ M_\odot$/yr [3]. The star's parameters suggest that the mass of X Persei is $\sim(10–15)\ M_\odot$. Assuming that the MS lifetime of such a star is $\sim 10^7$ yr, we can estimate the total amount of mass lost by the star in the course of its MS evolution, $\sim 0.05\ M_\odot$. It is evident that such mass loss does not significantly influence the evolution of the star.

Let us consider the main approaches to studies of the Be-star phenomenon. Some Me, Ge, Fe, Ae, and Be stars may be young objects that are accreting the remains of their protostellar envelopes. This is relevant first and foremost in connection with Herbig Ae and Be stars. It is interesting that, in this case, the protostellar material can fall into the close vicinity (within several stellar radii) of the accreting star. Later, due to viscosity, the outer parts of the initially compact disk expand and attain the size of the protoplanetary cloud, $\sim$100 AU [4]. One example of such a star is the Ae star HD 34282 [5] with a mass of $\sim 2\ M_\odot$, which has a gas–dust disk with a mass of $\sim 0.1\ M_\odot$ and a radius of $\sim$800 AU. Such disks are typical of young Ae and Be stars [6]. The peculiarities of the chemical compositions of circumstellar disks suggest that planets may be present in at least some of them, such as the disk of HD 160546 [7]. Naturally, the outer parts of accretion–decretion disks not only survive until the central star arrives on the main sequence, but continue to exist over the entire lifetime of the star, providing, in principle, the possibility of forming planetary systems.

Let us continue to consider the formation of circumstellar gaseous disks. About 50% of stars are members of close binary systems [9]. Over the Hubble time, the components of binaries with masses greater than $\sim 1\ M_\odot$ expand and transfer some fraction of their matter to their companions. This matter forms an accretion disk, as in classical Algols. Examples of such binaries containing Be stars are provided by the semi-detached systems V 360 Lac (B3e + F9IV) [10] and HD 50123 (B6Ve + KIII) [11]. The orbital periods of Be stars in known binary systems lie in the range 5–400 day [12]. Up to $\sim$30% of Be stars have various types of degenerate dwarfs as companions [13]. One example is γ Cas, which is a Be + WD system [14]. Some fraction of Be stars may have neutron stars or black holes as companions [13]; one example is LS1 + 61°303 [15]. It is interesting that the variability of some Be stars may be due to the orbital motion

1063-7729/03/4710-0826$24.00

of the binaries to which they belong and quasi periodic activity of their mass-losing companions, as is observed for FY CMa [16]. It is evident that, after the cessation of mass transfer, the relic gaseous disks around the accreting components of close binaries rapidly dissipate. However, they can exist for comparatively long times in wide binaries and may be transformed into protoplanetary disks if they have enough time.

Let us consider two other possible mechanisms for the formation of circumstellar gaseous disks around rapidly rotating stars with radiative envelopes. Analysis of the initial semi-major orbital axes of close binaries as a function of the primary masses indicates that, in the course of their accretion as they are forming, the semi-major axes of young binaries follow an $a \sim M_1^{1/3}$ law, where M_1 is the mass of the primary. Since the radii of MS stars with $M_1 \gtrsim 1.5\ M_\odot$ increase as $M_1^{2/3}$, some of the closest MS binaries with $M_1 \gtrsim 10\ M_\odot$ merge, forming configurations with two nuclei [13]. No systems of this kind have been observed as yet; it may be that they should be searched for among early-type contact binaries with periods close to or slightly shorter than one day. The coalescence of the nuclei in such "binuclear" stars should result in the outward diffusion of angular momentum and the formation of a circumstellar decretion disk. Observationally, such a system would be manifest as a B star with emission lines in its spectrum.

The last possible mechanism for the formation of circumstellar gaseous disks, which is the topic of the present study, is the diffusion of the angular momentum of a star that evolves along the main sequence while maintaining rigid-body rotation [17]. Qualitative estimates have shown that, for a star with a radiative envelope, the ratio of the angular velocity and the break-up velocity increases as the star evolves along the main sequence. For sufficiently rapid initial rotation, this should lead to continuous mass loss during the star's evolution from point A of its evolutionary track to point B and further to point C (see Fig. 1). The mass-loss rate is especially high in the B to C portion of the track. When the star begins to expand after leaving the main sequence, rotational mass loss terminates. In this simple model, we cannot exclude the possibility that some excess angular momentum is stored by the young star in its inner dense layers, which can rotate faster than the envelope. This effect can enhance the total mass-loss by a factor of a few.

Observations of Be stars provide some evidence in favor of this last explanation for their mass loss. The study of Be stars in extremely young clusters [18] has shown that these stars are concentrated toward early subtypes, characteristic of stars that are leaving the main sequence. The more detailed study [19] showed

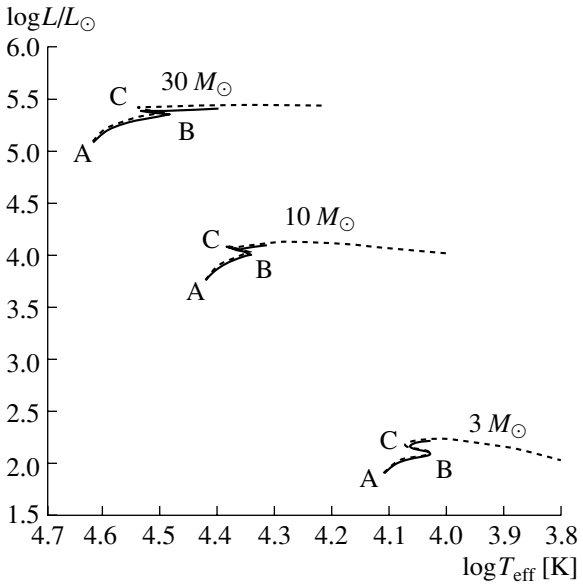

Fig. 1. Evolutionary tracks of stars in the Hertzsprung–Russell diagram. The solid curves show sections of tracks corresponding to the phase of rotational mass loss. The dashed curves show sections of tracks without mass loss. The numbers by the tracks indicate the initial masses of the stars. The letters mark points A, B, and C of the evolutionary tracks.

that Be stars are present only in clusters with ages of $(1.3–2.5) \times 10^7$ yr, which corresponds to the MS lifetimes of stars with masses $\sim 10\ M_\odot$. Thirty-two stars in the cluster h and χ Persei have masses of the same order of magnitude [20]. Finally, the detailed study of the rotation of 1092 main-sequence B stars led Abt *et al.* [21, 22] to conclude that the rigid-body rotation of the stars was preserved right up to the stages when the stellar radii expand to about four times their Zero Age Main Sequence (ZAMS) radii. Thus, we can indeed consider a massive ($\gtrsim 2\ M_\odot$) star to rotate as a rigid body in the course of its MS evolution, even though its radius may grow by a factor of two. The mechanism that sustains the rigid-body rotation has not been clearly established; it may be associated with the magnetic field of the star.

2. COMPUTATION RESULTS

We can numerically study mass loss by rapidly rotating stars using the law of conservation of angular momentum, $I\omega = \text{const}$, where I is the star's momentum of inertia and ω is the angular velocity of its rigid-body rotation. To estimate the equatorial mass loss, we assume that the matter lost by the star carries away a specific angular momentum equal to $\omega_{\rm cr}^2 R$, where R is the instantaneous radius of the star and $\omega_{\rm cr}$ is the break-up angular velocity. The resulting

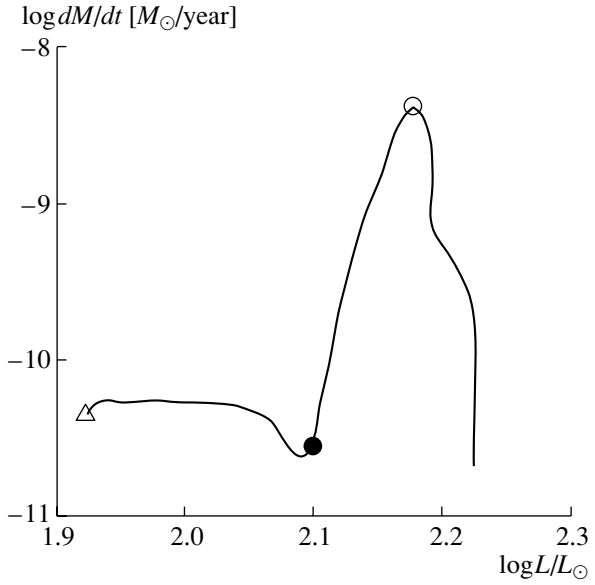

Fig. 2. Dependence of the rate of rotational mass loss on stellar luminosity for a star with initial mass 3 $M_\odot$. The triangle corresponds to point A, the filled circle to point B, and the open circle to point C.

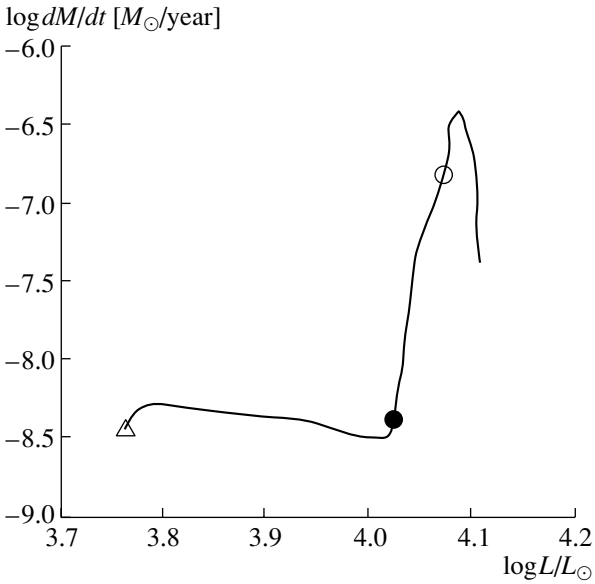

Fig. 3. Same as Fig. 2 for a star with initial mass 10 $M_\odot$.

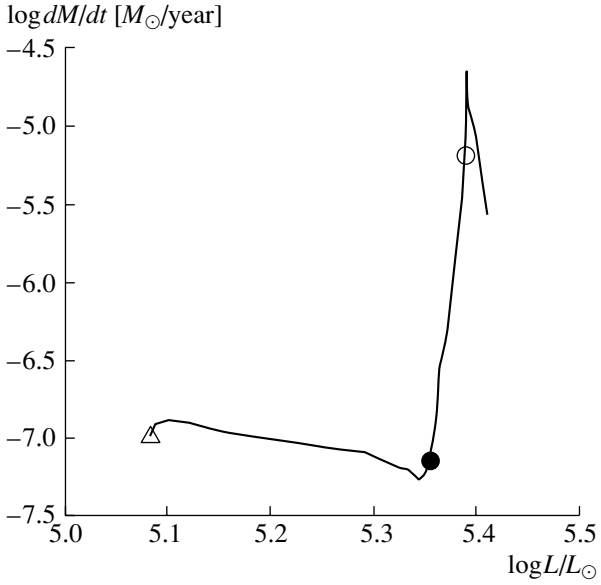

Fig. 4. Same as Fig. 2 for a star with initial mass 30 $M_\odot$.

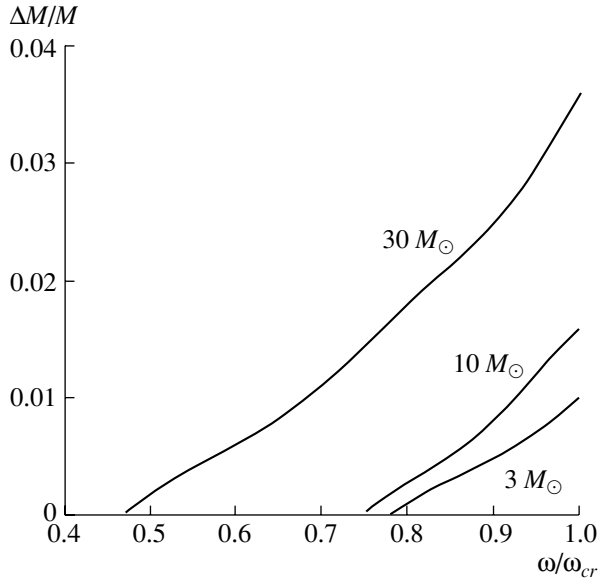

Fig. 5. Fraction of mass lost by a star as a function of the initial ratio of the stellar angular velocity to the break-up velocity assuming rigid-body rotation. The numbers indicate the initial masses of the stars.

equation for the mass-loss rate of a star rotating at the stability limit is

$$\frac{dM}{dt} = \frac{I}{R^2}\left(\frac{d\ln I}{dt} - \frac{3}{2}\frac{d\ln R}{dt}\right)\left(1 - \frac{I}{2MR^2}\right)^{-1}. \quad (1)$$

This equation is valid only when $dM/dt < 0$ and the angular velocity exceeds the break-up velocity. These conditions hold for a star evolving on the main sequence if its rotation on the ZAMS was sufficiently fast [17].

Our analysis is only approximate, since our models are one-dimensional. Moreover, we assume that equatorial mass loss begins only when the star attains the break-up velocity, while, in reality, mass loss probably starts earlier, due to radiation pressure and possible pulsations. Therefore, our results should be

considered only preliminary numerical estimates of the rate of rotational mass loss.

We carried out computations for MS stars with solar chemical composition ($X = 0.70$, $Y = 0.28$, $Z = 0.02$) and initial masses of 3, 10, and 30 $M_\odot$. Evolutionary tracks were computed for the MS phase and further, to the termination of the rotational mass-loss. For comparison, we computed evolutionary tracks for stars with constant mass. Figure 1 presents the tracks of mass-losing stars and stars with constant mass in the Hertzsprung–Russell diagram. We can see that the rotational mass loss is evolutionarily insignificant and does not appreciably change the tracks of the stars.

Figures 2, 3, and 4 show the dependence of the rate of rotational mass loss on the stellar luminosity. We can clearly see that the mass-loss rate is relatively small in the first stage of evolution, from the ZAMS to point B, but grows appreciably in the next evolutionary stage, from point B to point C. Note that the estimated mass-loss rate for X Persei given in the Introduction ($\sim 5 \times 10^{-9}\ M_\odot$/yr [3]) is in fairly good agreement with our estimate of the mass-loss rate for a star with initial mass 10 $M_\odot$ in the first, longest, phase of evolution (Fig. 3).

In Fig. 5, we show the dependence of the fraction of mass lost by the star on the ratio of the initial and break-up angular velocities. The minimum values of this ratio for which rotational mass loss occurs are 0.78, 0.75, and 0.47 for stars with initial masses of 3, 10, and 30 $M_\odot$, respectively. Note that nonuniform rotation of a star on the ZAMS can significantly reduce the initial rotational velocity necessary for mass-loss. Figure 5 clearly shows that the fraction of mass lost due to rotation increases with increasing stellar mass. This can be explained by the properties of the cores of MS stars of different masses. The higher the mass of the star, the higher the mass of the contracting helium core in the final phases of the star's MS evolution. This results in a stronger reduction of the star's moment of inertia and, hence, in the acceleration of its rotation.

3. CONCLUSIONS

Our computations have shown that a Be star can lose 1–4% of its initial mass in the course of its MS evolution if the initial velocity of its rotation was close to the break-up velocity and the rotation itself was rigid-body. Let us consider some consequences of rotational mass loss. It is obvious that the matter lost by the star due to rotation initially forms a compact gaseous disk. This disk will expand in the course of time due to friction and will probably partially evaporate [4, 23, 24]. Observational studies of several Be stars has revealed the formation and expansion of gaseous rings around them [23, 25]. By analogy with the accretion–decretion disks observed around Herbig Ae and Be stars [26], which are occasionally eclipsed by dust clouds when the line of sight coincides with the orbital plane [27], it seems likely that the formation of dust is possible in the outer parts of the disk as it expands and cools. If the mass of the central star does not exceed $\sim 10\,M_\odot$, its lifetime is also sufficiently long for the formation of large planets at the edge of the dust-forming region [9].

We can estimate the masses of the extended gaseous decretion disks around the stars under investigation, m_d, using the condition of conservation of angular momentum. As a result, we obtain $m_d = \Delta M (R/A)^{1/2}$, where $\Delta M \approx 0.03M$ is the total amount of matter lost by the star, R is the star's radius, and A is the radius of the disk. If we assume that $A \approx 100$ AU [5], then $m_d/M \approx 3 \times 10^{-4}$; i.e., when $M \approx (2\text{–}20)\,M_\odot$, the mass of the disk is comparable to the masses of solar and extrasolar planets [4]. If we assume that one condition for the formation of a planet is the condensation of dust at $T \approx 1500$ K, the position of the closest planet becomes a function of the mass of central star [9]. For $L/L_\odot \approx (M/M_\odot)^4$, the distance to the dust-condensation zone is $A \approx 0.1(M/M_\odot)^2$, and $m_d/M_\odot \approx 0.01(M/M_\odot)^{1/3}$, if the stellar radius is $R/R_\odot \approx (M/M_\odot)^{2/3}$. Thus, in this case as well, the mass of the gaseous disks is comparable to the masses of planets.

Generally speaking, judging from the positions of massive planets in extrasolar systems, dust formation may not be a necessary condition for the formation of planets. In this case, given the low viscosity of the disk material, we cannot rule out the development of gravitational instability in the compact, dense disks and the formation of brown dwarfs [4, 28] with probable masses of $\approx 0.01\ M_\odot$.

When estimating the role of rotational mass loss by MS stars, we should bear in mind other possible mechanisms for the loss of mass and angular momentum. First and foremost, this concerns mass loss via the stellar wind, which is most efficient for massive stars. Conti [29] and Stothers [30] provide a compilation of observational estimates of mass-loss rates by OB stars, which can be approximated by the analytical expression

$$\dot{M}_{\rm OB} = 10^{-20} \left(\frac{L_{\rm OB}}{L_\odot} \right)^{2.5} M_\odot/\text{yr}. \qquad (2)$$

Since $L_{\rm OB} \approx 10^2 (M_{\rm OB}/M_\odot)^2 L_\odot$ [31], and the MS lifetimes of OB stars are $\tau_{MS} \sim 3\times$

$10^7(M_{\rm OB}/M_\odot)^{-1/2}$ yr [31], the total mass loss in the MS stage of a star's evolution does not exceed

$$\frac{\Delta M_{\rm OB}}{M_{\rm OB}} \lesssim 3\times 10^{-8}(M_{\rm OB}/M_\odot)^{4.5}. \qquad (3)$$

Comparing this mass loss to the amount of mass lost due to rotation for the most massive stars ($\sim 0.1M_{\rm OB}$), we find that mass loss due to the stellar wind is negligible compared to rotational mass loss when $M_{\rm OB} \lesssim 30M_\odot$. This justifies our neglect of stellar-wind mass loss in this study.

It is interesting that two rapidly rotating Ae stars that have been studied in detail, ν Cyg and κ UMa, display a luminosity excess of one magnitude compared to ZAMS stars [32]. A special analysis [32] has shown that these stars are not young; i.e., they are not Herbig–Haro objects. Hence, these stars have had time to evolve to some extent. This result is consistent with our conclusions that rotational mass loss by Ae and Be stars becomes most efficient for stars are leaving the main sequence (Figs. 2–4) and that rotational mass loss occurs in the vicinity of point C of the evolutionary tracks, even for stars that rotated on the ZAMS with velocities comprising 50–70% of the break-up velocity (Fig. 5).

Other possibilities for enhancing the rotational mass loss of rapidly rotating stars and supporting their circumstellar gaseous disks appear if we consider the possible presence of a close companion to the Be star [33]. If the rotation of the star is not synchronized with the orbital motion, the presence of a close companion may facilitate the mass loss and modify the shape of the Be-star envelope.

ACKNOWLEDGMENTS

The authors thank A.A. Boyarchuk for discussions of problems associated with Be stars. This work was supported by the program "Leading Scientific Schools" (grant 00-15-96722), the State Science and Technology Program "Astronomy," the Program of the Presidium of the Russian Academy of Sciences "Nonstationary Phenomena in Astronomy," and the Russian Foundation for Basic Research (project code 03-02-16254).

REFERENCES

1. J. Zonec and D. Briot, Astron. Astrophys. **318**, 443 (1997).
2. A. Maeder *et al.*, Astron. Astrophys. **346**, 459 (1999).
3. J. Telting *et al.*, Mon. Not. R. Astron. Soc. **296**, 785 (1998).
4. A. V. Tutukov, Astron. Rep. **46**, 691 (2002).
5. V. Pietu, A. Dutrey, and G. Kahane, astro-ph/0210097 (2002).
6. J. Vink *et al.*, Mon. Not. R. Astron. Soc. **337**, 356 (2002).
7. J. Bouwman *et al.*, astro-ph/0301254 (2003).
8. L. Waters and C. Waelkens, Ann. Rev. Astron. Astrophys. **36**, 233 (1998).
9. A. G. Masevich and A. V. Tutukov, *Star Evolution: Theory and Observations* (Nauka, Moscow, 1988) [in Russian].
10. G. Hill *et al.*, Astron. Astrophys. **324**, 965 (1997).
11. C. Sterken, N. Vogt, and R. Mennickont, Astron. Astrophys. **291**, 473 (1994).
12. F. Carrier, G. Burki, and M. Burnet, Astron. Astrophys. **385**, 48 (2002).
13. A. V. Tutukov and L. R. Yungel'son, Astron. Zh. **79**, 738 (2002) [Astron. Rep. **46**, 667 (2002)].
14. K. Apparao, Astron. Astrophys. **382**, 554 (2002).
15. P. Gregory and C. Neish, Astrophys. J. **580**, 1133 (2002).
16. G. Peters, ASP Conf. Ser. **232**, 227 (2003).
17. A. V. Tutukov, Nauch. Inform. Astron. Sovet Akad. Nauk SSSR **11**, 62 (1969).
18. G. Peters, ASP Conf. Ser. **292**, 65 (2003).
19. J. Fabregat and J. Torrejon, Astron. Astrophys. **357**, 451 (2000).
20. A. Bragg and S. Kenyon, Astron. J. **124**, 3289 (2002).
21. H. Abt, H. Levato, and M. Grosso, Astrophys. J. **573**, 359 (2002).
22. H. Abt, Astrophys. J. **582**, 420 (2003).
23. J. Porter, Astron. Astrophys. **348**, 512 (1999).
24. A. Okazaki, Publ. Astron. Soc. Jpn. **53**, 119 (2001).
25. T. Rivinius *et al.*, Astron. Astrophys. **379**, 257 (2001).
26. C. Dullemond, Astron. Astrophys. **395**, 853 (2002).
27. P. The and F. Molster, Astrophys. Space Sci. **212**, 125 (1994).
28. A. Boss, Astrophys. J. **536**, L101 (2000).
29. P. S. Conti, Mem. Soc. R. Sci. Liege **9**, 193 (1976).
30. R. Stothers, Astrophys. J. **568**, 312 (2002).
31. A. V. Tutukov and L. R. Yungel'son, Nauch. Inform. Astron. Sovet Akad. Nauk SSSR **27**, 3 (1973).
32. D. Monin, G. Wade, and S. Fabrika, astro-ph/0304402 (2003).
33. P. Harmanec, D. Bisikalo, A. Boyarchuk, and O. Kuznetsov, Astron. Astrophys. **396**, 937 (2002).

Translated by L. Yungel'son

Astronomy Reports, Vol. 47, No. 10, 2003, pp. 831–837. Translated from Astronomicheskiĭ Zhurnal, Vol. 80, No. 10, 2003, pp. 902–908.

The Characteristics of Blazars That are Sources of Very-High-Energy Gamma Rays

O. R. Kalekin, Yu. I. Neshpor, and A. A. Stepanyan

Crimean Astrophysical Observatory, Nauchnyĭ, Crimea, 98409 Ukraine

Received February 25, 2003; in final form, May 8, 2003

Abstract—We show that the most probable extragalactic sources of very-high-energy gamma rays are HBL blazars whose peak frequencies are in the X-ray. The detection of very-high-energy gamma rays from the blazar 3C66A, which has a redshift of $z = 0.44$, suggests that the density of the intergalactic infrared background at wavelengths > 0.6 μm is lower than estimates published in the literature.

1. INTODUCTION

Blazars are one type of active galactic nuclei (AGNs). Interest in these sources rose sharply after the discovery that many sources of high-energy (> 100 MeV) gamma rays detected by the Compton Gamma-Ray Observatory (CGRO) are identified with AGNs [1]. These AGNs were subsequently observed using ground-based detectors sensitive to very-high-energy (VHE; 10^{11}–10^{13} eV) gamma rays.

The nature of objects in which particles are accelerated to VHE is of considerable interest. It is known that particles with energies up to 10^{20} eV are present among the cosmic rays. It is currently unclear in which astrophysical objects particles can be accelerated to such energies. CGRO observations [1] showed that many sources of high-energy gamma rays are AGNs, primarily quasars and BL Lac objects. The question of the energies to which particles can be accelerated in AGNs remains open, and observations of AGNs using ground-based detectors of VHE gamma rays can help resolve this problem.

2. KNOWN SOURCES OF VHE GAMMA RAYS

Currently, eight AGNs have been detected as sources of VHE gamma rays. The first firm detections of VHE gamma rays from AGNs were obtained using the 10-m ground-based Cherenkov detector of the Whipple Observatory in the USA: the Markarian galaxies Mrk 421 ($z = 0.031$) and Mrk 501 ($z = 0.034$) [2]. In both cases, the fluxes involved were very small—approximately 0.08 times the flux of the Crab Nebula (0.08 Crab) for Mrk 501 and 0.4 Crab for Mrk 421 [2]. However, in Spring 1997, the VHE gamma ray flux from Mrk 501 grew by more than a factor of 15 compared to its quiescent state, reaching 1.5–2.0 Crab [2, 3].

VHE gamma rays from the blazar 3C 66A ($z = 0.444$) were detected at the Crimean Astrophysical Observatory (CrAO) [4], as well as from Mrk 421 and Mrk 501, which are BL Lac objects—one relatively small group of AGNs, whose prototype is the object BL Lac. Observations of this source at the CrAO in 1998 [5] indicated the detection of VHE gamma rays at the 7.2σ level.

Two more sources of VHE gamma rays were also detected using the 10-m Whipple telescope—1H 1426+428 ($z = 0.129$) and PKS 2344+514 ($z = 0.044$), which are also classified as BL Lac objects. The former was detected in observations in 2000 and 2001 [6], and the latter in observations in 1997 [7]. Finally, the group of Durham University detected VHE gamma rays from the blazar PKS 2155–304 [8] ($z = 0.117$), and VHE gamma rays were detected from the BL Lac object 1ES 1959+650 ($z = 0.048$) using the Seven Telescope Array [9].

A brief summary of information about the VHE gamma ray sources is presented in Table 1. All the detected sources can be considered BL Lac objects.

3. CHARACTERISTICS OF BL LAC OBJECTS

The optical spectra of BL Lac objects are dominated by a pure continuum, without significant line emission. The power-law character of the spectra and the strong optical polarization of the radiation, which can reach 30%, suggests that the observed radiation is synchrotron radiation generated by charged particles that have been accelerated to VHE. The absence of large quantities of gas (there are no emission lines) and the synchrotron character of the spectrum

1063-7729/03/4710-0831$24.00

Table 1. Sources of VHE gamma rays

Object	Class	z	$\log \gamma_{\max}$
3C 66A 0219+428	LBL	0.444	5.0
Mk 421 1101+384	HBL	0.031	5.9
1H 1426+428	HBL	0.129	
Mk 501 1652+398	HBL	0.034	5.9
1ES 1959+650	HBL	0.048	
PKS 2155−304	HBL	0.116	5.6
BL Lac 2200+420	LBL	0.069	5.5
1ES 2344+514	HBL	0.044	5.8

suggest that the observed radiation is emitted in the innermost parts of the central source.

Brightness variability reaching 4^m–5^m in the optical (luminosity variations of up to a factor of 100) is characteristic of BL Lac objects. All BL Lac objects also emit significant radio emission, which is, as a rule, variable. Variability in the flux of VHE gamma rays is also observed. The very first two blazars detected as sources of VHE gamma rays—Mrk 421 and Mrk 501—showed appreciable variability [2, 3]. Variability has also been detected in the flux of VHE gamma rays from 3C 66A [10], with the VHE gamma ray flux being correlated with the optical brightness. The optical and radio variability of the blazar BL Lac is well known; VHE gamma rays were detected only during a flare in July 1998. The characteristic variability time scales of weeks and months, and sometimes even days [11], can be used to estimate the size of the region radiating the gamma rays to be of the order of 10^{16} cm. Ghisellini *et al.* [12] considered two models for blazars that suppose that the optical, X-ray, and gamma ray emission is radiated by high-energy particles in a jet that propagates from the central region of the AGN with a speed that is close to the speed of light. The optical emission is synchrotron radiation by relativistic electrons moving in the jet magnetic field. The X-ray and gamma ray emission are due to the Compton interaction between the relativistic electrons in the jet and radiation (the inverse Compton effect). In the first model, the Compton-scattered photons are located in the region surrounding the jet, while, in the second model, the scattered photons are synchrotron radiation from the relativistic electrons moving in the jet magnetic field.

4. OBJECTS PROMISING FOR THE DETECTION OF VHE GAMMA RAYS

In order to fruitfully investigate the nature of objects in which cosmic rays are generated, accompanied by the radiation of VHE gamma rays, it is very desirable to obtain data for a larger number of sources of VHE gamma rays. Since the observing times required to detect the fluxes of VHE gamma rays from AGN are very large, attempts to use data obtained in other parts of the electromagnetic spectrum to predict the most promising sources for observations aimed at detecting VHE gamma rays are extremely valuable. Such attempts have been made for a number of years. Calculations of VHE gamma ray fluxes based on the hypothesis that the gamma rays are generated by Compton scattering of the jet synchrotron photons by the radiating relativistic particles themselves (synchrotron self-Compton scattering) are presented in [13]; calculations were carried out for 23 X-ray selected BL Lac objects (XBLs) from the Third EGRET Catalog. This list of 23 objects did not include sources with $z > 0.1$, since the authors expected the absorption of VHE gamma rays by the intergalactic background to drastically weaken the observed flux of such gamma rays. At the time when it was hypothesized that VHE gamma rays might be expected from X-ray selected objects, only two sources of VHE gamma rays were known: Mrk 421 and Mrk 501. Of the six objects that were subsequently detected, three are included in the list of [13]—1ES 2155−304, 1ES 2344+514, and 1ES 1959+650 [13].

Currently, due to the availability of more extensive data, the possibility has arisen of better elucidating which objects might be promising candidates for sources of VHE gamma rays. This aim, we have conducted a comparison of the characteristics of various blazars, considering their energy spectra (the product of the spectral flux density and the frequency). We analyzed the following characteristics of the spectra using the data presented in [12, 14]: their distribution by class of blazar as adopted in [12, 14], the peak frequency of their energy spectra, the maximum intensity at that frequency, and ratios of the fluxes at various frequencies.

5. PROPERTIES OF THE SPECTRAL ENERGY DISTRIBUTIONS OF SOURCES OF VHE GAMMA RAYS

5.1. Blazar Type

In [12], the AGNs that are sources of high-energy gamma rays can be separated into several classes, according to their polarization characteristics (HPQs—high-polarization quasars, and LPQs—low-polarization quasars) or the peak frequency corresponding to their maximum radiation (HBLs—high-energy-peaked BL Lac objects, and LBLs—low-energy-peaked BL Lac objects). Data on the 5-GHz radio fluxes, 5500 Å optical fluxes, 1 keV X-ray fluxes,

and > 100 MeV gamma ray fluxes of 53 blazars are presented in [14]. Comastri *et al.* [14] separate the 53 objects into two types: flat-spectrum radio quasars (37 objects, nearly all of them HPQs or LPQs according to [12]) and BL Lac objects (16 objects, all either HBLs or LBLs according to [12]). All eight currently known sources of VHE gamma rays are BL Lac objects; six are HBLs, while two (3C 66A and BL Lac) are LBLs (see column 2 in Table 1). Note that, during a flare of the blazar 1H 1426+428 [6], a shift of the peak frequency in the X-ray toward higher frequencies was observed simultaneously with variations in the flux of VHE gamma rays. If the peak frequencies of 3C 66A and BL Lac in the X-ray shift toward higher frequencies during optical flares of these objects, it is possible that they would be classified as HBLs at those epochs. It is probable that there are sources of VHE gamma rays among flat-spectrum radio quasars as well, but these sources are virtually all very distant ($z > 0.8$). Therefore, it will be extremely difficult to detect their VHE gamma ray emission using currently available detectors.

5.2. Peak Radiation Frequencies of Blazars

The spectra of virtually all the blazars that have been detected by EGRET [12, 14] have two peaks when the flux of the radiation is presented as the product of the spectral flux density and the frequency. The lower-frequency peak is in the optical or ultraviolet (sometimes in the X-ray), while the higher-frequency peak is in the X-ray or high-energy gamma ray range. As was noted in [15], in the sources of VHE gamma rays, the peak frequencies in the X-ray are higher than those of other BL Lac objects. The measured VHE gamma ray flux is, indeed, reduced by absorption by the intergalactic infrared background accompanied by the formation of pairs, with gamma rays of higher energies being absorbed more strongly. This leads to a shift of the high-frequency peak in the source radiation toward higher frequencies. Thus, one requirement that a blazar be a source of VHE gamma rays is a higher frequency for its maximum radiation in the X-ray.

5.3. Maximum Electron Energy

We compared the maximum electron energies obtained in the blazar models of [12] for sources of VHE gamma rays and for other objects. The maximum electron energies of the sources of VHE gamma rays are higher than those of other blazars. This can be seen in Fig. 1, which presents the Lorentz factors corresponding to the maximum electron energies $\gamma_{\max}$ as a function of the peak frequency in the low-frequency part of the spectrum ($F_m(X)$). The sources of VHE gamma rays are denoted by filled circles. The maximum electron energies ($\gamma_{\max} m_o c^2$) of all the objects exceed 10^{11} eV. As is noted in [12], the maximum energy of the electrons that are responsible for the high-energy gamma ray emission is positively correlated with the peak frequency in the optical, ultraviolet, or X-ray ($E < 1$ keV; the low-frequency peak). We find that the correlation coefficient is very high, $r = 0.95 \pm 0.01$. A good correlation is obtained only for the first model considered in [12] (see Section 3).

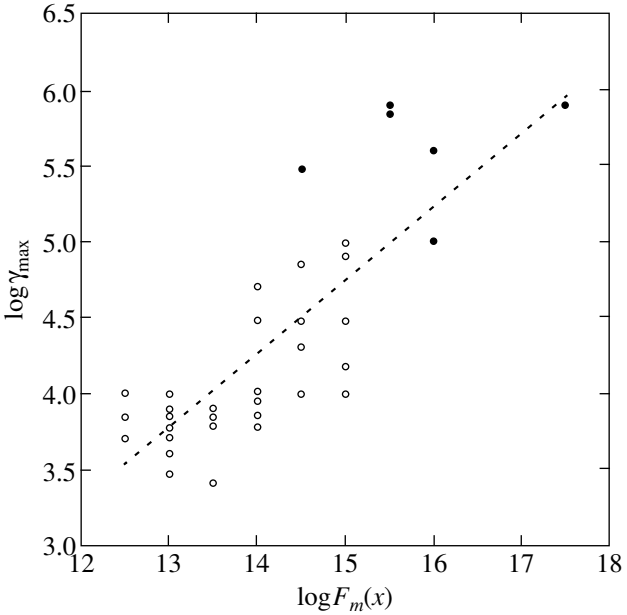

Fig. 1. Correlation between the Lorentz factor of the electrons with the maximum energy $\gamma_{\max}$ and the peak frequency of the low-frequency (synchrotron radiation) part of the spectrum $F_m(X)$. Known sources of VHE gamma rays are shown by the filled circles.

5.4. Ratios of the Fluxes in Various Energy Ranges

As was noted above, all known sources of VHE gamma rays are BL Lac objects. Therefore, we considered further only the data for BL Lac objects presented in [12, 14]. Table 2 presents ratios of the fluxes in various energy ranges for the 16 BL Lac objects in this list, where by "flux" we mean here the product of the spectral flux density and the frequency. $S(X)$, $S(R)$, and $S(\gamma)$ are the products of the frequency and the spectral flux density in the X-ray, in the radio at 5 GHz, and in the high-energy gamma ray range. Analysis of the data of [12, 14] shows (Fig. 2) that the sources of VHE gamma rays radiate relatively more of their energy in the X-ray compared to the radio: $\log (S(X)/S(R) > 1$. This is in agreement with the assumptions made in [13]. We can see from Table 2

Table 2. Flux ratios

Object	Name	$\log\frac{S(R)}{S(\mathrm{opt})}$	$\log\frac{S(X)}{S(R)}$	$\log\frac{S(\mathrm{opt})}{S(X)}$	$\log\frac{S(X)}{S(\gamma)}$
BL Lac objects					
0235+164	AO	−2.4021	1.1221	1.2800	−1.8447
0537−441	PKS	−1.7472	0.9913	0.7559	−1.4765
0716+714	S5	−3.3000	1.7428	1.5571	−1.0141
0735+178	PKS	−2.3140	0.5027	1.8112	−1.5507
0829+046	PKS	−1.9660	1.4967	0.4693	−1.0697
0851+202	OJ 287	−2.2082	1.2403	0.9679	−1.2959
0954+658	S4	−1.7869	0.7510	1.0360	−1.6690
1219+285	ON 231	−2.5131	1.3109	1.2022	−0.9709
1604+159	4C15.54	−1.4524	1.2164	0.2361	−2.1897
2005−489	PKS	−3.3384	2.1151	1.2233	−0.3538
2032+107	PKS	−2.4627	0.7983	1.6643	−2.0050
Sources of VHE gamma rays					
0219+428	3C 66A	−2.6181	1.7647	0.8534	−0.9356
1101+384	Mk 421	−3.4245	3.3504	0.0741	0.5532
1652+398	Mk 501	−2.4036	2.5368	−0.1332	0.2755
2155−304	PKS	−3.9351	3.8960	0.0391	0.3860
2344+514	1ES	−3.0790	2.8603	0.2186	−.1048

that the minimum value of this flux ratio for the VHE gamma ray sources is $\log(S(X)/S(R)) = 1.76$, and we accordingly suggest that such sources should have $\log(S(X)/S(R)) > 1.76$. It also follows from Fig. 2 that the sources of VHE gamma rays are distinguished among other blazars by their ratios $\log(S(X)/S(\gamma))$.

Based on the above analysis, we conclude that blazars that radiate VHE gamma rays should display the following flux ratios, which distinguish them from other BL Lac objects: $\log(S(X)/S(R)) > 1.76$, $\log(S(X)/S(\gamma)) > -1.0$, and $\log(S(R)/S(\mathrm{opt})) < -2.4$.

6. ABSORPTION OF GAMMA RAYS IN INTERGALACTIC SPACE

As noted above, the AGNs that are sources of VHE gamma rays are variable, which appreciably complicates their detection at very high energies. In addition, the flux of VHE gamma rays interacts with intergalactic infrared photons as it propagates through intergalactic space. In spite of the small cross section for photon–photon interactions with the formation of electron–positron pairs, this process can exert a substantial influence on the emitted spectrum of gamma rays due to the huge distances between the Milky Way and other galaxies, affecting the fluxes of VHE gamma rays detected at the Earth. It was noted earlier that it was expected to be possible to detect VHE gamma rays only from objects at distances corresponding to redshifts $z < 0.1$ [13]. However, VHE gamma rays have recently been detected from two more distant objects: the blazar 1H 1426+428 with $z = 0.129$ [6, 16], and the blazar 3C 66A with $z = 0.444$, detected at the CrAO [10].

Calculations of the expected absorption to distances corresponding to redshifts $z = 0.3$ are available in the literature (see, for example, [17, 18]), as well as for some z values corresponding to specific observed objects. For example, Stecker and de Jager [19] calculate the expected absorption for 3C 279, one of the brightest EGRET sources [1], which has $z = 0.54$.

We estimated the absorption expected for $z = 0.444$. Such estimates depend on models for the density of intergalactic photons and the measured values for this density obtained in various

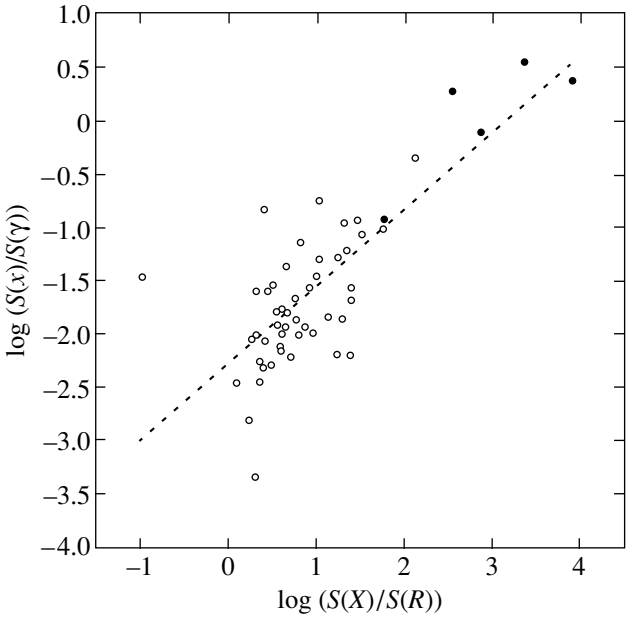

Fig. 2. Dependence of the X-ray/gamma ray flux ratio $\log[S(X)/S(\gamma)]$ on the X-ray/radio flux ratio $\log[(S(X)/S(R)]$. All values are expressed in erg $\mathrm{cm}^{-2}\mathrm{s}^{-1}$.

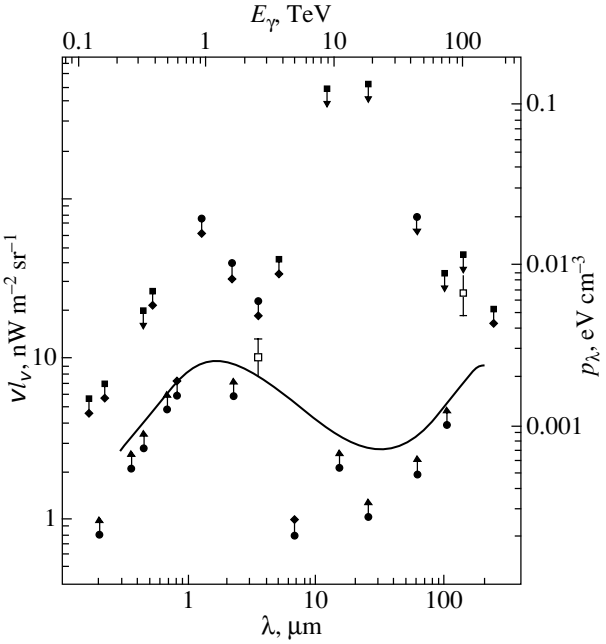

Fig. 3. Dependence of the intergalactic background photons on wavelength. The left scale shows intensity and the right scale energy density.

experiments. Figure 3 presents measurements of the intergalactic photon background in the form of the intensity (or energy density) as a function of wavelength. In our calculations, we used the solid curve in this figure. This curve coincides with the model of de Jager and Stecker [17] at wavelengths of 0.6–200 μm, responsible for the absorption of TeV gamma rays. We have not taken into account evolutionary variations of the spectrum of intergalactic photons at high z. According to the calculations of Salamon and Stecker [20] for wavelengths > 0.4 μm, the photon density begins to drop off with increasing z. For example, at $\lambda = 2$ μm, this density is a factor of three lower at $z = 1$ than at $z \simeq 0.0$. Interpolating this result for $z = 0.44$, we obtain a difference of only about a factor of 1.5. As will become clear from the formulas for the absorption calculations, these variations will not significantly affect the final results.

According to Stecker [21], for gamma rays with energy E radiated at a distance corresponding to the redshift z, the optical depth can be calculated as follows:

$$\tau(E,z) = \frac{3}{8}\sigma\frac{c}{H}\int\limits_0^z \sqrt{1+z} \times \int\limits_{\frac{m_0^2}{E(1+z)^2}}^{\infty} \frac{dn(\varepsilon)}{d\varepsilon} F\left(\frac{m_0^2}{E\varepsilon(1+z)^2}\right) d\varepsilon, \quad (1)$$

where $\sigma = 6.67 \times 10^{-25}$ cm^2 is the Thomson cross section, c the speed of light, H the Hubble constant, taken to be 70 km s^{-1}Mpc^{-1}, $m_0 = 0.51$ MeV the electron mass, $\frac{dn(\varepsilon)}{d\varepsilon}$ the density of intergalactic background photons as a function of their energy, and $F(q)$ a function associated with the integration over all possible angles θ for collisions between the interacting photons,

$$F(q) = 2q^2\int\limits_q^1 f(x)x^{-3}dx. \quad (2)$$

The numerical integration was carried out over the range $0.01 < q < 1$. For $q < 0.01$, we used an asymptotic approximation that introduced an error not exceeding 0.2%: $F(q) \approx 2q\left[\ln\frac{4}{q} - 2 + \frac{1}{2}q\left(\ln\frac{4}{q}\right)^2\right]$, where $q = \frac{m_0^2}{E\varepsilon}\frac{2}{1-cos\theta}$. Together with the power-law character of the photon density at large values of ε, i.e., small values of q, this enables us to calculate the energy integral in formula (1) with an infinite upper limit by obtaining an analytical expression.

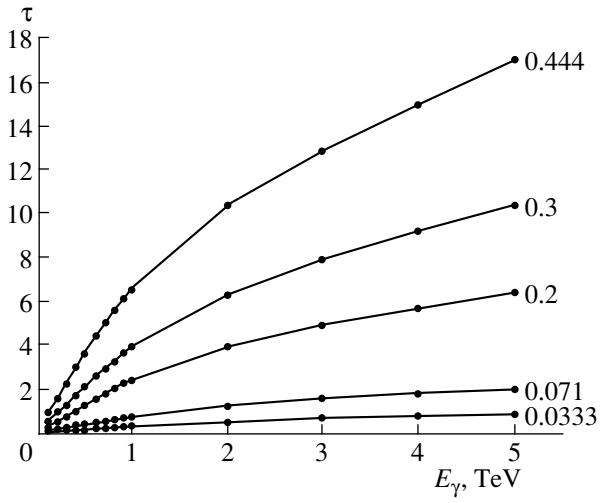

Fig. 4. Dependence of the optical depth on the gamma ray energy for various z.

We calculated the optical depth as a function of the gamma ray energy for objects observed using the CrAO gamma ray telescope: the AGNs Mrk 501 ($z = 0.033$) [6], BL Lac ($z = 0.071$) [5], and 3C 66A ($z = 0.444$) [4]. Plots of these dependences are presented in Fig. 4, which also shows curves for intermediate values of z. We can see from Fig. 4 that the weakening of the TeV flux becomes very substantial for $z = 0.444$, in agreement with the calculations of Stecker and de Jager [19]: they obtained the optical depths $\tau = 5$ for $z = 0.30$ and $\tau = 10$ for $z = 0.54$ for gamma rays with energies of 1 TeV, while our calculations yielded $\tau = 6.6$ for $z = 0.444$. This should lead to cardinal variations in the radiated spectrum. The estimate of the luminosity of VHE gamma rays emitted by 3C 66A obtained by us earlier [10] should, in this case, be increased by approximately three orders of magnitude. These earlier estimates suggested that the luminosity of this object in VHE gamma rays was 10^{46} erg/s, approximately equal to the luminosity in X-rays and high-energy gamma rays (300 MeV–10 GeV). A similar spectra but with an amplitude two orders of magnitude lower is displayed by another object observed at the CrAO—the blazar Mrk 501. Figure 4 shows that the absorption for this source should not be so large ($< 30\%$ at 1 TeV), so that previous estimates of its spectrum remain valid. Thus, if our results are correct, there must be substantial differences in the radiation mechanisms acting in these two objects. In addition, it is known that the powers radiated by different blazars at high energies can differ by two to three orders of magnitude, suggesting that the possibility of detecting VHE gamma ray emission at $z = 0.444$ should not be ruled out. The minimum possible absorption for the radiation of 3C 66A can be estimated from the work of Vasil'ev [18]. The optical depth is presented there as a function of the photon energy and the redshift of the object via the formula

$$\tau(E, z) = c_0(z) + c_1(z)\ln(E/1\ \text{TeV}) + c_2(z)[\ln(E/1\ \text{TeV})]^2. \quad (3)$$

Based on the lowest estimates for the spectral density of intergalactic photons yielded by various experiments (Fig. 3), Vasil'ev [18] derived values for the coefficients c in (3) for z values from 0 to 0.3. Approximating these results for $z = 0.444$, we obtain $\tau = 3$ for energy $E = 1$ TeV, which corresponds to absorption of 95% of the radiation, or a decrease in the flux by only a factor of 20. Thus, our estimate of the luminosity of 3C 66A in VHE gamma rays presented in [10] would have to be raised by only one order of magnitude, which can plausibly be explained by high activity of the source at these energies, without the need to deviate from existing models for the radiation of AGNs. More detailed and precise information about the absorption of gamma rays could be obtained from a reconstruction of the differential energy spectrum observed for 3C 66A; however, the observational data are not sufficient from a statistical point of view to be used for this purpose.

7. CONCLUSIONS

Based on the above analysis, we can conclude that blazars that radiate VHE gamma rays have the following distinguishing characteristics.

They are all HBL BL lac objects with the following characteristic spectral parameters: $\log(S(X)/S(R)) > 1.7$, $\log(S(X)/S(\gamma)) > -1.0$, and $\log(S(R)/S(opt)) < -2.4$. According to the models of [12], essentially all eight objects that are sources of VHE gamma rays have maximum electron energies exceeding 10^{11} eV, while the maximum electron energies of the remaining BL Lac objects are lower than 10^{11} eV. The low-frequency peaks of the VHE gamma ray sources are shifted to the far ultraviolet or soft X-ray compared to the peaks of the other BL Lac objects. The detection of VHE gamma rays from the blazar 3C 66A, which is located at a distance corresponding to $z = 0.44$, suggests that the density of the intergalactic infrared background at wavelengths > 0.6 μm is lower than previously published estimates.

ACKNOWLEDGMENTS

The authors thank S.G. Kochetkovaya, Z.N. Skiruta, and E.M. Nekhaĭ for help in preparation of the manuscript. The study was supported in part by the CRDF grant (VP1-2431-NA-02).

REFERENCES

1. D. J. Thompson, D. L. Bertsch, B. L. Dingus, *et al.*, Astrophys. J., Suppl. Ser. **101**, 259 (1995).
2. J. Quinn, C. W. Akerlof, S. Biller, *et al.*, Astrophys. J. **456**, L83 (1996).
3. F. Aharonian, A. G. Ahperjanian, J. A. Barrio, *et al.*, Astron. Astrophys. **327**, L5 (1997).
4. Yu. I. Neshpor, A. A. Stepanyan, O. R. Kalekin, *et al.,* Pis'ma Astron. Zh. **24**, 167 (1998) [Astron. Lett. **24**, 134 (1998)].
5. Yu. I. Neshpor, N. N. Chalenko, A. A. Stepanyan, *et al.,* Astron. Zh. **78**, 291 (2001) [Astron. Rep. **45**, 249 (2001)].
6. D. Horan, H. M. Badran, I. H. Bond, *et al.*, *Proc. of the 27th International Cosmic Ray Conference,* Ed. by V. Simon, E. Lorenz, and M. Pohl (IUPAP, Hamburg, 2001), Vol. 7, p. 2622.
7. M. Catanese, C. W. Akerlof, H. M. Badran, *et al.*, Astrophys. J. **501**, 616 (1998).
8. P. M. Chadwick, K. Lyons, T. J. L. McComb, *et al.*, Astrophys. J. **513**, 161 (1999).
9. T. Nishiyama, N. Chamoto, M. Chikawa, *et al.*, *Proc. of the 26th International Cosmic Ray Conference*, Ed. by B. L. Dingus, D. B. Kieda, and M. H. Salamon (AIP, Salt Lake City, 2000), Vol. 3, p. 370; AIP Conf. Proc. **515**, 134 (2000).
10. A. A. Stepanyan, Yu. I. Neshpor, N. A. Andreeva, *et al.*, Astron. Zh. **79** (8), 702 (2002) [Astron. Rep. **46**, 634 (2002)].
11. O. R. Kalekin, N. N. Chalenko, Yu. L. Zyskin, *et al.*, Izv. Ross. Akad. Nauk, Ser. Fiz. **63**, 606 (1999).
12. G. Ghisellini, A. Celotti, G. Fossati, *et al.*, Mon. Not. R. Astron. Soc. **301**, 451 (1998).
13. F. W. Stecker, O. C. De Jager, and M. N. Salomon, Astrophys. J. **473**, 75 (1996).
14. A. Comastri, G. Fossati, G. Ghisellini, and S. Molendi, Astrophys. J. **480**, 534 (1997).
15. Y. C. Lin, D. L. Bertsch, S. D. Bloom, *et al.*, Astrophys. J. **525**, 191 (1999).
16. D. Horan, H. M. Badran, I. H. Bond, *et al.*, Astrophys. J. **571**, 753 (2002).
17. O. C. de Jager and F. W. Stecker, astro-ph/0107103.
18. V. V. Vassiliev, Astropart. Phys. **12**, 217 (2000).
19. F. W. Stecker and O. C. de Jager, Astrophys. J. **476**, 712 (1997).
20. M. H. Salamon and F. M. Stecker, Astrophys. J. **493**, 547 (1998).
21. F. W. Stecker, *Cosmic Gamma Rays* (Mono Book, Baltimore, 1971).

Translated by D. Gabuzda

Astronomy Reports, Vol. 47, No. 10, 2003, pp. 838–847. Translated from Astronomicheskiĭ Zhurnal, Vol. 80, No. 10, 2003, pp. 909–918.

Long-Term Monitoring of the Water-Vapor Maser in NGC 7538: 1981–1992

E. E. Lekht[1,2], V. A. Munitsyn[3], and A. M. Tolmachev[4]

[1] *Instituto Nacional de Astrofísica, Óptica y Electrónica, Luis Enrique Erro No. 1, Apdo Postal 51 y 216, 72840 Tonantzintla, Puebla, México*

[2] *Sternberg Astronomical Institute, Universitetskiĭ pr. 13, Moscow, 119992 Russia*

[3] *Space Research Institute, Russian Academy of Sciences, Profsoyuznaya ul. 84/32, Moscow, 117810 Russia*

[4] *Pushchino Radio Astronomy Observatory, Astro Space Center, Lebedev Physical Institute, Russian Academy of Sciences, Pushchino, Moscow oblast, 142290 Russia*

Received March 15, 2003; in final form, May 8, 2003

Abstract—We report the results of monitoring the H_2O maser in NGC 7538, which is associated with a star-forming region. The observations were carried out on the 22-meter telescope of the Pushchino Radio Astronomy Observatory. Two intervals of long-term variability of the integrated flux that reflect the cyclic activity of the maser have been distinguished (1981–1992 and 1993–2003); the data for the earlier activity cycle, 1981–1992, have been analyzed. The period of the long-time-scale variations is about 13–14 years. Flares of individual spectral features and of two groups of features with mean radial velocities of −60 and −46.6 km/s have been observed. The flares lasted from 0.3 to 1 year. The emission features observed during the 1984–1985 flare at radial velocities between −62 and −58 km/s probably form a spatially compact group of spots ($< 10^{15}$ cm) in NGC 7538 IRS1. The triplet structure of the spectra can be traced. The observed anticorrelations and correlations of the fluxes of the triplet components suggest that the maser spots may be located either in a protoplanetary disk or in a high-velocity gaseous outflow.

1. INTRODUCTION

One approach to studying astronomical objects is long-term monitoring aimed at revealing the character of variations of the emission. In this paper, we report the results of long-term monitoring observations of the maser emission of the source NGC 7538 in the 1.35 cm H_2O line.

NGC 7538 is an extended and complex area located in the Perseus Arm of the Galaxy at a distance of 2.8 kpc [1]. It is most conspicuously associated with a visible HII region. The compact cluster of three infrared sources IRS1-3 lies approximately 2′ to the south [2]; in total, 11 infrared sources have been detected in this region [3]. NGC 7538 is also associated with a large molecular-cloud complex that has been mapped in lines of CO [4, 5], H_2CO at 4860 MHz (the 1_{10}–1_{11} transition) [6–8], HCO^+ (the 1–0 transition) [9], CS, and NH_3 [4], as well as in the HI line [10, 11]. The molecular cloud is coincident with an extended HII region. The region is rich in dynamically developing star-forming regions, which are located in the core of the molecular cloud [4] and are closely related to high-velocity gas and ultracompact HII regions. According to CS observations, the cloud core velocity is about −57 km/s [4].

The OH maser emission of NGC 7538 was first detected by Downes [12] and Turner *et al.* [13] in 1970, while the H_2O maser emission was discovered by Johnston *et al.* [14] in 1973. The water-vapor maser called NGC 7538S is located near IRS11. Later, another H_2O maser was detected in this region 1.3′ to the north [15, 16], coincident with an ultracompact HII region [17] and the infrared source IRS1. For convenience, we will call this maser NGC 7538N. It is located nearly at the center of the HCO^+ molecular cloud at a velocity of −59.7 km/s [9]. In the catalog of Comoretto *et al.* [18], the northern and southern H_2O masers have the same identification, S158.

The region associated with IRS1 has a peculiar morphology. Balley and Lada [19] detected a high-velocity outflow, which was studied in detail by Campbell and Thompson [20]. Fisher *et al.* [21] determined the orientation of the high-velocity outflow. The subsequent studies of Scoville *et al.* [5] revealed a rotating disk around IRS1 and, in addition to the CO molecular outflow, a high-velocity outflow of ionized gas at 5 and 15 GHz. The plane of the disk is perpendicular to the bipolar HII region and inclined 55° to the main axis of the outflow.

1063-7729/03/4710-0838$24.00

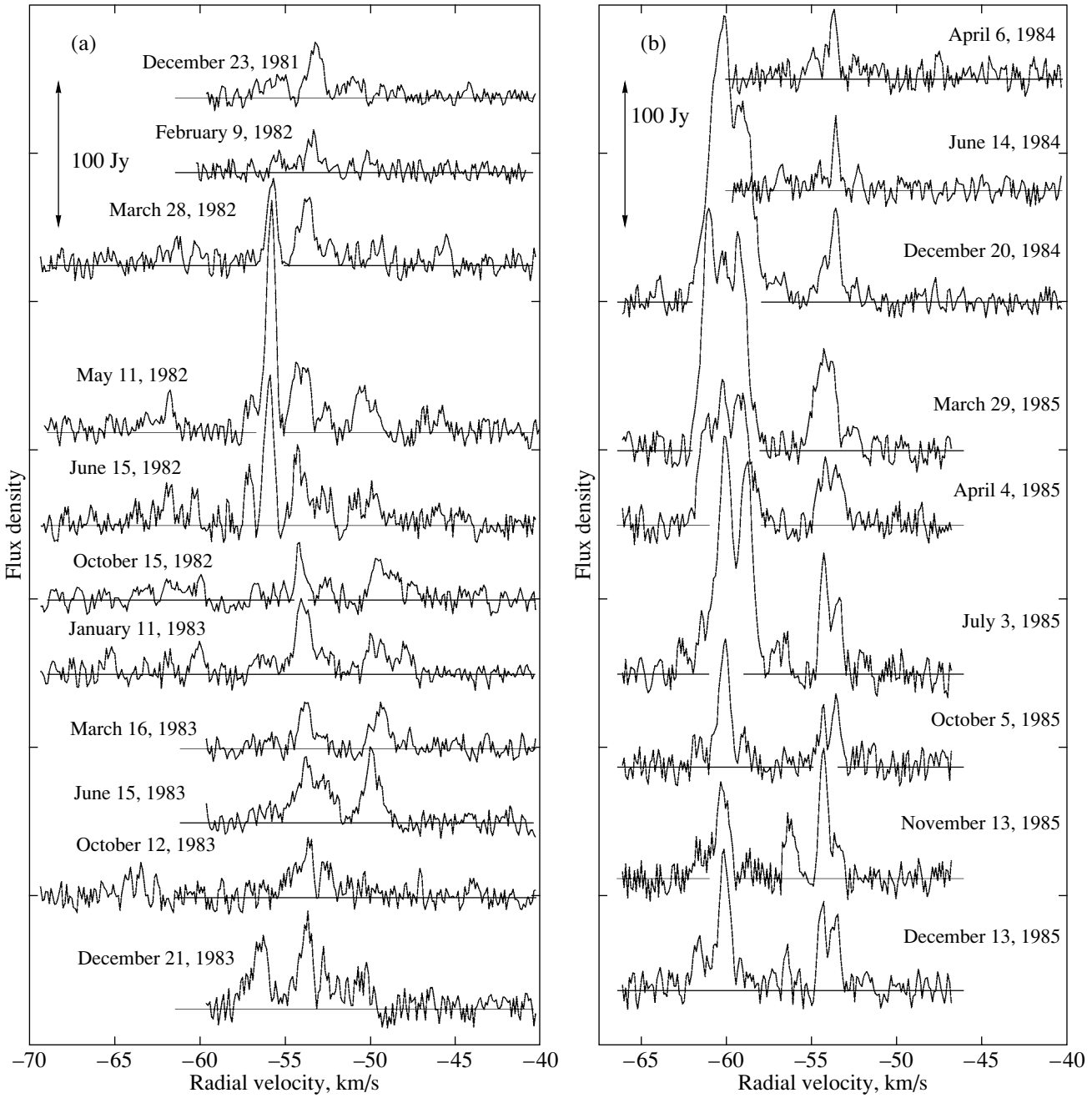

Fig. 1. Spectra of the H_2O maser emission of NGC 7538 obtained in 1981–1992. The vertical arrow shows the flux density scale.

The variability of the water-vapor maser NGC 7538S in November 1974–October 1976 was studied by White and Macdonald [22]. The integrated flux peaked in mid-1975. VLBI observations of the H_2O masers in NGC 7538 were carried out by Kameya *et al.* [23] in May 1987. In NGC 7538N, which is associated with IRS1 and OH [2], H_2CO [6], CH_3OH [24], $^{15}NH_3$ [25], and NH_3 [26] masers, the maser spots form two groups. One group is very compact and is in front of an ultracompact HII region [17], which is the source of excitation of the maser emission. The maser spots of the other group are widely scattered over a $24'' \times 15''$ area. The considerable difference in the distributions of the maser spots in the two groups associated with IRS1 suggests the action of different pumping mechanisms for these groups.

The maser spots in NGC 7538S are located at the same positions as the OH masers [2] and the ultracompact HII region. The spots trace a structure extended toward IRS11 and separated from it by $10''$.

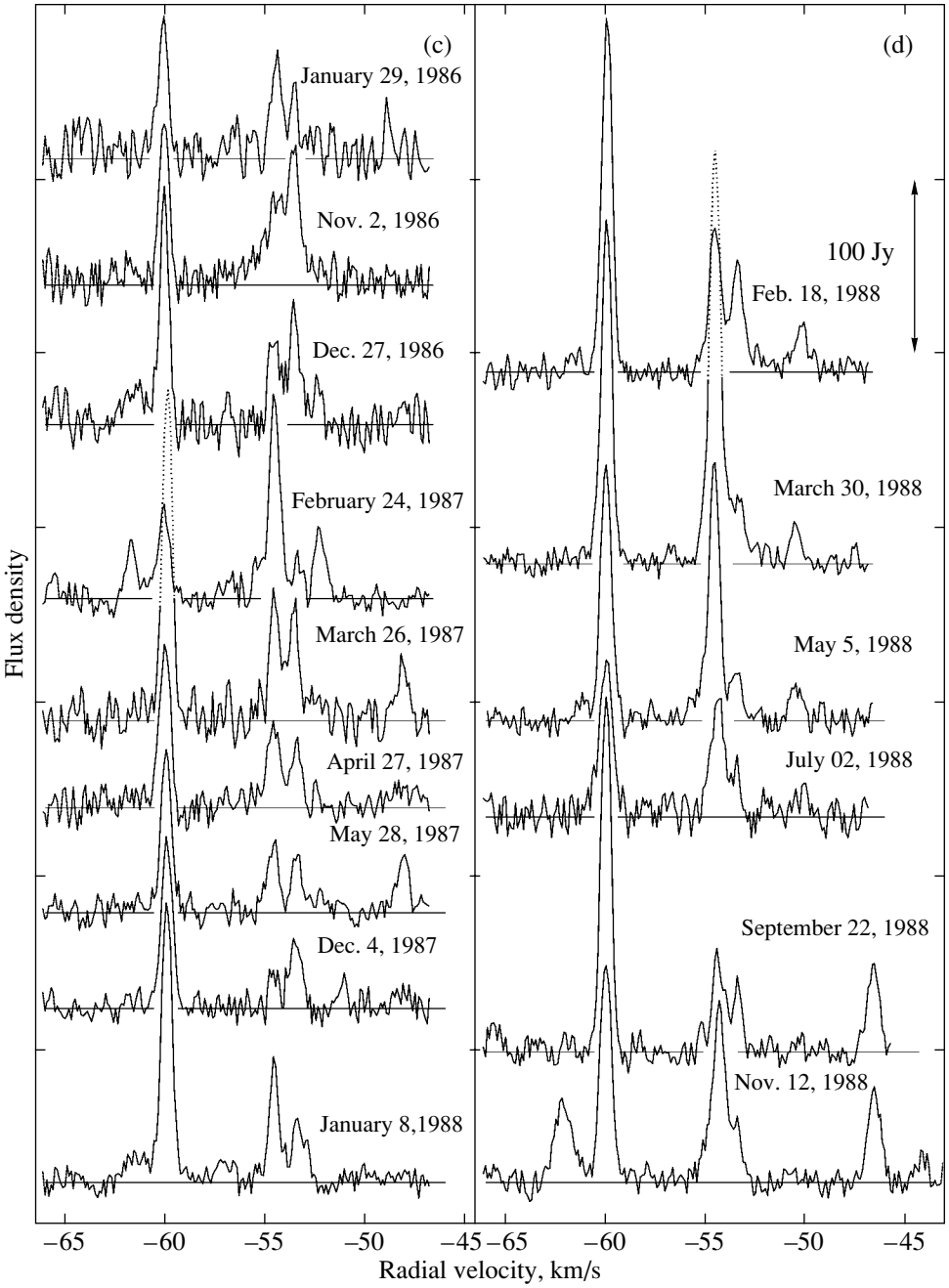

Fig. 1. (Contd.)

This suggests that the HII region, not IRS11, is the main source of the maser spots.

High-resolution observations of IRS1 in the 1.35 cm continuum and the H66α radio recombination line were carried out by Gaume *et al.* [27], who showed that the core of the HII region contains numerous clumps with brightness temperatures of $\approx 1.5 \times 10^4$ K. The continuum core consists of two components, northern and southern, with a region of enhanced electron density between them. The exciting star is presumably at the center of this region. There is an outflow of ionized gas from the core of the HII region toward the north and south.

We report here the results of our monitoring in 1981–1992, when we observed one of the two cycles of activity of the H_2O maser associated with the source IRS1 in the NGC 7538 complex found by us.

2. OBSERVATIONS AND DATA

Observations of the 1.35-cm H_2O maser emission of IRS1 in the NGC 7538 complex ($\alpha_{1950} =$

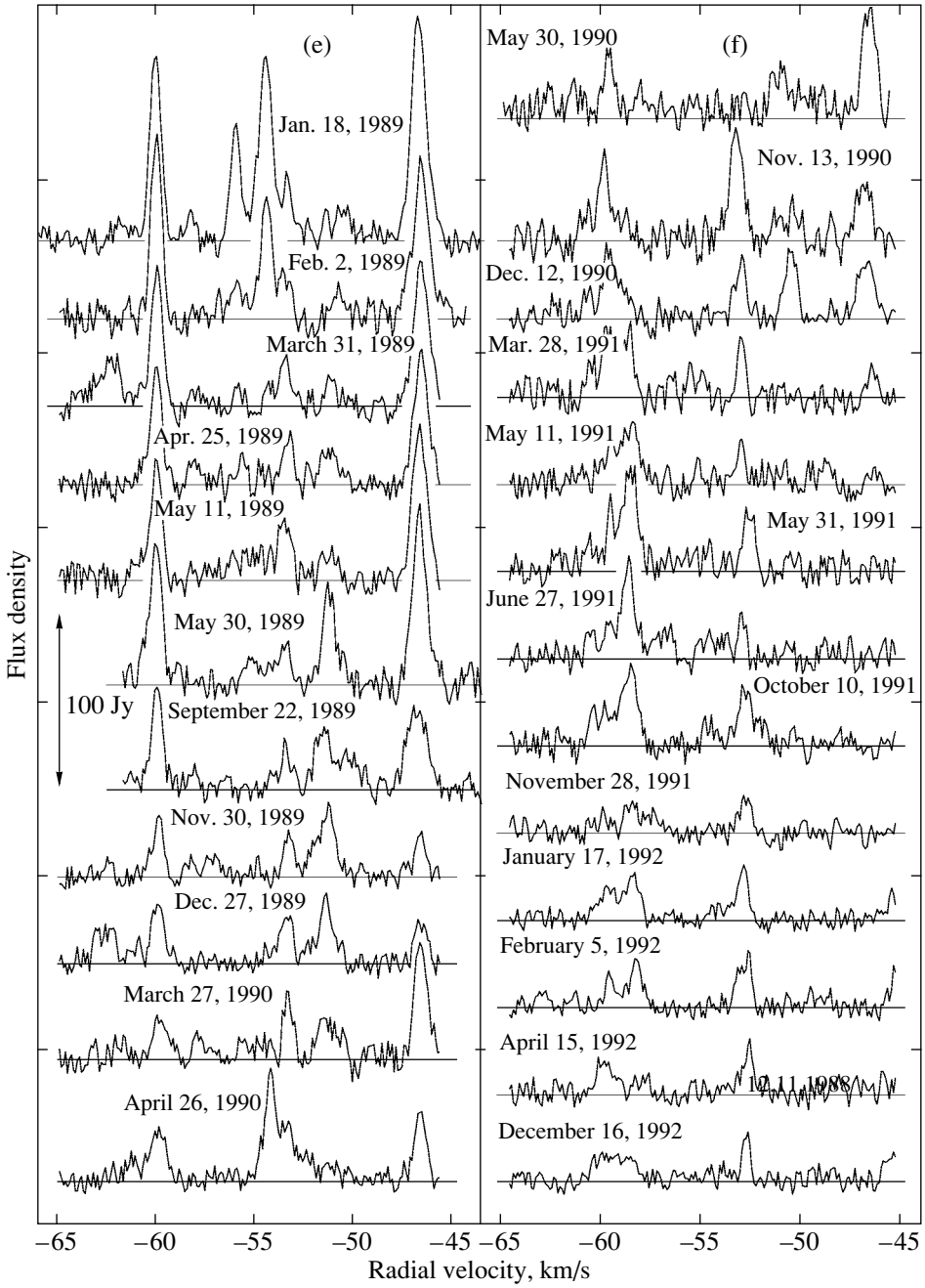

Fig. 1. (Contd.)

$23^h11^m36.5^s$, $\delta_{1950} = 61°11'49''$) were carried out on the fully steerable, parabolic, 22-m radio telescope of the Pushchino Radio Astronomy Observatory. Monitoring observations were obtained in December 1981–January 2003. We present here the results for the data obtained from 1981 to 1992. The mean interval between observations was about 1.5 months. An antenna temperature of 1 K for a pointlike source of unpolarized emission corresponds to a flux density of 25 Jy (see, for example, [28]).

The receiving equipment used in the NGC 7538 monitoring included a liquid-helium-cooled 22-GHz traveling wave maser amplifier. The system noise temperature was 200–300 K. The antenna beamwidth at 22 GHz is 2.6′. We used the symmetric beam modulation technique, with the receiver frontend being switched between two feed horns. As a result, the signal was received alternately from two directions separated by 10′. The symmetric beam switching enabled us to considerably reduce the effect of atmospheric emission. The observations were carried out using the ON–ON method. The antenna was first

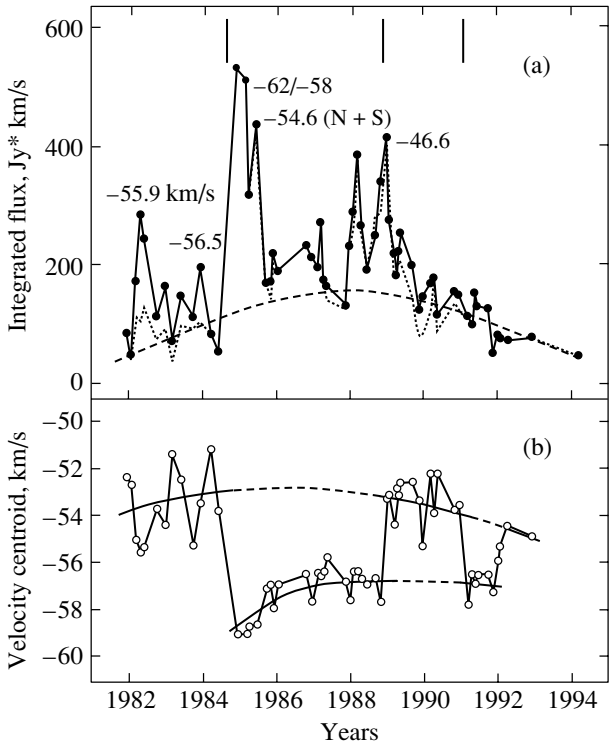

Fig. 2. Variations of (a) the integrated flux of the H_2O maser emission and (b) the velocity centroid. The dashed curve shows variations of the total flux corrected for the contribution of the southern source. The vertical lines show the boundaries of individual time intervals. The numbers indicate the radial velocities of the features during the flares. The feature labeled *S* belongs to the southern source, while the remaining features belong to the northern source.

pointed toward the source using one horn, then using the other. A noise tube was activated for calibration during the first phase of the observations.

The stability required for the frequency of the first local oscillator was provided by a phase-lock-loop frequency control system. The driving oscillator was the Ch6-31 frequency synthesizer, whose frequency was changed by tuning the receiver to the appropriate spectral interval. The signal analysis was carried out by a 96-channel filter-bank spectrometer with a frequency resolution of 7.5 kHz (0.101 km/s in radial velocity in the 1.35-cm line).

The results of monitoring the NGC 7538 H_2O maser in 1981–1992 are presented in Fig. 1. The vertical arrow shows the flux density scale in Janskys. The horizontal axis is the radial velocity with respect to the Local Standard of Rest. For convenience, all spectra are drawn to the same scale in both axes.

Figure 2a shows variations of the integrated flux, calculated as $\Sigma F(V_i)\Delta V$, where $F(V_i)$ is the flux at radial velocity V_i and ΔV is the spectral resolution of the filter-bank spectrometer, 0.101 km/s. In addition, for each spectrum, we calculated the velocity centroid ("weighted-mean" radial velocity) of the maser emission as $\Sigma F(V_i)V_i/\Sigma F(V_i)$ (Fig. 2b). Strong velocity jumps were observed, due to the appearance or disappearance of individual emission features or groups of features. We divided the entire observation period into separate time intervals in accordance with these jumps. The boundaries between these time intervals are marked with vertical lines.

Figure 3 shows a superposition of the spectra for particular time intervals and for the entire period of 1981–1992 (Fig. 3f). In Fig. 3e, we excluded three spectra obtained in 1982 (a flare with a duration shorter than four months) and four spectra obtained from the end of 1984 to the middle of 1985, when the strongest flare during the 1981–1992 monitoring occurred. This revealed the triplet structure of the H_2O maser spectra more clearly.

Figure 4 presents the average spectra for the same time intervals. The average spectrum for the first interval (December 1981–June 1984) consists of two parts, since the spectra were obtained in different radial-velocity intervals (Figs. 1a, 1b). The time variations of the fluxes of the three most intense and long-lived components are shown in Fig. 5. The arrows show times when the fluxes of the components at −60 and −54.6 km/s were anticorrelated. The vertical dashes at the bottom mark the positions of the emission maxima obtained by interpolating curves *1* and *3*.

3. RESULTS OF THE OBSERVATIONS

Our analysis of the monitoring data for NGC 7538 from 1981 to 2002 shows that there were two intervals of variability of the integrated flux of the H_2O maser emission: 1981–1992 and 1993–2003. We observed NGC 7538 episodically during the period of minimum maser activity (1992–1994). Due to the large amount of observational data collected, we present here the results for the first interval of maser-emission variability. In addition, we observed a decline of the maser activity in 2002–2003. Therefore, to obtain a more complete picture of the variability during the second period, it is useful to have observations over another one or two years.

3.1. Variability of the Integrated Flux

As was noted in the Introduction, H_2O maser emission is observed from two sources in the region of NGC 7538, separated by 0.4^s in right ascension and $1'19''$ in declination. When observing NGC 7538N with the $2.6'$ beam of the 22-m telescope, the emission of NGC 7538S was attenuated by a factor of two. Though the southern source is weaker than the

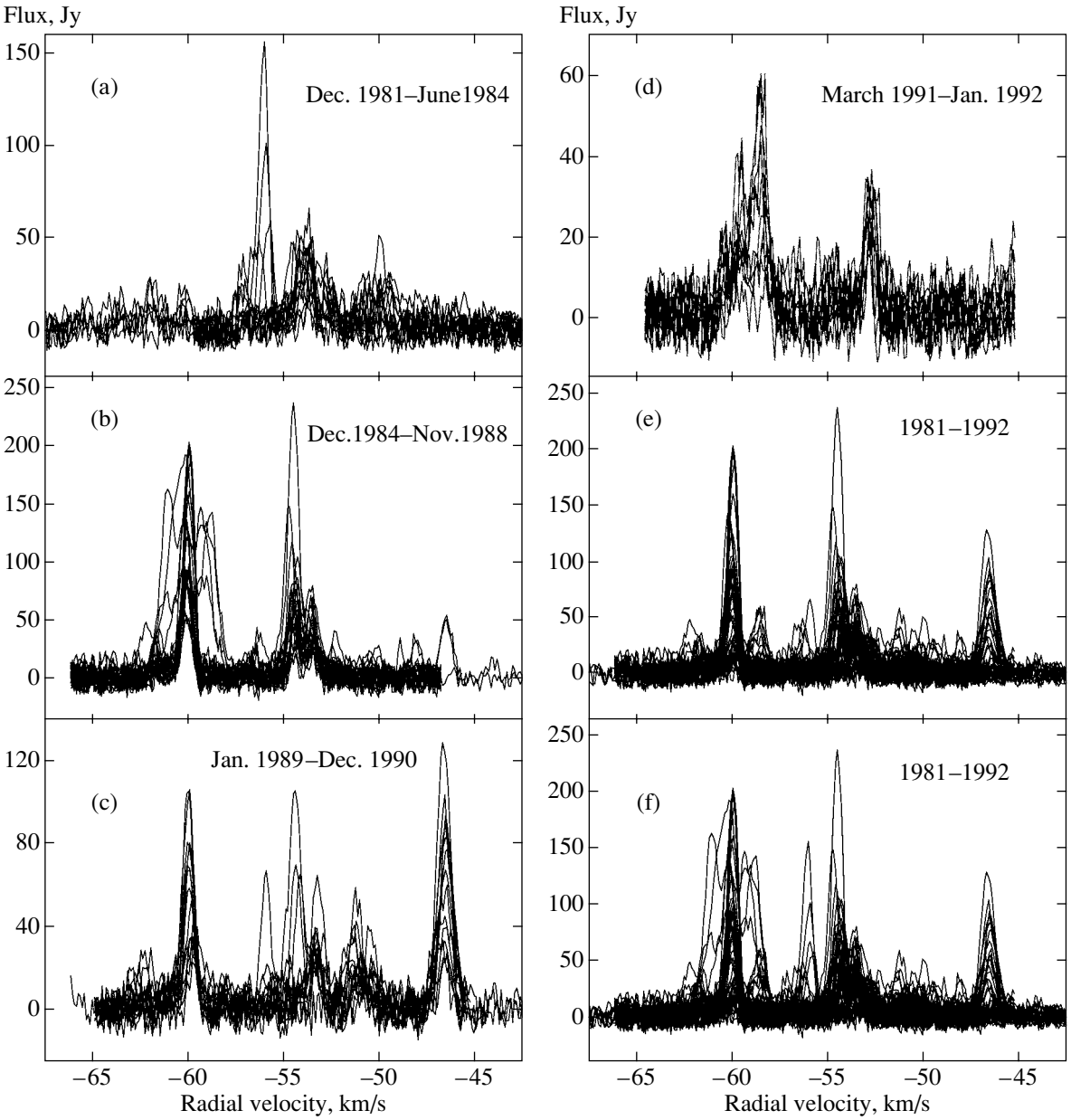

Fig. 3. Superposition of the spectra for individual time intervals (a–d) for the entire interval 1981–1992 (e, f).

northern source, its spectrum includes several emission features, so that its effect on the total-flux variability was sometimes significant. Since the velocities of individual emission features are fairly different and stable, we can correct the observed total flux for the contribution of the emission of NGC 7538S.

For this purpose, we used the data from individual observations of the source from the catalog of Comoretto *et al.* [18] and from Kameya *et al.* [23]. The correction we have applied does not guarantee full elimination of the effect of the southern source, but does considerably reduce its contribution to the total flux. The character of the corrected flux variations (dashed curve in Fig. 2a) is close to the flux variations observed for the northern source.

For a more correct separation of the emission into two components (NGC 7538N and NGC 7538S), it is desirable to have spectra obtained simultaneously from both sources. This will make it possible to correctly attribute observed emission features to the appropriate source. We have been obtaining such observations of NGC 7538 on the 22-m telescope since January 2003.

The integrated flux variations contain two components: fast and slow (dashed curve in Fig. 2a). The fast component displays a pronounced flaring char-

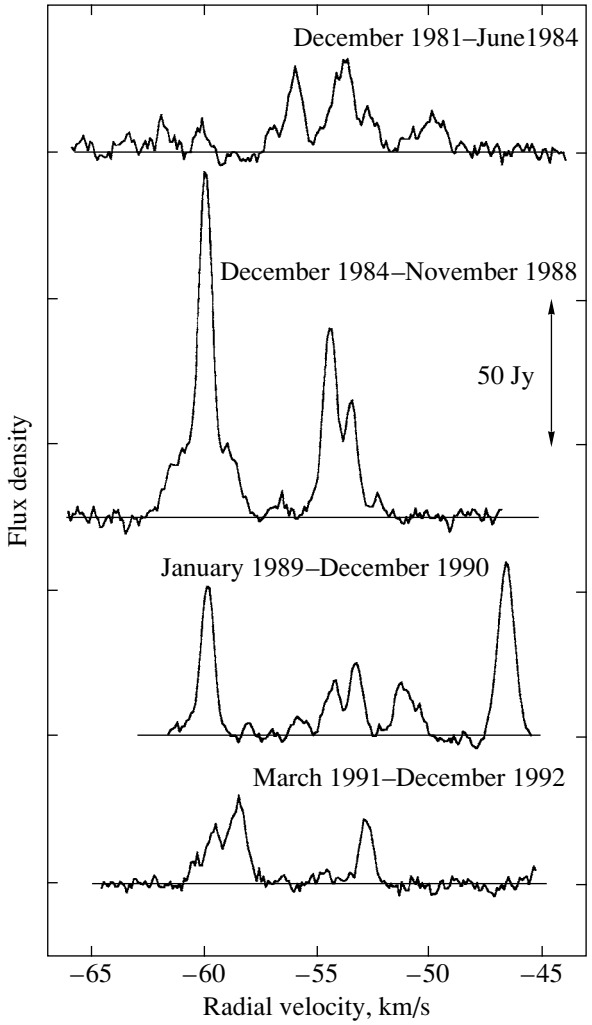

Fig. 4. Average maser spectra for the same intervals as in Fig. 3.

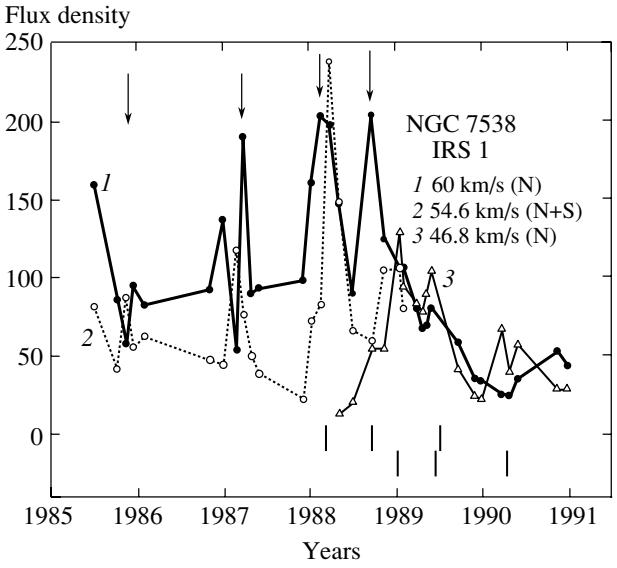

Fig. 5. Flux variations of three H_2O emission features. The vertical arrows mark times when the fluxes were anticorrelated. The vertical lines at the bottom mark positions of the emission maxima obtained by interpolating curves *1* and *3*.

acter and was especially prominent from the middle of 1984 to end of 1985 and in 1988–1990.

The slowly varying component displayed two minima: one in approximately 1980–1981 and the other in 1993–1994. The existence of the second minimum is confirmed by one of the points obtained in 1994. The time interval between the minima is about 13–14 years. This value can be adopted as the period of long-time-scale variations of the maser activity. There was an activity maximum in 1988. This kind of maser-emission variability characterizes the state of the H_2O maser activity as a whole and may be associated with cyclic variability of the young exciting star at an early stage of its evolution, when the star formation process has a nonstationary character.

3.2. Flare Activity and the Velocity Centroid

We observed four flares with durations from 0.3 to 1 year from 1982 to 1992. The variations of the integrated flux and velocity centroid were correlated. Strong flares of the flux were accompanied by velocity jumps. This is well traced in 1984 and 1988. During the 1991 velocity jump, we observed a decline of the total flux during a low level of the maser activity. Analysis of the available individual spectra of the northern (associated with IRS1) and southern (associated with IRS11) sources shows that all the velocity jumps were due to variability of the emission of the northern source.

In 1982–1984, we observed fast variations of the velocity centroid in the interval from −51 to −55.5 km/s with a period of about one year. These variations were associated with two flares, at −55.9 and −56.5 km/s. The first substantial velocity jump took place in 1984 and was due to a strong flare of the group of features with radial velocities from −62 to −58 km/s. The next jump took place at the beginning of 1989 and was also connected with the appearance of a group of spectrally closely spaced features with a mean radial velocity of about −46.6 km/s. The disappearance of the emission of this group at the beginning of 1992 resulted in a new velocity jump. The last velocity jump was also observed at the beginning of 1992 and was due to the appearance of an emission feature at $V_{LSR} = -45.5$ km/s. A tendency for the amplitudes of the velocity jumps to decrease can be traced (fitted solid and dashed curves in Fig. 2b).

We observed flares of the emission of two groups of features: one at velocities of −62 to −58 km/s and

the other at velocities of −47.5 to −45 km/s. During the flare we observed starting at the end of 1984, four features appeared at radial velocities of −61.2, −60.3, −59.5, and −58.7 km/s. The most intense emission was observed by Forster *et al.* [29] from November 1975 to March 1976 at $V_{LSR} = -61.2$ km/s, one arcsecond from the ultracompact HII region. The observations of Kameya *et al.* [23] (May 1987) show that the component with the strongest emission ($V_{LSR} = -60.3$ km/s) is located at the boundary of the ultracompact HII region. Kameya *et al.* [23] did not detect the component at −61.3 km/s and suggested this was due to variability of the maser emission. Apart from 1985, we observed emission at −61.3 km/s throughout our monitoring interval, although this emission appeared only episodically.

During the 1984–1985 flare, four features appeared not simultaneously, but with some delay. Due to a large gap in the 1984 observations, we cannot accurately estimate the maximum delay between the appearances of the first and last feature, but the delay is probably in the range 6–10 months. The estimated velocity of the stellar wind from the central star in IRS1 is a few hundreds of km/s; we will adopt the value ∼500 km/s [27]. In this case, the four emission features with similar radial velocities should form a spatially compact group $< 10^{15}$ cm in size, considerably smaller than the sizes of a compact group of spots estimated from the VLBI data of Kameya *et al.* [23] (3×10^{16} cm) and Migenes *et al.* [30] (2×10^{16} cm).

3.3. Correlation and Anticorrelation of the Emission Fluxes

A clear anticorrelation of the fluxes of two components (−60 and −54.6 km/s) can be traced in Fig. 5. We observed four such cases, ruling out the possibility that the anticorrelations came about by chance. However, according to Kameya *et al.* [23] (observations of May 9, 1987), the component at −54.6 km/s (−54.9 km/s in [23]) is identified with NGC 7538S. Kameya *et al.* [23] also detected emission at this velocity in NGC 7538S, but it was a considerably fainter (3.1 Jy). Therefore, we cannot rule out the possibility that the emission anticorrelated with the −60-km/s feature is associated with the northern source, while the emission we have recorded is the sum of the contributions of features from the two sources, with the emission of NGC 7538S being attenuated by a factor of two by our antenna beam.

This is confirmed by the H_2O spectrum of IRS1 from the catalog of Comoretto *et al.* [18] obtained on October 13, 1988. The flux of the −54.5-km/s component is 35 Jy, as opposed to 3.1 Jy for the −54.9-km/s component of Kameya *et al.* [23].

The flux variations of the feature at −46.8 km/s are essentially correlated with the flux of the main feature, though with a time delay. This is clearly traced for three maxima (flares of emission). The intervals between observations are unequal and sometimes fairly long; therefore, we have interpolated curves *1* and *3* to find the positions of the maxima. The differences in the positions of the three successive maxima of curves *1* and *2* are 10.1, 8.9, and 9.2 months. The average delay is 9.4 months. Similar delays for the three successive flares could come about if there is a single source of excitation of the maser spots. A young star in the ultracompact HII region near IRS1 is the most likely such source. For a stellar-wind velocity of ∼500 km/s [27], a delay of 9.4 months corresponds to a distance of $\sim 1.2 \times 10^{15}$ cm. The small differences in the delays for the three flares could be due to differences in the stellar-wind velocities in the intervals corresponding to the individual flares.

Thus, the flux anticorrelations and correlations we have found suggest that there is a common source of excitation for the components at −60, −54.5, and −46.8 km/s, with these components being located at different distances from the exciting star.

3.4. A Model for the H_2O Maser NGC 7538 IRS1

The superposition of all the spectra for our monitoring of NGC 7538 from 1981 to 1992 shows that the emission features are concentrated primarily in three groups (Figs. 3 and 4). The central group has the largest velocity dispersion. This velocity interval includes the strongest emission from NGC 7538S, which can appear from time to time in the spectra obtained by us for NGC 7538N. This is probably why the central group contains a large number of emission features.

Thus, we have observed three characteristic behaviors: the triplet pattern of the spectra, an anticorrelation between the fluxes of components of the central and lateral groups, and a correlation between the fluxes of the lateral components with a delay of about 9.4 months for three successive flares of the maser emission. The first two properties could come about in a protoplanetary (Keplerian) disk (see, e.g., [31, 32]).

The correlation between the fluxes of the lateral components suggests that the maser spot responsible for the emission at −46.5 km/s is associated with the same excitation source. This implies that all three components are associated with the protoplanetary disk. A natural question then arises: why do we not observe an anticorrelation between the fluxes of the

component at −46.5 km/s and the other components? A necessary condition for the supposed anticorrelation of the emission intensities is the absence of motion of the H_2O molecules of one maser spot relative to the other. It is possible that this condition is not fulfilled and that the −46.5-km/s spot participates in some motion with respect to the exciting central star. For example, the spot could be located in an outflow of the ionized gas observed in the ultracompact HII region near IRS1 [27]. Since we have not detected any drift of the emission at −46.5 km/s, the direction of the gas outflow would have to be close to the plane of the sky.

4. CONCLUSIONS

Let us summarize the most important results of our monitoring of NGC 7538 carried out on the 22-m radio telescope of the Pushchino Radio Astronomy Observatory.

(1) We have presented a catalog of H_2O maser spectra for NGC 7538 IRS1 for 1981–1992.

(2) We have detected two types of integrated flux variations, on long and short time scales. The period of the slow component is about 13–14 years; it is probably associated with quasi periodic activity of the star in the ultracompact HII region at an early stage of its evolution.

(3) The short-time-scale variability had a flaring character, with durations from several months to one year. These variations were associated with a strong increase of the emission of one of the groups of emission features with similar radial velocities. These emission features may form spatially compact groups ($< 10^{15}$ cm).

(4) There were abrupt changes of the velocity centroid associated with the flaring component of the activity of NGC 7538 IRS1.

(5) The detected anticorrelation of the fluxes of two emission features at radial velocities of −60 and −54.5 km/s and correlation of the fluxes at −60 and −46.5 km/s (with a mean time delay of about 9.4 months for three successive flares) suggest that there is a single source of excitation of the maser spots—a central star in the ultracompact HII region near IRS1. The absence of an anticorrelation between the fluxes of the component at $V_{LSR} = -46.5$ km/s and the central or other lateral components suggests that the spot at $V_{LSR} = -46.5$ km/s is located in a high-velocity gas outflow from the central star.

The proposed simple model is based on observations made during the first interval of activity of the H_2O maser in NGC 7538 (1981–1993); the model will be refined after our analysis of data for the second period of activity (1994–2003).

ACKNOWLEDGMENTS

The RT-22 radio telescope is supported by the Ministry of Science and Technology of the Russian Federation (registration number 01-10). The authors are grateful to the staff of the Pushchino Radio Astronomy Observatory for their substantial help with the observations.

REFERENCES

1. D. Campton, Y. M. Georgelin, and Y. P. Georgelin, Astron. Astrophys. **66**, 1 (1978).
2. C. G. Wynn-Williams, E. E. Beklin, and G. Neugebauer, Astrophys. J. **187**, 473 (1974).
3. M. W. Werner, E. E. Beklin, I. Gatley, *et al.*, Mon. Not. R. Astron. Soc. **188**, 463 (1979).
4. P. T. P. Ho, R. N. Martin, and A. H. Barrett, Astrophys. J. **246**, 761 (1981).
5. N. Z. Scoville, A. I. Sargent, D. V. Sanders, *et al.*, Astrophys. J. **303**, 416 (1986).
6. D. Downes and T. L. Wilson, Astrophys. J. **191**, L77 (1974).
7. Y. K. Minn and J. M. Greenberg, Astrophys. J. **196**, 161 (1975).
8. A. H. Rots, H. R. Dickel, A. H. Foster, and W. M. Goss, Astrophys. J. **245**, L15 (1981).
9. W. Batrla, P. Pratar, and L. E. Snyder, Astrophys. J. **330**, L67 (1988).
10. P. L. Read, Mon. Not. R. Astron. Soc. **192**, 11 (1980).
11. P. L. Read, Mon. Not. R. Astron. Soc. **193**, 487 (1980).
12. D. Downes, Astrophys. Lett. **5**, 53 (1970).
13. B. E. Turner, D. Buhl, E. B. Churchwell, *et al.*, Astron. Astrophys. **4**, 165 (1970).
14. K. J. Johnston, R. M. Sloanaker, and J. M. Bologna, Astrophys. J. **182**, 67 (1973).
15. R. Genzel and D. Downes, Nature **262**, 564 (1976).
16. R. Genzel and D. Downes, Astron. Astrophys., Suppl. Ser. **30**, 145 (1977).
17. B. Campbell and S. E. Persson, Astron. J. **95**, 1185 (1988).
18. G. Comoretto, F. Palagi, R. Cesaroni, *et al.*, Astron. Astrophys., Suppl. Ser. **84**, 179 (1990).
19. J. Bally and C. J. Lada, Astrophys. J. **265**, 824 (1983).
20. B. Campbell and R. I. Thompson, Astrophys. J. **279**, 650 (1984).
21. J. Fisher, D. B. Sanders, M. Simon, and P. M. Colomon, Astrophys. J. **293**, 508 (1985).
22. G. J. White and G. H. Macdonald, Mon. Not. R. Astron. Soc. **188**, 745 (1979).

23. O. Kameya, K. I. Morita, R. Kawabe, and M. Ishiguro, Astrophys. J. **355**, 562 (1990).

24. T. L. Wilson, C. M. Walmsley, L. E. Snyder, and P. R. Jewell, Astron. Astrophys. **134**, L7 (1984).

25. K. J. Johnston, S. R. Stolovy, T. L. Wilson, *et al.*, Astrophys. J. **343**, L41 (1989).

26. S. C. Madden, W. M. Irvine, H. E. Matthews, *et al.*, Astrophys. J. **334**, L107 (1988).

27. R. A. Gaume, W. M. Goss, H. R. Dickel, *et al.*, Astrophys. J. **438**, 776 (1995).

28. E. E. Lekht, M. I. Pashchenko, G. M. Rudnitskiĭ, and R. L. Sorochenko, Astron. Zh. **59**, 276 (1982) [Sov. Astron. **26**, 168 (1982)].

29. J. R. Forster, W. G. Welch, M. C. H. Wright, and A. Braury, Astrophys. J. **221**, 137 (1978).

30. V. Migenes, S. Horiuchi, V. I. Slysh, *et al.*, Astrophys. J., Suppl. Ser. **123**, 487 (1999).

31. R. Cesaroni, Astron. Astrophys. **233**, 513 (1990).

32. E. E. Lekht, S. F. Likhachev, R. L. Sorochenko, and V. S. Strel'nitskiĭ, Astron. Zh. **70**, 731 (1993) [Astron. Rep. **37**, 367 (1993)].

Translated by G. Rudnitskiĭ

Astronomy Reports, Vol. 47, No. 10, 2003, pp. 848–864. Translated from Astronomicheskiĭ Zhurnal, Vol. 80, No. 10, 2003, pp. 919–936.

Interpretation of Orbital Light Curves of U Geminorum

T. S. Khruzina[1], A. M. Cherepashchuk[1], D. V. Bisikalo[2], A. A. Boyarchuk[2], and O. A. Kuznetsov[2, 3]

[1] *Sternberg Astronomical Institute, Universitetskiĭ pr. 13, Moscow, 119899 Russia*

[2] *Institute of Astronomy, Russian Academy of Sciences, ul. Pyatnitskaya 48, Moscow, 109017 Russia*

[3] *Keldysh Institute of Applied Mathematics, Russian Academy of Sciences, Miusskaya pl. 4, Moscow, 125047 Russia*

Received March 5, 2003; in final form, May 8, 2003

Abstract—We interpret optical and IR orbital light curves of the dwarf nova U Gem in its quiescent state in the framework of "hot line" and "hot spot" models. The hot-line model provides an adequate fit to the light curves, while the hot-spot model is not fully consistent with the observations. The minimum χ^2 residuals for the hot-spot and hot-line models are 2203 and 168, respectively. © *2003 MAIK "Nauka/Interperiodica"*.

1. INTRODUCTION

The vast majority of light curves of normal cataclysmic (U Gem type) variables display a so-called "orbital hump" around orbital phase $\varphi \sim 0.8$. Gorbatskiĭ [1] and Smak [2] suggested that this is due to a hot spot at the edge of the accretion disk, where the disk collides with the stream from L1. For many years, the hot-spot model has been widely used to interpret light curves of cataclysmic binaries (see, for example, [3]).

Three-dimensional gas-dynamical studies of the mass transfer in close binaries [4–9] show that, morphologically, the stream and accretion disk are a single formation, and their interaction is shockless. Naturally, in this case, the temperature at the point of contact between the stream and disk does not increase, so that the hypothesis that there is a hot spot on the accretion disk must be abandoned. In the steady-state case, a shock interaction resulting in a temperature increase occurs when the matter flowing around the accretor but not yet captured by the disk collides with the stream from L1. This interaction forms an extended shock wave oriented along the stream [4–6, 10] (the "hot line"), whose radiation makes it possible to understand certain observed features in the light curves of cataclysmic variables [11, 12], in particular, the occurrence of regular and irregular peaks. Comparisons between hot-spot and hot-line models for cataclysmic variables with double eclipses [11, 12] have presented conclusive evidence in favor of the latter type of model for the interpretation of their light curves.

2. FORMULATION OF THE PROBLEM

Eclipsing close binaries are not a homogeneous group of stars. For example, the number of known cataclysmic binaries with double eclipses does not exceed ten. Therefore, it is of interest to consider close binaries with other peculiarities in their light curves and analyze the applicability of various gas-dynamical models for their interpretation. Here, we will analyze light curves of U Gem, which is a prototype cataclysmic binary.

U Gem is an eclipsing system, however, the object that is eclipsed is part of the accretion disk around the white dwarf and the shock emission region, rather than the white dwarf itself. In such systems, the dominant contribution to the optical radiation is made not by the stellar components but by the accretion disks and gas formations originating in the system due to the matter outflow from the donor. When the eclipse curve of U Gem is described using hot-spot models, serious difficulties arise in fitting the shape and position of the eclipse of the hot spot. In particular, the model completely fails to describe the curve at orbital phases $\varphi \sim 0.4$–0.6, i.e., at phases where the model predicts the second eclipse of the spot on the outer edge of the disk by the body of the disk. In fact, no trace of the second eclipse is observed. In the hot-line model, this problem does not arise, since the extended shock wave (i.e., the region where the matter flowing around the accretor and the gas stream from L_1 collide) is located beyond the disk and may also be elevated above the disk edge.

The shape of the intercomponent gas envelope of the system is rather complex, and taking its radiation into account is a very difficult problem. To first

1063-7729/03/4710-0848$24.00

approximation, we assume that the contribution of the intercomponent envelope is small due to the low gas density, and can be neglected. We also neglect the contribution of the stream from L_1 to the total optical radiation, due to the low temperature of the gas in the stream. Only the radiation from the system components, accretion disk, and shock region was taken into consideration in the computations for the hot-line model.

Each component of the model is described by its temperature and size; the temperature can vary over the surface of the source of radiation. There are nominally 18 free parameters in our hot-line model. The parameters of the binary are (1) the component mass ratio $q = M_1/M_2$, (2) the orbital inclination i, (3) the effective temperature of the red dwarf T_{eff}, and (4), (5) the radius R_1 and temperature T_1 of the white dwarf. The parameters of the elliptical accretion disk are (6) the eccentricity e, (7) the semimajor axis of the accretion disk a, (8) an internal parameter of the code A_p, which specifies the thickness of the outer edge of the disk along with the disk radius, (9) the disk temperature in the boundary layer (at the innermost orbit) T_b, (10) a parameter describing the radial temperature distribution of the disk α_g, and (11) the angle of the rotation of the disk periastron relative to the line connecting the system components α_e. The parameters of the hot line are (12)–(14) the semiaxes a_v, b_v, c_v, which specify the shape and size of the ellipsoid describing the hot line, (15), (16) the maximum temperatures of the hot line on the "windward" side (the side of the approaching stream of matter) and the "leeward" side (the side opposite the approaching stream) $T^{(1)}_{\max}$ and $T^{(2)}_{\max}$, (17) a parameter $y_{\min}$ describing the width of the shock, and (18) the difference dy between the points with the maximum temperatures on the windward and leeward sides of the line, originating due to the motion of the matter in the gas stream between the components. A more detailed description of the model and its parameters has been presented in [13, 14].

There are 12 free parameters in the hot-spot model. These are q, i, T_{eff}, R_1, T_1, r_d (the disk radius), α_g, A_p, T_b, and three parameters describing the size and position of the hot spot at the outer edge of the disk: the spot's radius R_{sp}, its azimuth α_{sp}, and the temperature at the center of the spot T_{sp}. A detailed description of the model and its parameters is given in [15].

Since the number of variables in both models is large, we must select the most probable solutions from a number of reasonable sets of parameters derived from the light curves, using estimates for the mass ratio of the close-binary components based on spectral observations, the orbital inclination, and the contribution of the red dwarf to the total radiation of the system.

Another restriction on the solutions is imposed by the method we used when a series of homogeneous light curves of a close binary was considered [16]. First, one of the light curves (called the reference curve) is selected, then a point on this curve (usually near orbital phase $\varphi \sim 0.25$) is selected as a reference point. Further, all remaining fluxes for both the reference curve and the other light curves are tied to the stellar magnitude of this point. In other words, all the homogeneous light curves are reduced to the same energy unit: the observed flux at the first quadrature of the reference light curve. Accordingly, when constructing the nth trial theoretical light curve in magnitudes, the flux at the first quadrature of the theoretical curve that provides the best fit to the observed reference light curve is used to translate the theoretical fluxes calculated in the model into magnitudes. This approach makes it possible to estimate variations of the system's luminosity from one light curve to another at each phase. When comparing the observed and synthesized curves, it also enables us to use both the shape of the light curve (as in the analysis of single light curves) and variations of the average flux level, which imposes supplementary constraints on the domain of allowed system parameters.

As in our previous studies, we used the Nelder–Mead method [17] to search for the parameters providing the best fit to the mean light curves. To find the global minimum of the residual, we used about one hundred different initial approximations for each curve, since a number of local minima usually exist in the parameter domain considered when a large number of independent variables are fit. The consistency between the theoretical and observed light curves for a given model was estimated using the residual

$$\chi^2 = \sum_{j=1}^{n} \frac{(m_j^{\text{theor}} - m_j^{\text{obs}})^2}{\sigma_j^2},$$

where m_j^{theor} and m_j^{obs} are the theoretical and observed magnitudes at the jth orbital phase, σ_j^2 is the dispersion of the observations for the jth point, and n is the number of normal points in the curve.

When constructing a theoretical light curve, we calculated the flux from the system components $F(\mathbf{X}, \varphi)$ for a series of orbital phases φ for the specified set of parameters $\mathbf{X}$. The resulting $F(\mathbf{X}, \varphi)$ are given in arbitrary units. They are translated into commonly used physical units (per unit wavelength) via the expression $f = Fa_0^2 \times 10^{12}$ [erg s^{-1} cm^{-3}], where a_0 is the distance between the centers of mass of the stars in centimeters. When interpreting individual light curves during the construction of a

trial theoretical curve, the calculated fluxes are usually translated into magnitudes using the flux at the first quadrature for the given trial curve. To compare the synthesized and observed curves, the calculated trial light curve is shifted so that the observed and calculated fluxes in magnitudes at the first quadrature agree. The χ^2 criterion is used in the subsequent comparison of the observed and synthesized light curves.

Spectral observations (the overall appearance of the spectrum and variations of the radial velocities) can be used to determine some parameters of a binary, i.e., to impose additional constraints and restrict the number of varied parameters. Such parameters include $q = M_1/M_2$, the effective temperatures of the stars T_1 and T_2, the radius of the primary R_1, and the orbital inclination i. Having fixed these parameters of the system, we can use the light curves to estimate the parameters of the accretion disk (its eccentricity e, semimajor axis a, the azimuth of periastron α_e, and the temperature of the boundary layer T_b) and of the region of shock interaction (the semiaxes of the truncated ellipsoid describing the shape of the hot line a_v, b_v, and c_v; the maximum temperatures of the hot line on the windward and leeward sides $T_{\max}^{(1)}$ and $T_{\max}^{(2)}$; the compactness of the region of shock deexcitation, specified by the parameter $y_{\min}$; and the parameter dy—the distance along the y axis of the hot line between the points with maximum temperature).

We obtained solutions for two gas-dynamical models with different locations of the shock-interaction region: (a) a hot line located along the stream from L_1 and (b) a hot spot at the edge of the accretion disk. A comparison of the results makes it possible to distinguish between these two gas-dynamical models.

3. GENERAL INFORMATION ABOUT U Gem

Dwarf novae are particularly interesting due to the complex patterns shown by their variability. They show brightness variations on a wide range of timescales. Normal dwarf novae, or U Gem-type variables, display flares by up to 4–6^m, which occur quasiperiodically on time intervals of 10–300 days. All well-studied dwarf novae are short-period binaries with orbital periods of several hours. Many display regular brightness oscillations with amplitudes of about 0.5^m, which are correlated with the orbital period. Dwarf novae are frequently found to be soft X-ray sources.

The most complete study of U Gem has been carried out by Krzeminski [18], who constructed a model for the system and determined its parameters based on his photometric observations and the spectral observations of Kraft [19]. Extensive photometric observations were also made by Mumford [20] (during a flare) and Paczynski [21]. Both Krzeminski and Paczynski monitored several flares of the system. These observations had a typical time resolution of 0.5–2 minutes. Two white-light light curves with a substantially higher time-resolution (a signal integration time of about 2 s) were obtained by Warner and Nather [22], who were studying "flickering" of the brightness. In the quiescent state of the system, the light curve displays an eclipse of the hot source and a "hump" at orbital phases 0.7–0.8.

The first spectral study of U Gem [19] indicated the presence of hydrogen and Ca II emission lines in the optical spectrum. The He I 4471 and 4026 Å lines are rather weak, and the He II 4686 Å line is also sometimes observed. The lines display two-peaked profiles, with the distance between the peaks corresponding to the rotational velocity of the disk ring, $v \sin i = 580$ km/s. Kraft [19] used the radial-velocity curve to derive the value $K_1 = 265$ km/s for the hot component, and demonstrated that the blue star is eclipsed. Only one optical spectral type can be observed (sdBe), and the absorption lines of the secondary are not visible, making it impossible to determine the component mass ratio directly from optical spectral data.

The spectral type of the secondary (dM4.5, with a possible error of 0.5 spectral type) was first determined by Stauffer *et al.* [23] based on their IR spectral studies. This result was confirmed by Wade [24], who showed that the spectral energy distribution (SED) of U Gem can be interpreted as the combined spectrum of an M4.5 or M5 star and a source with a flat continuum. Infrared photometry of U Gem was carried out by Frank *et al.* [25], Berriman *et al.* [26], and Panek [27], who derived a high-accuracy H light curve. The distance to the system estimated from absolute photometry and the IR color indices is 76^{+36}_{-24} pc [24, 25, 27].

In the quiescent state, the UV spectrum of U Gem displays roughly the same average continuum, without any apparent phase dependence [28]. The UV flux may be due to nuclear burning on the white-dwarf surface near the boundary layer of the disk [28]. Subsequent studies at near-UV wavelengths have indicated that the contribution of the white dwarf to the total flux of the system is substantial. The SED at these wavelengths in the quiescent state corresponds to that of a main-sequence star with a temperature of 26 000–30 000 K [29, 30]. If we assume that this flux comes from the white dwarf, its absolute magnitude is $10^m.7$, which is normal for a white dwarf. The observed temperature of the white dwarf is higher before a flare or immediately after a decrease in the optical flux: ~35 000–38 000 K [31, 32]. In the two-component

model of [32, 33], the best fit to the observed UV spectrum is provided when the temperature of the white dwarf is 29 100–31 400 K and the temperature of the boundary layer is 54 000–58 000 K; the residual is substantially lower than in a one-component model in this case. The source of the hot radiation component occupies ~15–18% of the visible surface of the white dwarf. For the given temperature, the contribution of the white dwarf to the total optical radiation reaches ~18%. In the quiescent state of the system, neither soft nor hard X-ray radiation is observed [34, 35]. The flare activity of U Gem has been studied in detail by Krzeminski [18] and Smak [36]. During flares, U Gem displays appreciably variable 0.15–0.5 keV X-ray radiation [34] and a weaker 2–10 keV flux [35].

Thus, spectral studies of U Gem indicate that the optical radiation comes primarily from the area of interaction between the outflowing matter and the disk and, to a lesser extent, from the disk itself. The radiation from the stellar components of the close binary can only be observed in the UV (the white dwarf) and the IR (the red dwarf).

The most prominent feature in the optical light curve of U Gem in its quiescent state is a large, broad hump with an amplitude of up to $0^m.5$ that extends over up to half the orbital period at phases 0.6–0.1. An eclipse with a duration of $\sim 0.05 P_{orb}$ is observed against the background of this feature. The hump is roughly symmetrical about its maximum, which occurs at phase 0.85; i.e., the shape of the ascending branch of the curve is a mirror reflection of the descending branch (on which the eclipse is superimposed). The eclipse, which appears to be total, displays a flat, extended bottom; the ingress lasts about 100 s, while the egress lasts about 50 s, indicating that the eclipsed region is fairly large. No secondary eclipse has been detected. The eclipses differ in their widths, depths (up to $0^m.1$), and orbital phases, suggesting that the disk is eclipsed rather than the star. During an eclipse, the residual radiation is specified primarily by emission lines from the noneclipsed part of the disk. The contributions of both the M star and the white dwarf are small.

The instability of the position of the center of the eclipse makes it difficult to calculate the system ephemeris. Krzeminski [18] and Warner and Nather [22] calculated their light curves using the same ephemeris [18], in spite of the almost ten-year difference between the epochs of their observations. Careful studies of the times of minima in the quiescent state of the system [37] indicate that the orbital period varies quasiperiodically; on average, Min.I = HJD2437638.82625 + 0.17690618 E. $O-C$ oscillates sinusoidally in accordance with the expression $O-C = 0.00047 \sin(360^\circ(E/38200) - 140^\circ)$.

Since the eclipses are not due to overlapping of the visible stellar disks, but instead to obscuration of the hot region between the components, which is displaced relative to the line connecting the stars, a shift between the photometric minimum and the spectroscopic conjunction of the stars is observed. This shift has been estimated to be from $0.025P$ to $0.05P$, where P is the orbital period of the system. According to Krzeminski [18], the radial-velocity curve convolved with the ephemeris [18] indicates that the spectroscopic conjunction of the components occurs at a phase 0.05 after the photometric eclipse (i.e., at photometric phase 0.95). Using their IR spectra, Wade [38] determined that the spectral conjunction occurs at photometric phase 0.974; the same result was obtained by Berryman *et al.* [26]. Stover *et al.* [39] reported that the spectral and photometric conjunctions coincide within the errors. Analysis of the phasing of the IR light curves of U Gem [27] indicated that the displacement of the eclipse curve is $0.040 P_{orb}$. The observed scatter in these results is due both to the unstable position of the eclipsed region relative to the line connecting the component centers and uncertainty in the time of the minimum; substantial errors can be accumulated when individual observations are separated by several decades.

When determining the system parameters, particular emphasis has been put on spectral measurements of the radial-velocity curves of the components. Based on spectroscopic studies of line profiles, Smak [40] estimated the orbital inclination of the system to be $i = 67^\circ \pm 8^\circ$. Subsequent estimates decreased the error in this value to $\pm 3^\circ$ [36]. Wade [38] first determined the radial velocities of the secondary from its NaI 8183 and 8194 Å doublet lines; the resulting half-amplitude of the radial-velocity curve was $K_2 = 284 \pm 15$ km/s. Displacements of the emission lines in the optical spectra of the system in the course of its orbital motion reflect the motion of the disk rather than of the white dwarf. Therefore, estimates of the half-amplitude of the radial-velocity curve K_1 depend on the model adopted for the motion of the disk material. Various estimates lie in the range from $K_1 = 137 \pm 8$ [39] to 265 km/s [19]. The high-time-resolution measurements of Stover [39] are considered to be the most reliable. His estimate for the component mass ratio $q = M_1/M_2 = 2.09 \pm 0.15$ for $i = 67^\circ$ yields the masses for the stars $M_1 = (1.18 \pm 0.15) M_\odot$ and $M_2 = (0.56 \pm 0.06) M_\odot$. The radius of the white dwarf derived from studies of the UV flux from the system [30] is $R_1 \sim 5.8 \times 10^8$ cm $= 0.008 R_\odot$, which is consistent with the radius of a normal white dwarf with a mass of $1.2 M_\odot$. In this case, the inner radius of the disk obtained from line-profile modeling is $0.029 R_\odot$ [39]. The radius of the secondary can be found if we assume that it is equal

to the radius of the secondary's Roche lobe: $R_2 = (0.51 \pm 0.02)R_\odot$ [39]. The corresponding luminosity of the star is almost twice that expected for an M4.5 main-sequence star. Hence, we can conclude that, since the "mass–radius" relation indicates that the star is close to the main sequence, its estimated spectral type is later than is typical for stars of the given mass. All these uncertainties are related to difficulties in deriving a spectral classification for the secondary, due to its small contribution to the total radiation of the system.

4. OPTICAL LIGHT CURVES OF U Gem IN THE QUIESCENT STATE

Extensive photometric observations of U Gem were carried out as far back as the 1960s by Mumford [20] and Paczynski [21]. Later, Krzeminski [18] and Warner and Nather [22] presented high-accuracy UBV light curves of the system in its quiescent state with high time resolution. Frank *et al.* [10] also published electro-photometric V observations of U Gem, with the aim of comparing them with the IR light curve of the system. However, the scatter of the points on all these curves is high, and their time resolution was substantially worse than that of [22].

Krzeminski's [18] V light curve of U Gem (Figs. 1a, 1b) is usually presented in various reviews as an example of the optical orbital variability of ordinary cataclysmic variables. This curve was obtained on January 1, 1963 during prolonged photometric UBV observations carried out from December 1961 to January 1963. The observed points (Fig. 2a) were taken from the plot in Fig. 2 in [18]. The error of each point is $\pm 0\overset{m}{.}004$. Figures 1a, 1b, and 2b present the average curve used to determine the system parameters.

Warner and Nather [22] studied flickering in the U Gem light curve (Figs. 1c, 1d) with very high time resolution ($\sim$2 s between adjacent points). However, the duration of both their observational data sets was close to the orbital period of the system, and both their orbital light curves have small phase gaps (at phases $\varphi \sim 0.67$–0.75 and 0.09–0.29 for curves "1098" and "1100," respectively; Figs. 1c, 1d), due to observations of the comparison star at the beginning and end of each data set. Both light curves were obtained in white light ($\sim$5000 Å) during the quiescent state of the system, on April 3 and 4, 1970, three weeks after a flare of U Gem on March 12, 1970. Some portions of the light curves display flickering amplitudes of up to $0\overset{m}{.}3$ on time scales from seconds to minutes; flickering is observed nearly throughout the light curves, except for the vicinity of the eclipse. Both curves are presented in Fig. 4 (top). The observational data points were taken from Fig. 1 in [22]. There are $\sim$3500 and 3100 points in curves 1098 and 1100, respectively. When the mean curves are drawn, the resulting formal error of $\sim 0\overset{m}{.}002$ is substantially lower than the true accuracy of the measurements; therefore, all the normal points were assigned the conditional error $\sigma = 0\overset{m}{.}035$.

We considered three optical light curves of U Gem in hot-line and hot-spot models. Table 1 presents the numbers of normal points N used to describe the shape of the mean V ($\lambda \sim 5500$ Å, Krzeminski [18]) and white-light (two $\lambda \sim 5000$ Å curves of Warner and Nather [22]) light curves. It also contains the corresponding critical χ^2 levels for the $\alpha = 0.001$ significance level.

The following intervals of probable values are suggested by previously derived parameters of the system (see Section 2). The component mass ratio $q = M_1/M_2 \sim 1.94$–2.24, $i \sim 64°$–$70°$, and $T_{\rm eff} \sim 2900$–3200 K. The disk is fairly thin in the quiescent state, $A_p \sim 6$–8, and the disk radius is $r_d/a_0 \sim 0.25$–0.40 (a_0 is the distance between the component centers of mass). The parameter α_g does not exceed 0.75, according to the model of Shakura and Sunyaev [41]. The temperature of the white dwarf in the quiescent state is 25 000–32 000 K, according to [30–32], and the radius of the white dwarf is restricted to the range $R_1/a_0 = 0.004$–0.006, since $a_0/R_\odot \sim 1.5$–1.7, according to [39]. Due to the absence of mutual eclipses of the components, the optical light curve essentially does not provide any information about q, i, or $T_{\rm eff}$. Depending on the adopted values for these parameters, we will obtain different minimum residuals for various parameters of the disk and shock region. Therefore, it is natural to adopt the values for these parameters obtained from spectral data. Finally, since phase $\varphi = 0.0$ of the observed light curve corresponds to the middle point of the eclipse of the shock region rather than the conjunction of the system components, the observed curve must be shifted by $\Delta\varphi$, where $\varphi_0(\text{conj}) = \varphi_0(\text{phot}) + \Delta\varphi$, if we wish to compare the observed and synthesized curves. We varied this parameter in the interval $\Delta\varphi = 0.25$–0.45.

In the first stage of our determination of the parameters of U Gem in the quiescent state, we used Krzeminski's [18] V light curve. The following parameter values were fixed in the calculations: $q = 2.2$, $i = 66\overset{\circ}{.}5$, $T_{\rm eff} = 3100$ K, $A_p = 7.5$ (which roughly corresponds to a half-thickness of the disk edge of $z/2 = 0.006a_0$, or an opening angle for the outer edge of the disk $\sim 2°$), $R_1/\xi = 0.010$ (ξ is the distance between the center of mass of the white dwarf and the inner Lagrange point, $\xi/a_0 = 0.58$ for $q = 2.2$), $\alpha_g = 0.75$, and $T_1 = 26\,000$ K. In this model, the temperature of the uneclipsed white dwarf

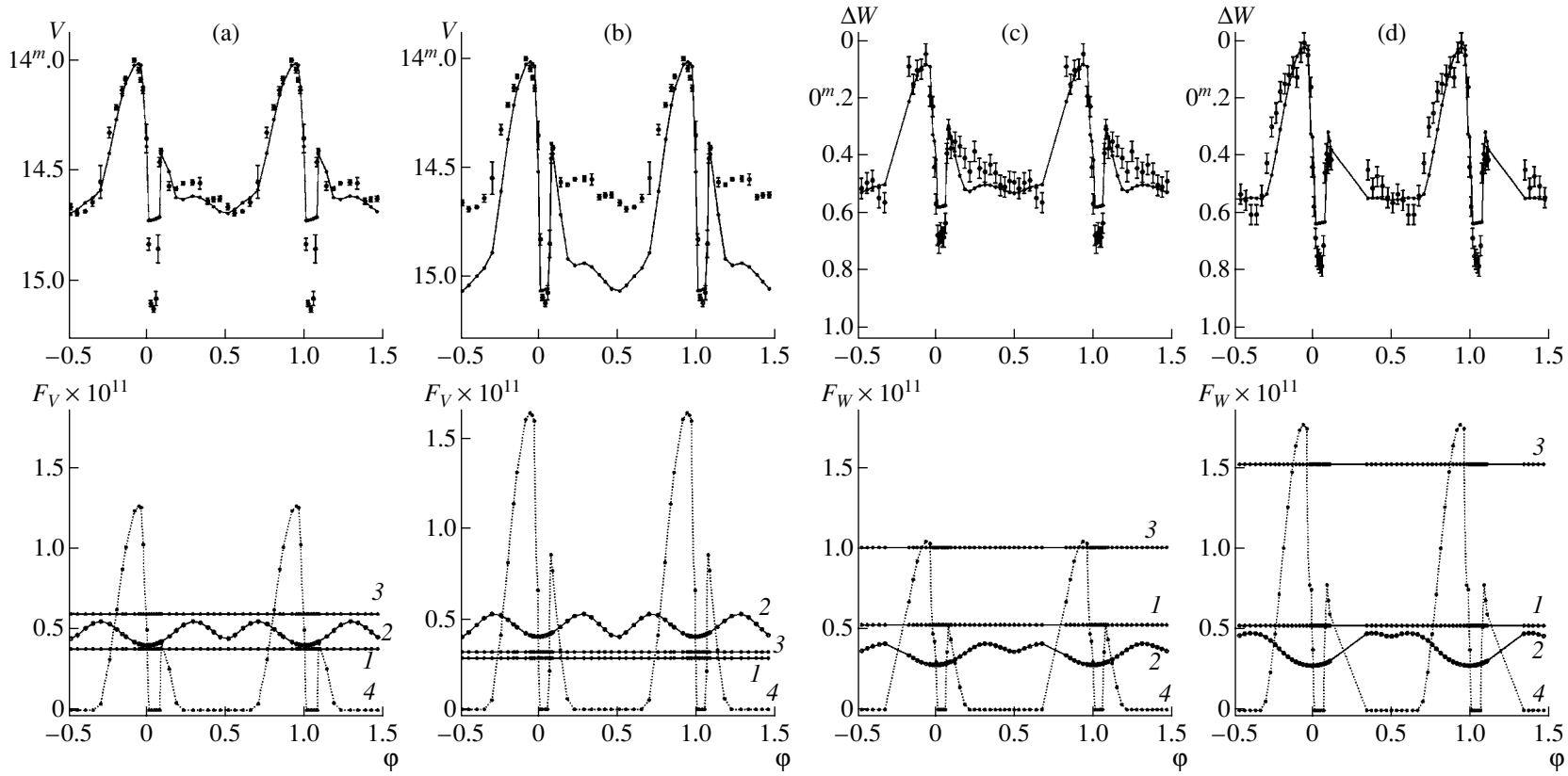

Fig. 1. Observed optical light curves of U Gem in its quiescent state according to [18, 22] and the results of the hot-spot model calculations. The top section shows the observational data (points with corresponding errors) in (a), (b) V (Krzeminski's curve [18] obtained on January 1, 1963) and (c), (d) white light ($\lambda = 5000$ Å light curves obtained by Warner and Nather [22] on April 3 and April 4, 1970), together with the theoretical curves (solid) calculated with the parameters from Table 2. In (b), the solid curve represents the theoretical light curve calculated with $r_d/a_0 = 0.3842$, $r_{sp}/a_0 = 0.073$, $\varphi_{sp} = 0.935$, $T_{sp} = 11\,595$ K, $T_b = 21\,900$ K, and $T_1 = 21\,883$ K; the remaining parameters are the same as those for the theoretical curve in (a) (Table 2). The bottom section shows the contributions of the (*1*) compact object (close to zero), (*2*) red dwarf, (*3*) circular accretion disk, and (*4*) hot spot to the total flux.

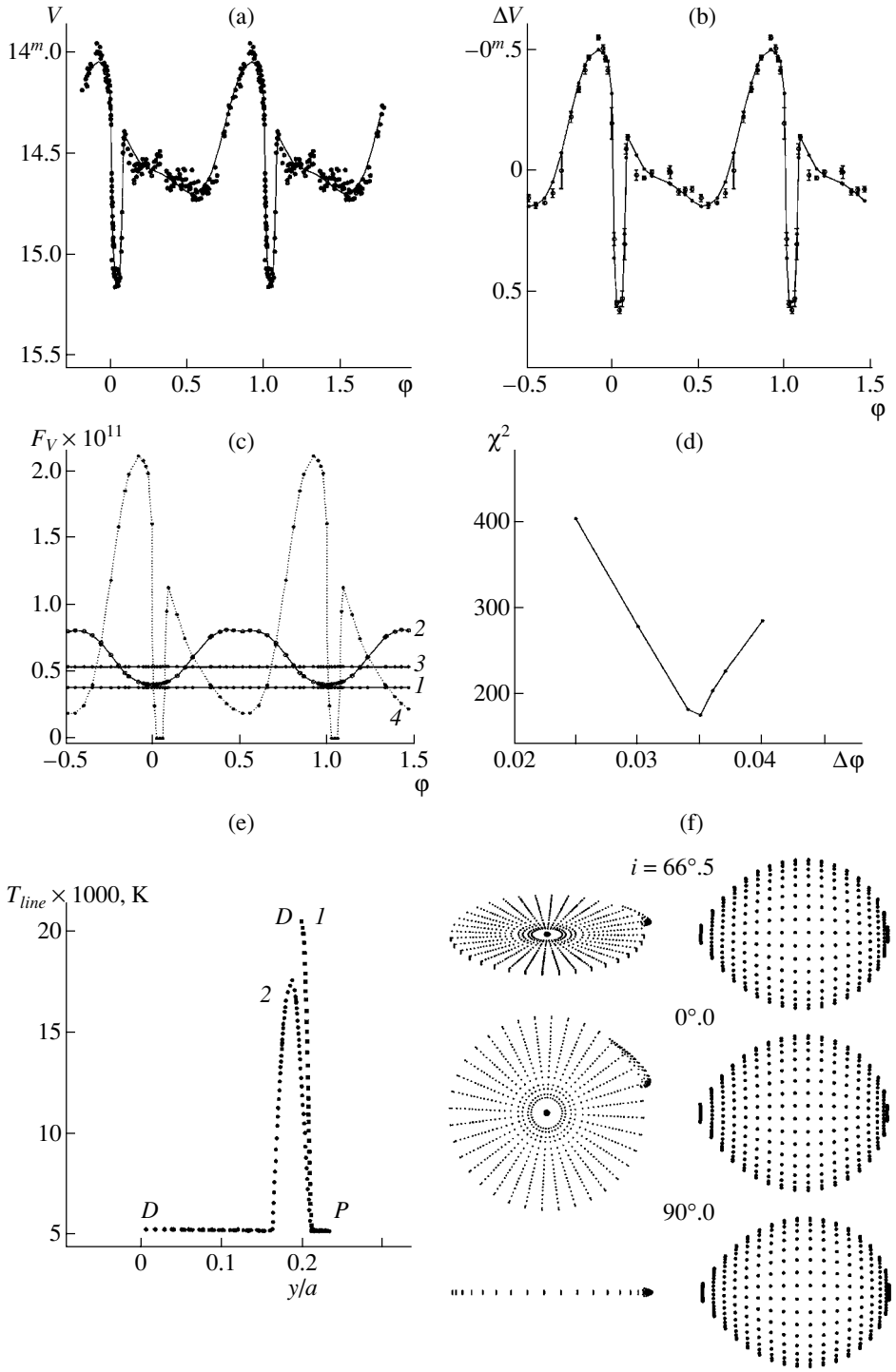

Fig. 2. Results of computations carried out in the hot-line model for the V light curve of U Gem in the quiescent state obtained by Krzeminski [18]. Shown are the (a) observed light curve (points) and (b) mean light curve (points with corresponding errors), as well as the theoretical light curve synthesized with the parameters from Table 1 (solid). (c) Contributions to the total flux from the (*1*) compact object, (*2*) red dwarf, (*3*) elliptical accretion disk, and (*4*) hot line. (d) Dependence of the χ^2 residual on the trial displacement $\Delta\varphi$ between the phase φ_0(phot) of the photometric minimum of the light curve and the phase φ_0(conj) of conjunction of the stars in the system. (e) Distribution of the brightness temperature over the hot-line surface on its (*1*) windward and (*2*) leeward sides. The D indicates the y coordinates of the tangent points between the body of the hot line and the lateral surface of the disk; the P marks the coordinate of the y pole of the ellipsoid specifying the hot line. (f) Sketches of the optical components of the system for the system parameters from Table 1 for the case when the system is viewed at orbital inclinations of $i = 66.^\circ5$, $i = 0^\circ$ (in the orbital plane), and $i = 90^\circ$.

is used only to calculate its contribution to the total flux. A higher temperature T_b for the boundary layer was used when calculating the effect of reflection on the secondary and the disk. For example, according to [32, 33], increasing the white dwarf's temperature to $T_1 = 32\,000$ K results in a $\sim 40\%$ increase in its flux. The remaining system parameters remain essentially unchanged, though the consistency between the theoretical and observed curves deteriorates due to the increase of the residual radiation during the eclipse (in our case, the fit residual increased to $\chi^2 = 468$). Thus, we fixed seven model parameters: q, i, T_{eff}, A_p, α_g, R_1, and T_1. The same parameters were fixed in the hot-spot model. As a result, the number of free parameters in the hot-line model decreased to 11: four parameters describing the elliptical disk (e, a, α_e, and T_b) and seven parameters describing the hot line (a_v, b_v, c_v, $T^{(1)}_{\max}$, $T^{(2)}_{\max}$, dy, and $y_{\min}$). The hot-spot model had the following five free parameters: the circular-disk parameters r_d and T_b, and the hot-spot parameters f_{sp}, φ_{sp}, and r_{sp}. These are described in detail in [13, 15].

We can clearly see in Fig. 1a that the optical light curve of U Gem cannot be adequately fit using the hot-spot model. Since, according to this model, the eclipse of the hot spot should be seen at orbital phase $\varphi \sim 0.4$, the code searches for a compromise between the depth of the eclipse at phase $\varphi \sim 0$ and the absence of an eclipse at phase $\varphi \sim 0.4$–0.5. Figure 1 presents one of the solutions obtained, with a minimum residual of $\chi^2_{\min} = 2203$ (see the second column in Table 2). In this case, the shift of the observed light curve is also $\Delta\varphi = 0.035$. Figure 1b presents another solution for the same curve. Here, the model fits the eclipse at phase $\varphi \sim 0$ fairly well, due to the higher temperature of the hot spot compared to the previous case. However, the out-of-eclipse part of the synthesized light curve indicates a deep minimum due to the self-eclipse of the hot spot by the edge of the disk. The light curve in Fig. 1b was synthesized for the following parameters of the close binary: $r_d/a_0 = 0.3842$, $r_{sp}/a_0 = 0.073$, $\varphi_{sp} = 0.935$, $T_{sp} = 11\,595$ K, and $T_b = 21\,900$ K; the effective temperature of the white dwarf was lower than for the first curve ($T_1 = 21\,883$ K). The remaining parameters of the close-binary system used to construct the synthesized light curve were the same as for the first curve (Table 2). In this case, the minimum residual was $\chi^2_{\min} = 14\,623$.

When a hot-line model is used, the situation changes. In spite of the fact that the minimum residual ($\chi^2_{\min} = 168$) is larger than its critical value for $N = 29$ and $\alpha = 0.001$ ($\chi^2_{0.001,29} = 58.3$), the synthesized light curve (solid curve in Figs. 2a, 2b) is consistent with the observations both near and far from the eclipse. The model is not fully consistent with the observations only at the maximum of the orbital hump. The variability of the out-of-eclipse part of the observed light curve ($\varphi \sim 0.15$–0.8) is also somewhat higher than predicted by this model (Figs. 2a, 2b).

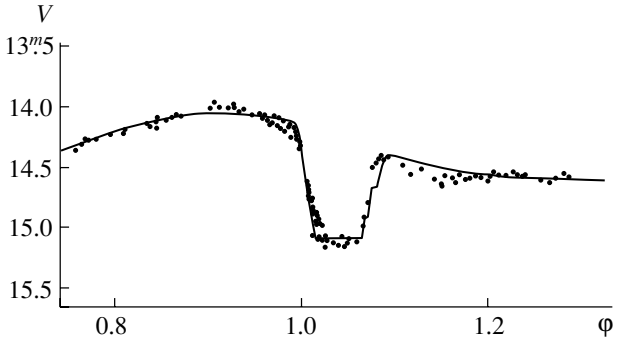

Fig. 3. Comparison of Krzeminski's [18] observations of U Gem near the light-curve minimum (points) and the theoretical hot-line model calculations made with the system parameters from Table 1 (solid curve).

In our previous studies (see, for example, [11, 12, 16]), the consistency between the hot-line model and the structure of the system studied was mainly tested by the radiation of the hot line in the out-of-eclipse part of the light curves. In the present case, we can derive the parameters of the hot line both from its direct radiation and from its eclipse by the red dwarf. Figure 3 presents a section of the observed light curve near the eclipse. It is clear that both the shape of the eclipse and its position are consistent with the hot-line model. Table 1 presents the model parameters used in the light-curve synthesis. When deriving the parameters of U Gem using Krzeminski's [18] V light curve, we varied $\Delta\varphi$, the shift of the observed light curve relative to the synthesized curve. For the observed curve, the phase $\varphi = 0.0$ corresponds to the center of the eclipse of the shock region, while, for the synthesized curve, this phase is related to the components' conjunction (see above). We independently searched for the optimal system parameters for which the residual reached its minimum for each selected $\Delta\varphi$. Figure 2d presents the dependence of the obtained minimum residual on $\Delta\varphi$. We also constructed similar dependences for the remaining light curves of U Gem analyzed here (Table 1), interpreted in both models.

Figure 2c presents the contributions of the various system components to the total flux in arbitrary units. As expected, the bulk of the flux comes from the extended shock (curve *4*), whose total eclipse by the red dwarf results in the appearance of a section with almost constant brightness at the light-curve minimum. The contribution of the white dwarf (*1*)

and elliptical disk (*3*) is smaller than the maximum flux from the hot line by a factor of four to five, and does not vary in the course of the orbital motion of the system components, i.e., none of the components is eclipsed. The variations of the flux from the red dwarf (*2*) correspond to ellipsoidal variability superimposed with the reflection effect; i.e., the heating of the stellar surface by hot radiation from the inner parts of the disk and (to a smaller extent) the white dwarf. It is clear that the fluxes of the hot line and disk dominate at orbital phases $\varphi \sim 0.65$–1.25, making it difficult to distinguish the absorption lines of the red dwarf against this background. During the very short eclipse of the shock (at phases $\varphi \sim 0.9$–1.1) the flux of the star is still almost $\sim 20\%$ smaller than the flux of the disk. The portions of the light curve where the flux of the shock region is small are formed by the radiation from the red-dwarf surface strongly heated by the reflection effect. The observed variations in the out-of-eclipse portion of the system light curve are due to the complex interaction between the radiation of the red dwarf and sections of the extended shock visible at these orbital phases.

The extent of the shock wave (hot line) beyond the boundary of the optically thick accretion disk is relatively small. Figure 2e presents the distributions of the brightness temperature over the hot-line surface on its windward (*1*) and leeward (*2*) sides. The dependence for the variation of the hot-line temperature $T(y)$ along its edge, presented by curve *2*, is similar to the analogous dependence for the hot-spot temperature if the hot spot is located on the surface of the ellipsoid describing the shape of the hot line, rather then at the outer edge of the disk. The radiation from this section of the shock produces the orbital hump observed in the light curves of cataclysmic variables. The temperature here reaches $\sim 16\,000$ K, while the full width at half maximum intensity size of the heated region (along the hot-line axis) does not exceed $0.03a_0$. The size of the radiating shock region is one-third this value on the windward side. The maximum temperature to which the matter is heated does not exceed $\sim 19\,600$ K, comparable to the temperature on the leeward side. Note that, according to the hot-line model used, it is only in the orbital plane that the truncated ellipsoid describing the radiating region of the shock merges into the disk at a tangent to it (drawn from the inner Lagrange point L_1; see [13] for more detail). The size of the truncated ellipsoid (hot line) perpendicular to the orbital plane specified by the parameter c_v can be either larger or smaller than the thickness of the outer edge of the disk z. The value of z is not specified explicitly in the model and is calculated using formula (26) of [14]. The situation when the shock region is located above the outer edge of the disk is realized in our hot-line model via appropriate choice of the semiaxis c_v of the hot-line ellipsoid perpendicular to the orbital plane. For the given light curve, the resulting size of the part of the hot-line ellipsoid that intersects the outer edge of the disk along the c_v axis ($z_{line}/a_0 \sim 0.0156$) exceeds the thickness of the outer edge of the disk above the orbital plane ($z_d/a_0 \sim 0.007$) by a factor of roughly 2–2.5. As a result, radiation from portions of the hot line will be observed at all orbital phases (except near its eclipse by the red dwarf at phases $\varphi \sim 0$). It is the lack of this radiation that makes it impossible to fit the shape of the observed light curve of U Gem in hot-spot models. Even if we supposed that the contribution of the heated red dwarf at phases $\varphi \sim 0.4$–0.6 could compensate the lack of flux from the shock, this would contradict the observations: in this case, the contribution of the star at phase 0.5 should not be lower than 52–53%, while careful spectral studies indicate that the contribution of the secondary to the total flux never reaches 50% [24, 38].

Figure 2f presents sketches of the optical components of U Gem on Jan. 1, 1962 for the parameters from Table 1, for the cases when the system is viewed at orbital inclinations of $i = 66.^\circ5$, $i = 0^\circ$ (in the orbital plane), and $i = 90^\circ$. It is obvious that, in spite of the fact that the system is in its quiescent state, the disk is large: its semimajor axis is $a \sim 0.38a_0$. A similar size was derived by Stover [39] based on modeling line profiles obtained during the quiescent state of U Gem for a circular-disk model: $r_d/a_0 \sim 0.37$–0.41. The disk is essentially circular, with its outer parts being fairly cool (the average brightness temperature is ~ 1700 K) and contributing comparatively little to the total flux. The radiating part of the hot line resembles a small bulge on the accretion disk, which also protrudes above its edge perpendicular to the orbital plane (see the sketch of the system for $i = 90^\circ$ in Fig. 2f).

The white-light light curves obtained by Warner and Nather [22] (denoted W) in the quiescent state of U Gem are similar to the V curve of Krzeminski [18], however, they display a smaller orbital-variability amplitude. Unfortunately, Warner and Nather [22] do not present their brightness estimates in magnitudes and give only the fluxes for their 2 s integration time at the maximum and minimum brightnesses, noting that U Gem was in its quiescent state during their observations. Therefore, the brightness values in Table 1 (for example, $m_{\max} = [14.0]$ and $m_{\min} = [14.7]$) are tentative, and are intended only to enable estimation of the variability amplitude within a given orbital cycle. The intensities were translated into magnitudes using the maximum observed flux from the system. If the total variability amplitude for Krzeminski's [18] V curve reaches 1^m, this amplitude is $0.^m7$ and $0.^m8$ for curves 1098 and 1100 of [22], respectively.

Curves 1098 and 1100 are uniform. Therefore, we first interpreted curve 1098 as a single curve, similar to that of Krzeminski [18]. When interpreting curve 1100, we took into account its tie to curve 1098; i.e., we took into account the fact that the flux observed in curve 1098 at photometric phase 0.21 (the corresponding spectroscopic phase for the best-fit shift, $\Delta\varphi = 0.039$, is $\varphi \sim 0.25$) corresponds to the theoretical flux obtained at this orbital phase for the best fit of curve 1098 (in this case, $m_W = 0\overset{m}{.}586$ corresponds to a flux of 1.9×10^{-11} in arbitrary units).

Note that, when interpreting curves 1098 and 1100 of [22], we fixed the error for each normal point to be $\sigma = 0\overset{m}{.}035$, close to the mean dispersion of the points in the light curve (Fig. 4a). Due to the large number of observations (about 150) averaged to obtain each normal point in the mean curve, the resulting error was worse than the accuracy of a single photometric observation.

Table 1 presents the system parameters derived from fitting the light curves; the theoretical light curves synthesized with these parameters are shown by the solid curves in the upper and middle parts of Fig. 4. The lower part of Fig. 4 presents the contribution of the system components to the total flux. We can see that the flux of the hot line is ~20% higher in curve 1100 than in curve 1098, and the eclipse is correspondingly deeper. The contributions from the remaining components vary to a substantially lesser degree.

It is striking that, for both curves of Warner and Nather [22], the flux from the hot line at orbital phases $\varphi \sim 0.53$–0.57 is very small, though it never becomes zero. This distinguishes them from Krzeminski's [18] V curve, for which the flux near phase 0.5 is also large. This is due both to the higher compactness of the hot line and to its lower mean temperature during the observations of Warner and Nather [22] compared to those of Krzeminski [18].

Figures 1c and 1d present the observations of Warner and Nather [22] analyzed in the hot-spot model. In contrast to the smooth decline and subsequent smooth rise of the flux from the hot line at orbital phases $\varphi \sim 0.2$–0.7, the hot-spot model displays a very sharp decrease in the flux from the spot at phases $\varphi \sim 0.1$–0.2, followed by its total eclipse, which can last right up to phase $\varphi \sim 0.7$, when the spot again begins to contribute to the total flux, depending on its size and azimuth (see the lower section of Fig. 1). The upper section of Fig. 1 presents examples of synthesized light curves calculated in the hot-spot model for the light curves of both Krzeminski [18] and Warner and Nather [22]. As in the hot-line model, we varied $\Delta\varphi$ when searching for the best-fit system parameters. The curves indicate that this model is not able to fit the shape of the light curves of U Gem in its quiescent state: the total flux at phases $\varphi \sim 0.3$–0.7 should be close to the flux at phase $\varphi \sim 0.01$. By appropriate selection of the parameters of the disk and hot spot, we can achieve a satisfactory fit of the shape

Table 1. Quiescent-state parameters of U Gem using the hot-line model to interpret the optical light curves

Parameters	Study/filter		
	[18]/V	[22]/W	
	Jan. 1, 1963	"1098"	"1100"
$m_{\max}$	14.0	[14.0]	[14.0]
$m_{\min}$	15.2	[14.7]	[14.8]
N	29	36	36
$\chi^2_{0.001,N}$	58.3	68.3	68.3
a/a_0	0.3810	0.3419	0.3907
e	0.0009	0.2199	0.1996
α_e, deg	137.121	149.334	124.272
$r_d(\min)/a_0$	0.3807	0.2668	0.3128
$r_d(\max)/a_0$	0.3814	0.4171	0.4687
a_v/a_0	0.0657	0.0744	0.0596
b_v/a_0	0.233	0.229	0.210
c_v/a_0	0.0297	0.0504	0.0506
$T^{(1)}_{\max}$, K	19551	8174	10055
$T^{(2)}_{\max}$, K	16108	8118	9125
$\langle T^{(1)}\rangle$, K	6050	6180	5405
$\langle T^{(2)}\rangle$, K	4140	3440	3265
$y_{\max}/a_0$	0.1980	0.2002	0.1870
$y_{\min}/a_0$	0.2085	0.2294	0.2005
dy/a_0	0.0127	0.0137	0.0188
T_b, K	36080	34840	35716
$\langle T_{\text{out}}\rangle$, K	1730	1845	1735
α_g	0.75	0.75	0.75
T_1, K	26000	26000	26000
$\Delta\varphi$	0.035	0.039	0.039
χ^2	168	51.6	38.1

When determining the system parameters, we fixed the values $q = M_1/M_2 = 2.2$, $i = 66\overset{\circ}{.}5$, $T_{\text{eff}} = 3100$ K, $A_p = 7.5$ (this corresponds to an opening angle for the disk edge of $2z/a \sim 2\overset{\circ}{.}04$, with the half-thickness of the outer edge of the disk being $z/a_0 \sim 0.007$), and $R_1/a_0 = 0.0058$. $T^{(1)}$ and $T^{(2)}$ are the brightness temperatures of the hot line on its windward (1) and leeward (2) sides.

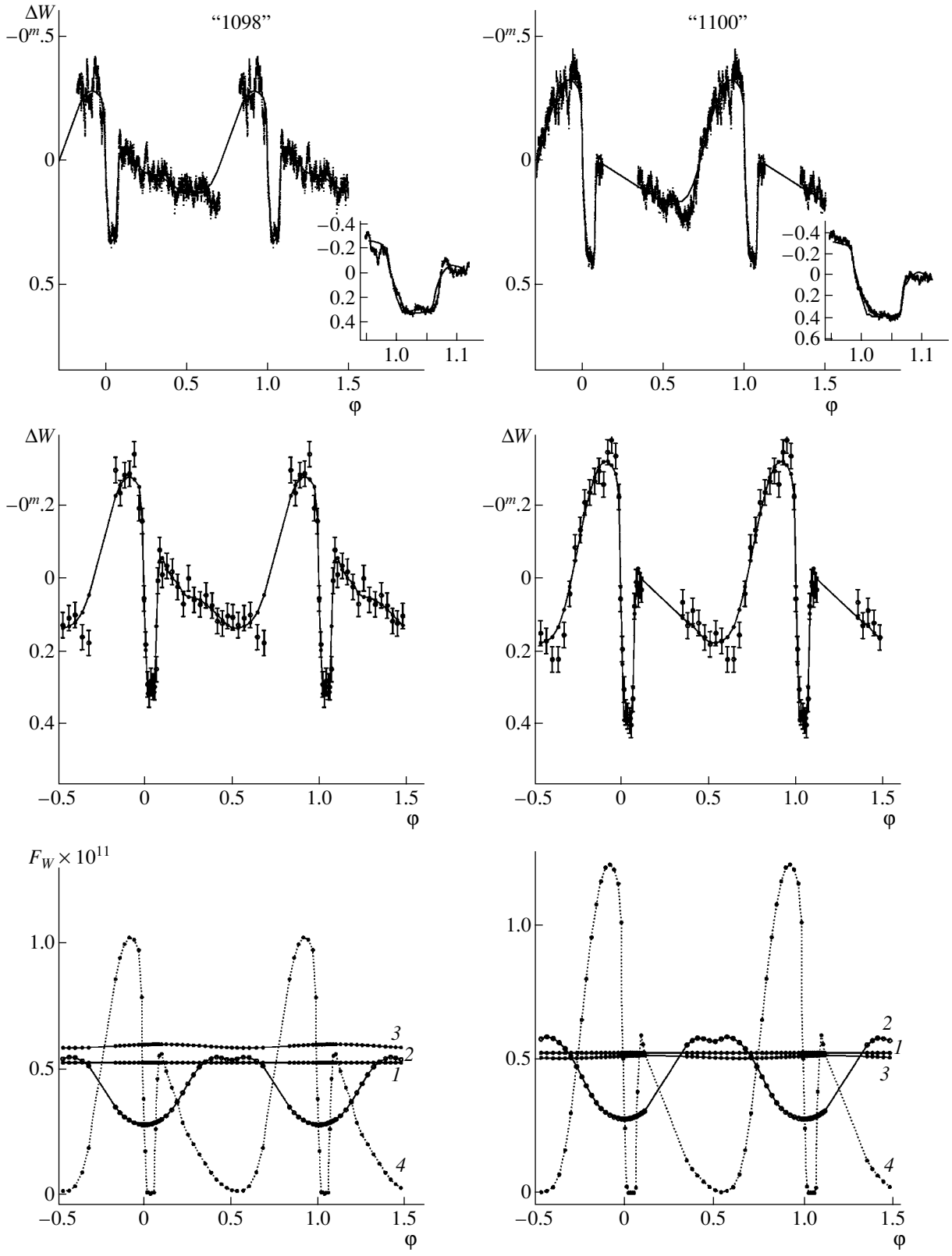

Fig. 4. Results of hot-line model calculations for Warner and Nather's [22] white-light light curves 1098 and 1100 of U Gem in the quiescent state (W). The top section shows the observed light curves, the middle section the mean curve and corresponding theoretical curve synthesized using the parameters from Table 1 (solid curves), and the bottom section the contributions of the (*1*) compact object, (*2*) red dwarf, (*3*) elliptical accretion disk, and (*4*) hot line to the total flux.

and depth of the eclipse at phase $\varphi \sim 0.01$; however, we obtain a minimum with nearly the same depth at phases $\varphi \sim 0.2$–0.7, which is not observed. Only a small increase of the flux can be obtained due to the ellipsoidality of the red dwarf's radiation. The hot-spot model not only inadequately fits the eclipsing part of the light curve, but also the shape of the hump at phase $\varphi \sim 0.85$: the theoretical light curve at these phases has a narrower peak than is observed. We have noted such results previously for other systems [12, 16]. Table 2 presents the parameters of the U Gem system used to construct the synthesized light curves in Fig. 4.

Thus, a comparison between the hot-spot and hot-line models provides convincing evidence that the latter model yields a better fit of the optical light curves of U Gem in the quiescent state.

5. IR LIGHT CURVES OF U Gem

It was demonstrated in [23, 24] that the maximum of the SED of the secondary component in U Gem in its quiescent state lies in the IR, where the star's contribution to the total flux can reach 80–90%. IR photometry of U Gem has been carried out by Frank *et al.* [25], Panek [27], and Berriman *et al.* [26]. We chose to use the light curves of U Gem obtained by Panek [27] to analyze the IR observations and determine the system parameters.

Panek's [27] J, H, and K photometric observations of U Gem were obtained on January 18, 19, and 20, 1981, 100 days after a flare. The largest flux was observed in the H filter ($\lambda \sim 16\,500$ Å). The error in a single observation at these wavelengths was $0^m.023$. The H light curve is a double wave spanning the orbital period. We used the ephemeris of [42] to convolve the light curves; phase $\varphi = 0.0$ corresponds to the center of the photometric eclipse at optical wavelengths. According to the estimate of Panek [27], the error introduced by using this ephemeris was $0.01P$ by January 1981. A figure in [27] presents individual data points for all three observing nights, and that paper also presents tables with the observational data for each night convolved with the orbital period. Normal points were obtained for a phase interval of 0.05. All three curves are consistent within $0^m.02$. The fluxes at the quadratures are different: the H-curve brightness is higher by $0^m.03$ at orbital phases 0.75–0.95 compared to the brightness at the first quadrature. In the other filters, the fluxes at the quadratures are the same within the errors.

We considered each of the three H light curves of Panek [27] presented in the Tables, as well as a mean curve taken from the corresponding figure in [27] and represented by 30 normal points, in both hot-spot and hot-line models. Figures 5a and 5b display both the individual and mean light curves. The nightly-averaged light curves of [27] are given in the upper section of Figs. 6a, 6b. Each of these consists of 20 normal points.

Table 2. Quiescent-state parameters of U Gem using the hot-spot model to interpret the V light curve of Krzeminski [18]

Parameters	Jan. 1, 1963
$m_{\max}$	14.0
$m_{\min}$	15.2
N	29
$\chi^2_{0.001,N}$	58.3
r_d/a_0	0.424
r_{sp}/a_0	0.094
φ_{sp}	0.950
T_{sp}, K	9850
α_g	0.75
T_b, K	26000
T_1, K	26000
$\Delta\varphi$	0.035
χ^2	2203

When determining the system parameters, we fixed the values $q = M_1/M_2 = 2.2$, $i = 66°.5$, $T_{\rm eff} = 3100$ K, $A_p = 7.5$ (this corresponds to an opening angle for the disk edge of $2z/a \sim 2°.06$, with the half-thickness of the outer edge of the disk being $z/a_0 \sim 0.0075$), $R_1/a_0 = 0.0058$, and $\alpha_g = 0.75$.

The procedure used to search for the best-fit system parameters for a given model was the same as that used for the optical light curves. We fixed q, i, $T_{\rm eff}$, R_1, T_1, α_g, and A_p at the same values as were obtained for the optical light curves (Table 3). We then found the best fits to the H light curve averaged over the three nights for the sequence $\Delta\varphi = 0.020$–0.050, presented in Fig. 5b. The phase shift of the light curves that yielded the minimum residual was $\Delta\varphi = 0.045$ in the hot-line model and about $\Delta\varphi = 0.046$ in the hot-spot model. In his analysis of this light curve in terms of purely ellipsoidal variability of the secondary component, Panek [27] obtained the shift $\Delta\varphi = 0.040$ [27], adopting $q = 2.0$ and $i = 67°$; the resulting synthesized curve provides a reasonable fit to the shape of the light curve at phases $\varphi \sim 0.2$–0.6 but deviates substantially from the observations in other parts of the orbital period.

Table 3 presents the system parameters derived from our fits of the H light curve of U Gem averaged

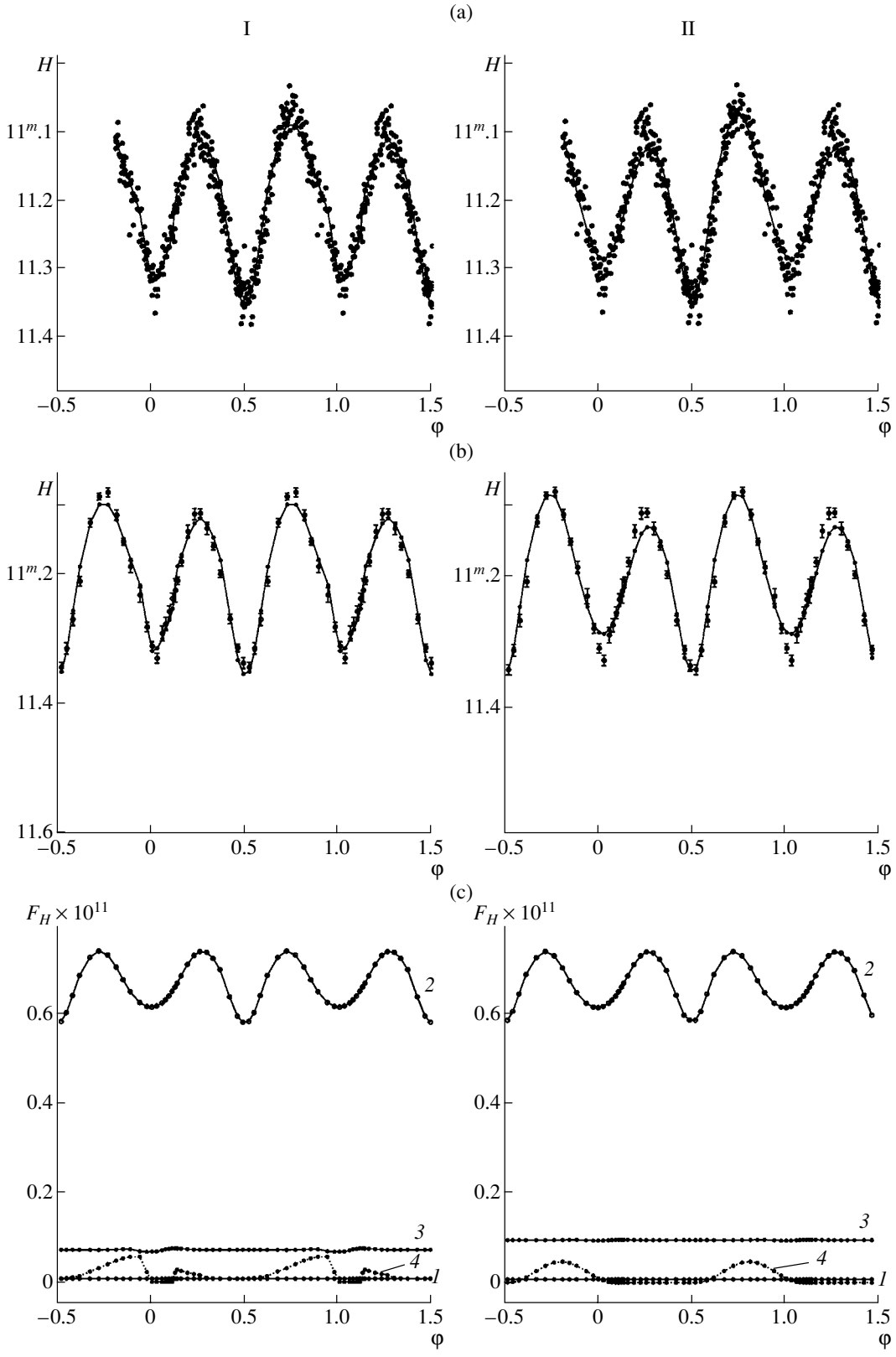

Fig. 5. *H* light curve of U Gem in its quiescent state constructed by Panek [27] from his observations of January 18–20, 1981, calculated using the hot-line (I) and hot-spot (II) models. Observed (a) and mean (b) light curves are presented. The solid curves indicate theoretical light curves calculated using the parameters of Table 3. The plots (c) display the contributions of the (*1*) compact object, (*2*) red dwarf, (*3*) accretion disk, and (*4*) region of increased energy release to the total flux.

Table 3. Quiescent-state parameters of U Gem derived using the hot-line model to interpret the H light curves

Parameters	Average for three nights	Jan. 18, 1981	Jan. 19, 1981	Jan. 20, 1981
$m_{\max}$	11.07(1)	11.05(1)	11.08(1)	11.07(1)
$m_{\min}$	11.34(1)	11.33(1)	11.35(1)	11.32(1)
N	30	20	20	20
$\chi^2_{0.001,N}$	59.7	45.3	45.3	45.3
	Hot-line model			
a/a_0	0.493	0.503	0.500	0.476
e	0.033	0.010	0.014	0.036
α_e, deg	117	108	113	124
$r_d(\min)/a_0$	0.477	0.498	0.493	0.459
$r_d(\max)/a_0$	0.509	0.508	0.507	0.493
a_v/a_0	0.045	0.047	0.048	0.052
b_v/a_0	0.207	0.201	0.202	0.223
c_v/a_0	0.0096	0.0097	0.0098	0.0112
$T^{(1)}_{\max}$, K	29150	26275	26200	35240
$T^{(2)}_{\max}$, K	20060	20740	20525	21940
$\langle T^{(1)}\rangle$, K	2265	2150	2150	4785
$\langle T^{(2)}\rangle$, K	8535	7970	8495	7510
$y_{\max}/a_0$	0.1654	0.1630	0.1639	0.1827
$y_{\min}/a_0$	0.1658	0.1635	0.1647	0.1903
dy/a_0	0.0428	0.0374	0.0406	0.0266
T_b, K	26050	26040	26020	26040
$\langle T_{\rm out}\rangle$, K	1255	1240	1245	1275
$\Delta\varphi$	0.045	0.043	0.045	0.041
χ^2	96.5	22.4	31.2	44.5
	Hot-spot model			
r_d/a_0	0.4883	0.5033	0.5243	0.5036
r_{sp}/a_0	0.1693	0.1475	0.1697	0.1336
φ_{sp}	0.8107	0.8127	0.7953	0.8125
T_{sp}, K	5495	5655	5660	5910
$\Delta\varphi$	0.046	0.040	0.040	0.044
χ^2	128	32.5	62.3	62.7

When determining the system parameters, we fixed the values $q = M_1/M_2 = 2.2$, $i = 66.^\circ5$, $T_{\rm eff} = 3100$ K, $A_p = 7.5$ (this corresponds to an opening angle of the disk edge of $2z/a \sim 2.^\circ07$, with the half-thickness of the outer edge of the disk being $z/a_0 \sim 0.009$), $R_1/a_0 = 0.0058$, $T_1 = 26\,000$ K, and $\alpha_g = 0.75$. $T^{(1)}$ and $T^{(2)}$ are the brightness temperatures of the hot line on the (1) windward and (2) leeward sides.

over three nights in both the models considered. Figures 5a and 5b show theoretical light curves for both models synthesized using the corresponding best-fit parameters (solid curves).

When the synthesized and observed light curves are compared, it is evident that the hot-line model provides a substantially better fit to the observed light curve at phases $\varphi \sim 0.9$–1.3, i.e., in the region of the eclipse and at first quadrature. This is due to the presence of the additional radiation from the hot line on the side of the incoming flow. The minimum residuals are $\chi^2 = 96.5$ and 128 for the hot-line and hot-spot models, respectively. The asymmetrical shape of the curve describing the contribution of the hot line to the total flux (Fig. 5c, model I) in the course of the orbital motion of the components also makes it possible to explain the break in the observed light curve at phase $\varphi \sim 0.9$ (Fig. 5a). In the hot-spot model,

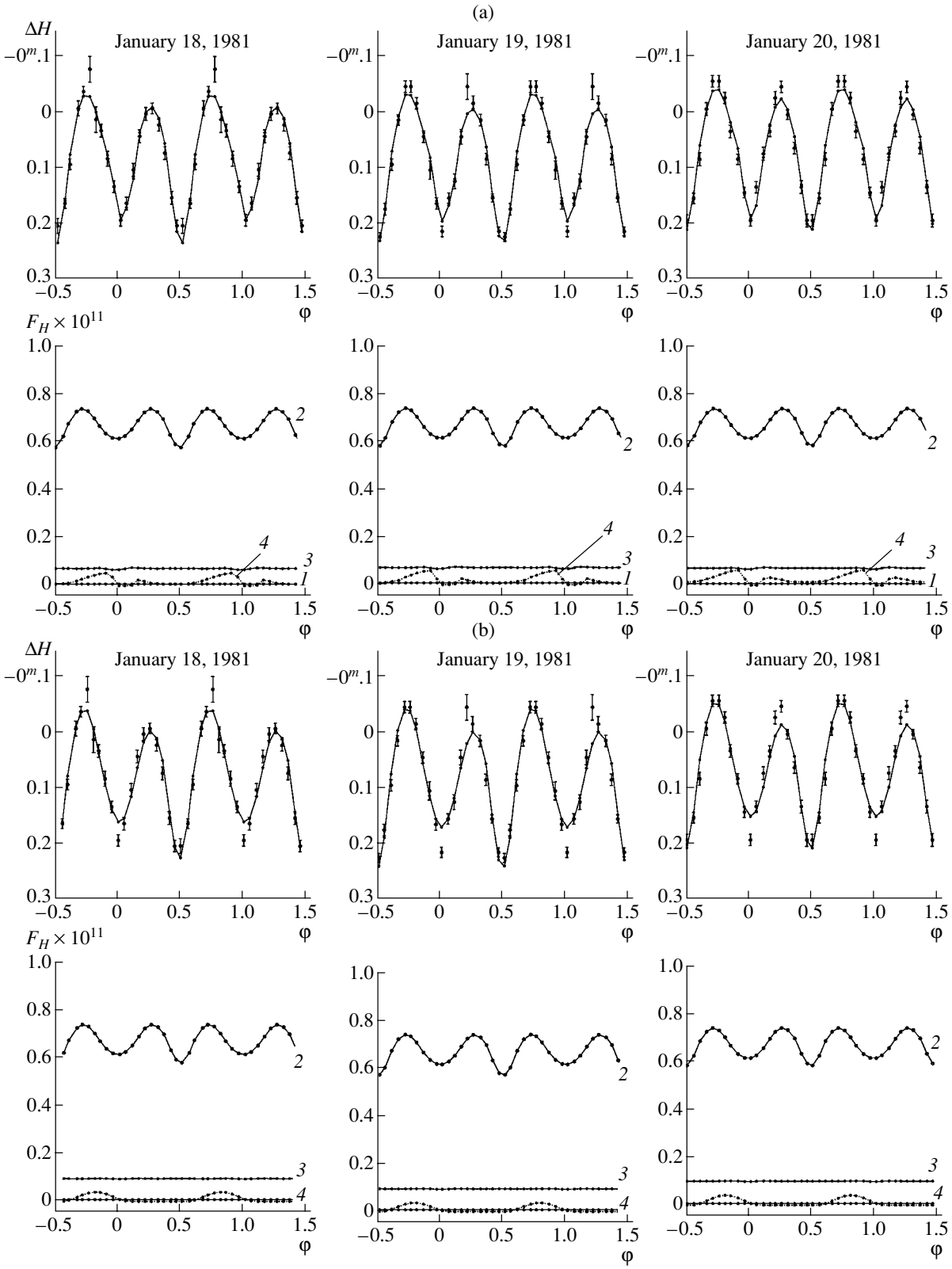

Fig. 6. Calculations for the three H light curves of U Gem in its quiescent state obtained by Panek [27] on January 18, 19, and 20, 1981 in the (a) hot-line and (b) hot-spot models. The mean (upper) and corresponding theoretical light curves synthesized using the parameters from Table 3 (solid curves) are presented; the lower section shows the contributions of the (*1*) compact object, (*2*) red dwarf, (*3*) accretion disk, and (*4*) hot line (a) or hot spot (b) to the total flux.

the contribution of the spot's radiation is symmetrical about phase $\varphi \sim 0.8$ (Fig. 5c, model II), so that the resulting brightness variations are smooth, without any sharp changes in the slope of the curve (Fig. 5a, model II).

When fitting the H light curves of U Gem obtained on each of the three nights, we tied them to the three-night average H curve; i.e., we took the observed flux $m_H = 11.127$ to correspond to the theoretical flux in arbitrary units, 8.23×10^{-12} (in the hot-line model) or 8.39×10^{-12} (in the hot-spot model), obtained for the observed magnitude of U Gem for the best fit of the averaged H light curve.

Although the night-to-night variations of the light-curve shape are minor, they are detectable. The system brightness at the quadratures differed by almost $0^m.1$ on January 18, while the fluxes at the quadratures on the two subsequent nights coincided within the errors (Figs. 6a, 6b). The deepest minimum at phase $\varphi \sim 0.5$ was observed on January 19, while the brightness in this minimum was $\sim 0^m.03$ higher on the other two nights. It is obviously impossible to describe such variations of the IR flux in a model with purely ellipsoidal variability. The presence of some additional sources of radiation is required, particularly at phases $\varphi \sim 0.25$.

Table 3 presents the results of fitting the three H light curves in both models considered. The light curves synthesized using the parameters from Table 3 are displayed by the solid curves in Figs. 6a, and 6b. A comparison of the residuals and the shapes of the theoretical light curves makes it clear that, as for the mean H light curve, the hot-line model provides a better fit of the observations for each of the individual nights. The increase of the flux at the first quadrature ($\varphi \sim 0.25$) is due to the higher temperature (both average and maximum; see Table 3) on the windward side of the hot line. The small contribution of the hot line in the region of the secondary minimum also results in its slightly smaller amplitude on January 20, compared with the preceding light curve.

The theoretical light curves calculated in the hot-spot model for the best-fit parameters and the optimal phase shift $\Delta\varphi$ differ little from the theoretical curve presented in Figs. 5a and 5b (model II). By appropriately selecting q, i, $T_{\rm eff}$ and the parameters of the spot, we can obtain a better fit of the H light curve in the hot-spot model near phase $\varphi \sim 0.25$ on each night. In this case, however, the resulting values of q, i, and $T_{\rm eff}$ are appreciably different from each other, which is physically meaningless.

The radius of the disk in the quiescent state of U Gem in the infrared obtained in both models exceeds the radius at optical wavelengths and reaches $\sim 0.5a_0$, where a_0 is the distance between the centers of mass of the system components. The size of the hot line at IR wavelengths is roughly the same as in the optical; i.e., the line resembles a small bulge on the outer edge of the disk. The average color temperature of the hot line ($\sim$5500 K) is the same as that of the hot spot ($\sim$5600 K); the difference is that the hot-line temperature is distributed over the surface of the region of interaction between the stream and disk very inhomogeneously compared to the hot-spot model. The contribution of the hot line to the total flux of the system at orbital phases $\varphi \sim 0.25$ is small due to the lower average color temperature at these wavelengths; however, even this small contribution makes it possible to obtain substantially better consistency between the observed and theoretical curves than in the hot-spot model.

6. CONCLUSIONS

Our analysis has demonstrated a striking contradiction between the hot-spot model and the observed light curves of U Gem. At the same time, the hot-line model is consistent with both the optical and IR light curves of U Gem in its quiescent state. The minimum χ^2 residuals for the hot-spot and hot-line model fits to the quiescent V light curve of Krzeminski [18] are $\chi^2_{\rm min} = 2203$ and 168, respectively; i.e., they differ by a factor of 13(!). The hot-line model for U Gem is constrained by both the orbital variability (orbital hump in the light curve) and the eclipse of the hot line by the red dwarf. In spite of this "double constraint," the hot-line model is able to fit all phases of the observed orbital light curves of U Gem in its quiescent state. In contrast, as was also found for other systems [12, 16], the hot-spot model for U Gem displays narrower peaks than are observed and, most importantly, does not reproduce the large observed depth of the eclipse of the region of interaction between the stream and disk by the body of the secondary.

The mathematical reason for the better fit of the light curves by the hot-line model is that this model is specified by a larger number of parameters than the hot-spot model. We stress, however, that the hot-line model more adequately reflects the physics of the region of interaction between the stream and disk, and has a reliable physical basis in three-dimensional gas-dynamical computations of the gas flows in close binary systems [5–10].

ACKNOWLEDGMENTS

This work was supported by the Russian Foundation for Basic Research (project codes 02-02-17524, 02-02-16462, 02-02-17642, 03-02-16622), grants in support of Leading Scientific Schools of the Russian Federation (grant nos. 162.2003.2,

388.2003.2), the State Science and Technology Project "Universities of Russia—Basic Research" (grant no. 02.03.012/1), the State Science and Technology Project "Astronomy," and INTAS (grant no. 01-491).

REFERENCES

1. V. G. Gorbatskiĭ, Astrofizika **3**, 245 (1967).
2. J. Smak, Acta Astron. **20**, 312 (1970).
3. B. Warner, *Cataclysmic Variable Stars* (Cambridge Univ. Press, Cambridge, 1995).
4. D. V. Bisikalo, A. A. Boyarchuk, O. A. Kuznetsov, and V. M. Chechetkin, Astron. Zh. **74**, 880 (1997) [Astron. Rep. **41**, 786 (1997)].
5. D. V. Bisikalo, A. A. Boyarchuk, O. A. Kuznetsov, and V. M. Chechetkin, Astron. Zh. **74**, 889 (1997) [Astron. Rep. **41**, 794 (1997)].
6. D. V. Bisikalo, A. A. Boyarchuk, V. M. Chechetkin, *et al.*, Mon. Not. R. Astron. Soc. **300**, 39 (1998).
7. D. V. Bisikalo, A. A. Boyarchuk, O. A. Kuznetsov, and V. M. Chechetkin, Astron. Zh. **75**, 706 (1998) [Astron. Rep. **42**, 621 (1998)].
8. D. V. Bisikalo, A. A. Boyarchuk, V. M. Chechetkin, *et al.*, Astron. Zh. **76**, 905 (1999) [Astron. Rep. **43**, 797 (1999)].
9. D. V. Bisikalo, A. A. Boyarchuk, V. M. Chechetkin, and O. A. Kuznetsov, Astron. Zh. **77**, 31 (2000) [Astron. Rep. **44**, 26 (2000)] .
10. M. Makita, K. Miyawaki, and T. Matsuda, Mon. Not. R. Astron. Soc. **316**, 906 (2000).
11. D. V. Bisikalo, A. A. Boyarchuk, O. A. Kuznetsov, *et al.*, Astron. Zh. **75**, 40 (1998) [Astron. Rep. **42**, 33 (1998)].
12. T. S. Khruzina, A. M. Cherepashchuk, D. V. Bisikalo, *et al.*, Astron. Zh. **78**, 625 (2001) [Astron. Rep. **45**, 538 (2001)].
13. T. S. Khruzina, Astron. Zh. **78**, 298 (2001) [Astron. Rep. **45**, 255 (2001)].
14. T. S. Khruzina, Astron. Zh. **77**, 510 (2000) [Astron. Rep. **44**, 446 (2000)].
15. T. S. Khruzina, Astron. Zh. **75**, 209 (1998) [Astron. Rep. **42**, 180 (1998)].
16. T. S. Khruzina, A. M. Cherepashchuk, D. V. Bisikalo, *et al.*, Astron. Zh. **80**, 239 (2003).
17. D. M. Himmelblau, *Applied Nonlinear Programming* (McGraw-Hill, New York, 1972; Mir, Moscow, 1975).
18. W. Krzeminski, Astrophys. J. **142**, 1051 (1965).
19. R. P. Kraft, Astrophys. J. **135**, 408 (1962).
20. G. S. Mumford, Sky Telesc. **26**, 190 (1963).
21. B. Paczynski, Acta Astron. **15**, 305 (1965).
22. B. Warner and R. E. Nather, Mon. Not. R. Astron. Soc. **152**, 219 (1971).
23. J. Stauffer, H. Spinrad, and J. Thorstensen, Publ. Astron. Soc. Pac. **91**, 59 (1979).
24. R. Wade, Astron. J. **84** (4), 562 (1979).
25. J. Frank, A. R. King, M. R. Sherrington, *et al.*, Mon. Not. R. Astron. Soc. **195**, 505 (1981).
26. G. Berriman, D. H. Beattie, I. Gatley, *et al.*, Mon. Not. R. Astron. Soc. **204**, 1105 (1983).
27. R. J. Panek, Astrophys. J. **258**, 572 (1982).
28. G. Fabbiano, L. Hartmann, J. Raymond, *et al.*, Astrophys. J. **243**, 911 (1981).
29. C. C. Wu and R. J. Panek, Astrophys. J. **262**, 244 (1982).
30. R. J. Panek and A. V. Holm, Astrophys. J. **277**, 700 (1984).
31. E. M. Sion, K. S. Long, P. Szkody, and M. Huang, Astrophys. J. **430**, L53 (1994).
32. F. H. Cheng, E. M. Sion, K. Horne, *et al.*, Astron. J. **114**, 1165 (1997).
33. K. S. Long, W. P. Blair, C. W. Bowers, *et al.*, Astrophys. J. **405**, 327 (1993).
34. K. O. Mason, M. Lampton, P. Charles, and S. Bowyer, Astrophys. J. **226**, L129 (1978).
35. J. H. Swank, E. A. Boldt, S. S. Holt, *et al.*, Astrophys. J. **226**, L133 (1978).
36. J. Smak, Acta Astron. **34** (1), 93 (1984).
37. E. L. E. Eason, J. L. Africano, A. Klimke, *et al.*, Publ. Astron. Soc. Pac. **95**, 58 (1983).
38. R. A. Wade, Astrophys. J. **246**, 215 (1981).
39. R. J. Stover, Astrophys. J. **248**, 684 (1981).
40. J. Smak, Acta Astron. **26** (2), 277 (1976).
41. N. I. Shakura and R. A. Sunyaev, Astron. Astrophys. **24**, 337 (1973).
42. S. Arnold, R. A. Berg, and J. G. Duthie, Astrophys. J. **206**, 790 (1976).

Translated by K. Maslennikov

Astronomy Reports, Vol. 47, No. 10, 2003, pp. 865–872. Translated from Astronomicheskiĭ Zhurnal, Vol. 80, No. 10, 2003, pp. 937–944.

Abundances of Carbon, Nitrogen, Oxygen, and Other Elements in the Atmosphere of the Giant 30 LMi

T. M. Rachkovskaya

Crimean Astrophysical Observatory, Nauchnyĭ, Crimea, 98409 Ukraine

Received January 16, 2003; in final form, May 8, 2003

Abstract—We have studied the star 30 LMi using high-dispersion CCD spectra and photographic observations. We estimate the star's effective temperature $T_{\rm eff} = 7210$ K, gravity $\log g = 3.34$, and microturbulence velocity $\xi_t = 5.8$ km/s. The carbon abundance, $\log\varepsilon(\mathrm{C}) = 8.57$, is close to the solar value. Nitrogen ($\log\varepsilon(\mathrm{N}) = 7.81$), oxygen ($\log\varepsilon(\mathrm{O}) = 8.76$), and sulfur ($\log\varepsilon(\mathrm{S}) = 7.20$) are slightly underabundant compared to the Sun, by -0.16 dex, -0.11 dex, and -0.13 dex, respectively. A relatively large underabundance of -0.27 dex was found for titanium ($\log\varepsilon(\mathrm{Ti}) = 4.75$), whereas zinc shows an overabundance by $+0.21$ dex ($\log\varepsilon(\mathrm{Zn}) = 4.81$). Sodium ($\log\varepsilon(\mathrm{Na}) = 6.26$), silicon ($\log\varepsilon(\mathrm{Si}) = 7.57$), calcium ($\log\varepsilon(\mathrm{Ca}) = 6.38$), chromium ($\log\varepsilon(\mathrm{Cr}) = 5.62$), iron ($\log\varepsilon(\mathrm{Fe}) = 7.51$), nickel ($\log\varepsilon(\mathrm{Ni}) = 6.34$), and yttrium ($\log\varepsilon(\mathrm{Y}) = 2.34$) exhibited abundances close to the solar values. We find no chemical anomalies characteristic of Am stars or δ Scuti stars in the spectrum of 30 LMi. © *2003 MAIK "Nauka/Interperiodica"*.

1. INTRODUCTION

A number of stars with peculiar chemical compositions are situated in the region of A and F stars in the Hertzsprung–Russell diagram. Among them, we find classical Am stars, which display enhanced abundances of elements with growth in their atomic numbers, with a deficiency of calcium and scandium also always present. Such objects are concentrated near the main sequence. A qualitatively similar pattern of abundance anomalies was found for pulsating δ Scuti stars (δ Del stars), but slightly decreased abundances of calcium and scandium were observed only for some of them (for instance, see our paper [1]). Berthet [2, 3] concluded from his spectral study of eight A–F giants that their abundance anomalies were similar to those for δ Scuti stars. Later, based on the results of [2, 3], the conclusion of Hauck [5] (based on Strömgren photometry) that 36% of 132 A–F giants had high Δm_2 values characteristic of Am stars and δ Scuti stars, and the conclusion of Kurtz [6] that δ Scuti stars are evolved Am stars, Berthet [4] proposed that, in the course of their evolution, classical Am stars lost their distinguishing peculiarity (a deficiency of calcium and scandium), become δ Scuti stars, and finally evolve into A–F giants with Am features. However, Kunzli and North [7] reject this hypothesis because, if it is correct, Am stars and A–F giants should display the same occurrence rate of binaries and similar distributions of their rotational velocities, $v \sin i$, which is not the case. According to Kunzli and North [7], the observations indicate that the percentage of reliably established binaries with periods shorter than 1000 days is only 30% among giants with Am features, whereas the frequency of binaries among Am stars is 75%; the rotational velocites of Am stars do not exceed 100 km/s, whereas A–F giants with Am features often have $v \sin i > 100$ km/s. Because of this, Kunzli and North [7] suggest that the existence of giants with Am features can be explained if all normal A and F stars can experience a brief phase when enhanced metal abundances in their atmospheres are observable.

Our goal in the current study was to determine the abundances of carbon, nitrogen, and oxygen from high-resolution spectra for objects from the list [2, 3] that are observable with our telescope. Carbon, nitrogen, and oxygen are especially interesting from the point of view of stellar evolution but currently remain poorly studied for A–F giants. We are aware only of carbon-abundance estimates for three stars, including 30 LMi, made by Berthet [2, 3]. Recall that, on average, classical Am stars have reduced C, N, and O abundances, whereas these abundances in pulsating δ Scuti stars are slightly below or about equal to the solar values (see, e.g., [8]). In our study of the giant 20 Peg [9], we presented the abundances of C, N, O, and some other elements. Here, we report the results of a similar study of 30 LMi (HD 90277 = HR 4090, $m_v = 4.73$, Sp = F0V, $v \sin i = 35$ km/s). We have confirmed the rotational velocity of 30 LMi, $v \sin i = 35$ km/s, via fitting of synthesized spectra (see below).

1063-7729/03/4710-0865$24.00

2. OBSERVATIONAL MATERIAL

Our observations were acquired with the 2.6 m reflector of the Crimean Astrophysical Observatory. Most of the spectra were taken from 1995–2001 with an American EEV15-11 CCD chip (1024 × 256 pixels). The detector was used at the Coudé focus. All parts of the spectrum, except for the vicinity of H_α, were recorded in the second order of the diffraction grating, with each spectrum covering about 70 Å. The reciprocal linear dispersion of the spectra was 3 Å per mm, and the spectral resolution was 30 000. The H_α line was recorded in the first order, with the spectral interval covered and the dispersion being 120 Å and 6 Å per mm. The signal-to-noise ratios were S/N = 50–100. The CCD spectra were reduced using standard techniques (for example, see [8]). As in our earlier observations [9], the spectral intervals for the CCD observations were centered on the CI λ5052, NI λ8683, and OI λ6156 lines. The selected spectral intervals also contain lines of other elements, whose abundances we also estimated. In addition, we observed the H_α, H_β, and H_γ lines, which were used in our calculations of the atmospheric parameters of 30 LMi. We also used spectra of 30 LMi we had obtained in 1982–1983 with the same instrument but photographically, on Kodak 103aO and 103aD plates, in the wavelength range $\lambda\lambda$ 4000–6000 Å, with reciprocal dispersions of 4, 6, and 12 Å per mm. These spectrograms were measured directly in intensities with a microphotometer.

We calculated the equivalent widths of unblended lines; if lines of elements of interest were blended with other features, synthetic spectra for the corresponding spectral intervals were calculated. As a result, in addition to nitrogen and oxygen, we obtained the first estimates of the abundances of sodium, silicon, sulfur, and zinc in the atmosphere of 30 LMi.

3. EQUIVALENT WIDTHS. OSCILLATOR STRENGTHS

We used line lists from the Vienna database [10] to identify the lines in the spectrum of 30 LMi. A list of the studied lines is presented in Table 1. The first three columns for each set of elements contain the line wavelengths λ, excitation potentials of the lower level χ, and oscillators strengths $\log gf$ according to [10]. If the oscillator strengths were taken from a different source (only for CI and SiI), a reference follows. The fourth and fifth columns of Table 1 give the equivalent widths W_λ and abundances $\log\varepsilon$ derived from individual lines. We present two values of the equivalent width of the yttrium line, YII λ5087, obtained using different detectors. We mark photographic and CCD observations "ph" and "ccd" in the sixth column of Table 1.

As noted above, some sections of the spectrum of 30 LMi were observed earlier by Berthet [2]. Figure 1 compares the equivalent widths for lines in common between [2] and the present study. We can see from Fig. 1 that our measurements give somewhat higher W_λ values. This difference may be due to differences in the continuum levels fit by the two authors. Fairly strong blending of lines is typical of stars of these spectral types, with the blending becoming stronger with higher rotational velocity. For this reason, observations covering broader wavelength intervals are desirable for more certain determination of the continuum level. Our photographic observations of 30 LMi were helpful in this respect.

4. ATMOSPHERIC PARAMETERS

The **effective temperature and gravity** were determined by comparing the observed parameters and theoretical parameters for a Kurucz model [14]. We considered the following quantities: (1) the equivalent widths W_λ of the H_α, H_β, and H_γ Balmer lines; (2) the ionization equilibrium for iron; (3) the photometric index $[c_1] = c_1 - 0.2(b-y) = 0.926$ of the four-color $uvby$ system, known to be free of interstellar reddening; and (4) the photometric index β. As noted above, theoretical values for these parameters are given by Kurucz [14]. The values of c_1 and $b-y$, which are needed to calculate $[c_1]$, and the index $\beta = 2.774$ were taken from Hauck and Mermilliod [15]. The H_α equivalent width was found using the CCD spectra; the H_β and H_γ equivalent widths were derived from both CCD and photographic observations. The equivalent widths of hydrogen lines (and lines of other elements) derived from photographic observations were obtained via simple integration over the line profiles. This method cannot be applied to our CCD observations of the hydrogen lines, because it was not possible to record the entire line profile together with its wings and fragments of the continuous spectrum on the CCD chip, while this is necessary to determine the continuum level. Thus, when measuring W_λ, we used the method we described in [9], based on comparing the observed "truncated" profile of a hydrogen line with the theoretical profile for the Kurucz model in order to estimate the line's total equivalent width. Table 2 presents the mean W_λ values for the hydrogen lines, along with their errors and the number of measurements of each line.

The values of the effective temperature, $T_{\rm eff} = 7210 \pm 50$ K, and gravity, $\log g = 3.34 \pm 0.15$ (the errors quoted are formal only), were found by averaging the parameters corresponding to the point of intersection of the β, H_α, H_β, and H_γ curves with both of the $[c_1]$ and Fe curves (Fig. 2). The adopted

Table 1. List of studied lines in the spectrum of 30 LMi

Element λ, Å	χ, eV	log gf	W_λ, mÅ	log ε	Detector	Element λ, Å	χ, eV	log gf	W_λ, mÅ	log ε	Detector
CI						4285.44	3.24	−1.20	130	7.72	ph
5052.17	7.68	−1.65		8.75*	ccd	4447.72	2.22	−1.34	200	7.55	ph
		−1.49[11]		8.56*		4484.22	3.60	−0.86	102	7.45	ph
		−1.30[12]		8.40*		4494.57	2.20	−1.14	240	7.67	ph
NI						4966.09	3.33	−0.87	102	7.25	ph
8683.40	10.33	+0.09	60	7.72	ccd	5001.87	3.88	+0.01	200	7.49	ph
8686.15	10.33	−0.30		7.90*	ccd	5049.82	2.28	−1.36	146	7.20	ccd
OI						5051.63	0.92	−2.80		7.40*	ccd
6155.98	10.74	−0.66		8.78*	ccd	5068.77	2.94	−1.04	147	7.41	ccd
6156.77	10.74	−0.48		8.75*	ccd	5133.69	4.18	+0.14	180	7.44	ph
6158.18	10.74	−0.31		8.75*	ccd	5162.27	4.18	+0.02	200	7.69	ph
NaI						5367.47	4.42	+0.44	200	7.48	ph
5889.95	0.00	+0.12	440	6.57	ph	5369.97	4.37	+0.54	229	7.57	ph
5895.92	0.00	−0.18	410	6.66	ph	5383.37	4.31	+0.64	260	7.69	ph
6154.23	2.10	−1.56		6.45*	ccd	5389.48	4.42	−0.41	90	7.55	ph
SiI						5393.17	3.24	−0.72	180	7.56	ph
6145.02	5.62	−1.48[13]	24	7.70	ccd	5405.78	0.99	−1.84	250	7.37	ph
6155.13	5.62	−0.40		7.57*	ccd	5415.20	4.39	+0.64	240	7.57	ph
8686.35	6.20	−1.20		7.45*	ccd	5424.07	4.32	+0.52	240	7.64	ph
SI						5445.04	4.39	−0.02	120	7.34	ph
8693.90	7.87	−0.48	157	7.20	ccd	5466.40	4.37	−0.63	80	7.66	ph
CaI						5572.86	3.40	−0.28	210	7.46	ph
4425.44	1.88	−0.29	168	6.10	ph	5576.10	3.43	−1.00	120	7.58	ph
4578.55	2.52	−0.17	120	6.15	ph	5586.76	3.37	−0.12	210	7.28	ph
5581.96	2.52	−0.57	110	6.46	ph	5615.64	3.33	+0.05	300	7.81	ph
5588.75	2.53	+0.31	230	6.45	ph	6151.62	2.18	−3.30	16	7.78	ccd
5601.28	2.53	−0.55	160	6.80	ph	6157.73	4.07	−1.26		7.60*	ccd
6162.17	1.90	−0.17	222	6.34	ccd	7780.55	4.47	−0.27	102	7.50	ccd
TiII						FeII					
4312.86	1.18	−1.09	260	4.82	ph	4273.33	2.70	−3.26	190	7.53	ph
4386.84	2.60	−0.94	160	5.02	ph	4491.40	2.86	−2.70	220	7.32	ph
4395.03	1.08	−0.51	320	4.70	ph	4515.34	2.84	−2.45	280	7.57	ph
4468.51	1.13	−0.60	288	4.50	ph	4520.22	2.81	−2.60	260	7.52	ph
4779.98	2.05	−1.26	126	4.65	ph	4555.89	2.83	−2.16	320	7.65	ph
4805.08	2.06	−0.96	180	4.72	ph	4576.34	2.84	−2.92	223	7.54	ph
5185.90	1.89	−1.37	160	4.84	ph	4629.34	2.81	−2.33	290	7.50	ph
CrI						5234.60	3.22	−2.23	295	7.69	ph
4254.33	0.00	−0.11	290	5.53	ph	5362.87	3.20	−2.74	200	7.42	ph
5206.04	0.94	+0.02	240	5.56	ph	6147.74	3.89	−2.72	128	7.46	ccd
CrII						6149.26	3.89	−2.72	118	7.39	ccd
4558.72	4.07	−0.45	260	5.63	ph	NiI					
4634.10	4.07	−0.99	220	5.82	ph	4714.41	3.38	+0.26	138	6.02	ph
5237.33	4.07	−1.16	150	5.46	ph	NiII					
5313.59	4.07	−1.65	120	5.75	ph	4015.47	4.03	−2.42	120	6.68	ph
FeI						ZnI					
3922.91	0.05	−1.65	300	7.22	ph	4810.53	4.08	−0.14	140	4.81	ph
4021.87	2.76	−0.73	200	7.43	ph	YII					
4157.78	3.42	−0.40	170	7.34	ph	4900.12	1.03	−0.09	183	2.52	ph
4213.65	2.84	−1.29	140	7.58	ph	5087.42	1.08	−0.17	98, 106	2.15	ccd, ph

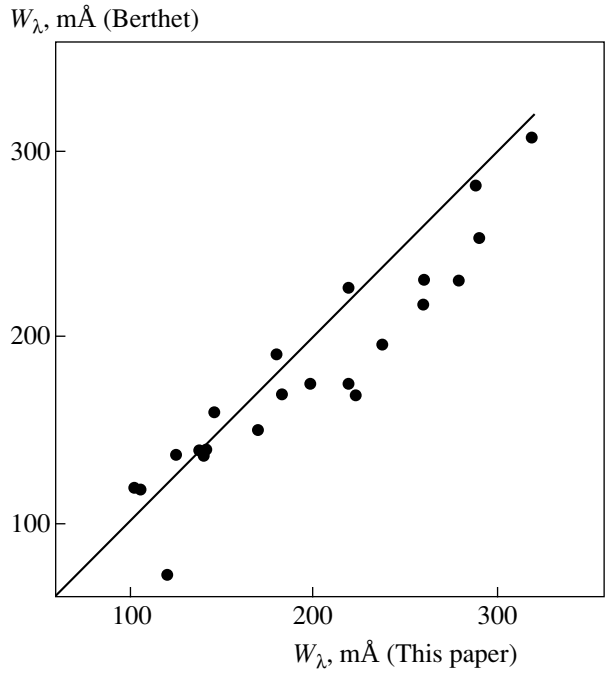

Fig. 1. Comparison of the line equivalent widths for 30 LMi from our measurements (horizontal axis) and the measurements of Berthet [2] (vertical axis).

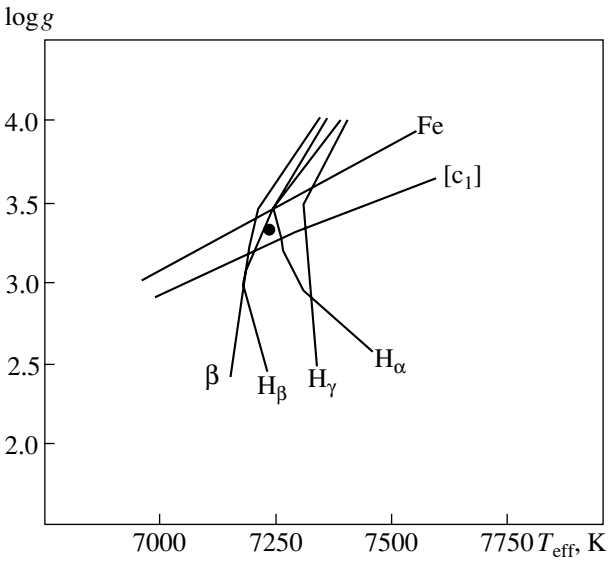

Fig. 2. Diagram for the determination of the effective temperature and gravity of 30 LMi. The filled circle corresponds to the adopted model.

model is shown by the filled circle in Fig. 2. For comparison, Berthet [2] derived the values $T_{\rm eff} = 7440$ K and $\log g = 3.33$.

The **microturbulence velocity**, ξ_t, can be found from the condition that the abundances of an element calculated from lines of one of its ions do not show a systematic trend with increasing equivalent width. This requires that we have measurements of a sufficiently large number of lines whose equivalent widths cover a fairly broad range. We can see from Table 1 that this requirement is satisfied to various degrees by CaI, TiII, CrII, FeI, and FeII. The abundances $\log \varepsilon$ of these elements were calculated for several values of ξ_t. The resulting microturbulence velocities that yield no correlation between $\log \varepsilon$(El) and W_λ are collected in Table 3.

It follows from Table 3 that the largest difference of the ξ_t values derived from different ions is 1.0 km/s. We finally adopted the value $\xi_t = 5.8$ km/s derived from FeI as being the most reliable one for our abundance calculations; this value also turns out to be close to the weighted mean for all the elements, $\xi_t = 5.9$ km/s (Table 3). As an example, Fig. 3 displays the relation between $\log \varepsilon$(Fe) and W_λ for FeI for $\xi_t = 5.8$ km/s. Berthet [2] derived a lower microturbulence velocity for 30 LMi from FeI lines: $\xi_t = 4.6$ km/s.

5. CHEMICAL COMPOSITION

We estimated the elemental abundances, $\log \varepsilon(\mathrm{El}) = \log \times [N(\mathrm{El})/N(\mathrm{H})] + 12$ (on this scale, $\log \varepsilon(\mathrm{H}) = 12$ for hydrogen), in the atmosphere of 30 LMi using $T_{\rm eff} = 7210$ K, $\log g = 3.34$, and $\xi_t = 5.8$ km/s, assuming LTE. The abundances calculated from individual lines are collected in the fifth column of Table 1. The asterisks mark $\log \varepsilon$(El) values obtained by fitting synthetic spectra. The mean $\log \varepsilon$ values for different ions are presented in the second column of Table 4; we give the number of lines used to calculate the average next to these values in parentheses. The third column of this table contains σ, the rms deviation from the mean abundance. We postpone a full discussion of the data in Table 2 to later sections, and will consider here each element in turn, simultaneously comparing our results for 30 LMi with the results for 20 Peg [9]. We will first consider iron, whose lines are the most numerous in the observed sections of the spectrum.

Iron. Table 1 shows that we estimated the iron abundance using mainly the equivalent widths, except for two lines for which we determined $\log \varepsilon$(Fe) by fitting synthetic spectra. The abundances derived from the FeI and FeII lines are the same, $\log \varepsilon(\mathrm{Fe}) = 7.51$, which is lower than the estimate of Berthet [2] by 0.3 dex. What could be the origin of this difference? We cannot give a firm answer to this question at this time and note only the following. In contrast to Berthet, we used new Kurucz models, as well as more recent data on the oscillator strengths for lines of iron and other elements. Berthet's lists [2, Table 2] contain lines that are blends according to the

Table 2. Hydrogen-line equivalent widths for 30 LMi

Line	W_λ, Å	Number of observations
H_α	9.70 ± 0.10	3
H_β	11.60 ± 0.60	4
H_γ	13.20 ± 0.65	3

Table 3. Microturbulence velocity from lines of different ions

Ion	ξ_t, km/s	Number of lines
CaI	5.9	6
TiII	5.4	7
CrII	6.0	4
FeI	5.8	30
FeII	6.4	11
Mean	5.9	58

model of 30 LMi of [10] (this is true not only of iron, but also of other elements), and these lines are clearly seen in Table 2 of [2] to give overestimated abundances compared to estimates obtained using other lines. The iron abundance of the giant 20 Peg found by us earlier, $\log\varepsilon(\mathrm{Fe}) = 7.63$, is also somewhat lower than the estimate of Berthet [3] (by 0.14 dex). Note also that, according to Rentzsch-Holm [16], the non-LTE corrections for the temperatures of 30 LMi and 20 Peg ($T_{\mathrm{eff}} = 6970$ K, $\log g = 3.35$) are about +0.07 dex, and both Berthet and we assumed LTE in our calculations.

Carbon. We observed only one line of this element, CI λ5052.17, blended with the FeI λ5051.63 line, and therefore calculated the carbon abundance by fitting a synthetic spectrum. The oscillator strengths for the CI λ5052.17 line presented in the literature differ fairly markedly (Table 1), and we found it necessary to calculate the carbon abundance with each of three $\log gf$ values; these results are presented in the fifth column of Table 1. Figure 4 demonstrates a fully satisfactory agreement between the observed and calculated profiles. We can see from Table 1 that the difference between the highest and lowest carbon abundances is 0.35 dex; their mean, $\log\varepsilon(\mathrm{C}) = 8.57$, is given in Table 4. The mean carbon abundance for 20 Peg, calculated using the same lines and with the same oscillator strengths, coincides with the value found for 30 LMi: $\log\varepsilon(\mathrm{C}) = 8.58$. According to Rentzsch-Holm [16], the non-LTE corrections to the carbon abundances of 30 LMi and 20 Peg do not exceed −0.1 dex; we can see that this correction is lower than the scatter in the carbon abundances due to uncertainties in the oscillator strengths.

Table 4. Elemental abundances in the atmosphere of 30 LMi

Element	$\log\varepsilon$	σ	[X]	$\Delta\log\varepsilon$(El)
CI	8.58	−	+0.03	+0.13
NI	7.81(2)	0.09	−0.16	
OI	8.76(3)	0.01	−0.11	
NaI	6.26(3)	0.13	−0.07	
SiI	7.57(3)	0.10	+0.02	
SI	7.20(3)		−0.13	
CaI	6.38(6)	0.23	+0.02	+0.24
TiII	4.75(7)	0.16	−0.27	−0.14
CrI	5.54(2)	0.02		
CrII	5.66(4)	0.14		
	5.62		−0.05	−0.09
FeI	7.51(32)	0.16	+0.01	
FeII	7.51(11)	0.10		
NiI	6.02(1)			
NiII	6.67(1)			
	6.34		+0.09	+0.13
ZnI	4.81(1)		+0.21	
YII	2.34(2)	0.18	+0.10	−0.08

Nitrogen. The two nitrogen lines observed in the spectrum of 30 LMi gave similar abundances, $\log\varepsilon(\mathrm{N}) = 7.81$. The nitrogen abundance for 20 Peg derived from the same lines and with the $\log gf$ values from Table 1 was only slightly higher ($\log\varepsilon(\mathrm{N}) = 8.00$).

Oxygen. The oxygen abundances calculated from three lines by fitting synthetic spectra differ slightly (Table 1) and give the average value $\log\varepsilon(\mathrm{O}) = 8.76$ (close to the value derived in a similar way for 20 Peg, $\log\varepsilon(\mathrm{O}) = 8.78$). Figure 5 compares the observed and calculated spectra for 30 LMi in the wavelength range $\lambda\lambda$6153–6160. According to Takeda [17], the non-LTE corrections to the oxygen abundances of 30 LMi and for 20 Peg do not exceed −0.04 dex.

Sodium. We observed three sodium lines. Two of them, NaI λ5889 and λ5895, are fairly strong resonance lines, and gave the abundances $\log\varepsilon(\mathrm{Na}) = 6.57$ and $\log\varepsilon(\mathrm{Na}) = 6.66$, respectively. The λ6154 line, which we used to fit a synthetic spectrum, gives $\log\varepsilon(\mathrm{Na}) = 6.45$. Mashonkina *et al.* [18] present non-LTE calculations for sodium lines demonstrating that the sodium abundances derived from LTE

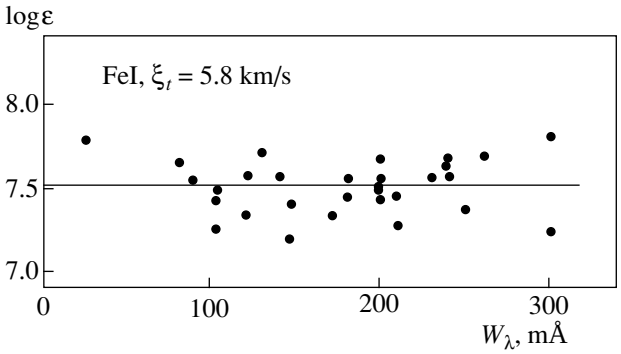

Fig. 3. Iron abundances from FeI lines as a function of equivalent width, for $\xi_t = 5.8$ km/s.

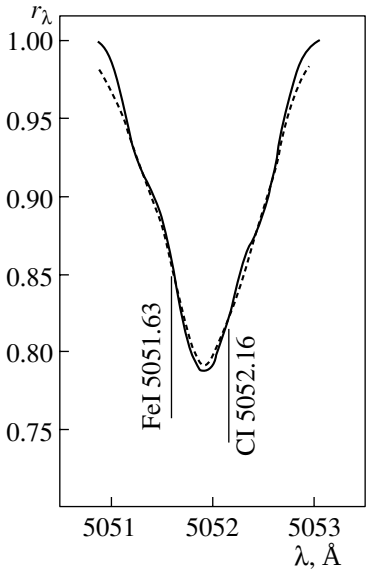

Fig. 4. Comparison of the synthetic (solid) and observed (dashed) spectra near λ5052.

calculations are too high, with the excess depending strongly on $T_{\rm eff}$ and $\log g$. We accordingly introduced corrections to our abundances for 30 LMi, approximately equal to -0.1 dex and -0.45 dex for the λ6154 line and the λ5889 and λ5895 lines. The $\log\varepsilon(\mathrm{Na}) = 6.26$ value from Table 4 is an average of the non-LTE-corrected abundances from the three lines. For 20 Peg [9], whose sodium abundance was derived from the NaI λ6154 and λ6160 lines only, we obtain $\log\varepsilon(\mathrm{Na}) = 6.27$ after the non-LTE correction, similar to the value for 30 LMi.

Silicon. Data from the literature show fairly a large scatter in the oscillator strengths of the silicon lines. We applied $\log gf$ values for the various lines from different sources (Table 1), seeking better agreement of the calculated abundances. The average silicon abundance for 30 LMi derived from three lines

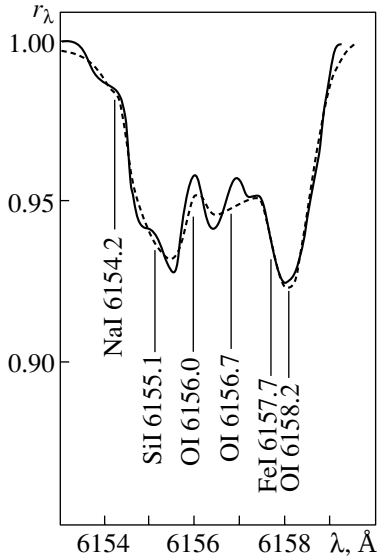

Fig. 5. Same as Fig. 4, but near λ6156.

was $\log\varepsilon(\mathrm{Si}) = 7.57$. For 20 Peg, the silicon abundance derived from the same lines was $\log\varepsilon(\mathrm{Si}) = 7.69$.

Sulfur. The sulfur abundance, $\log\varepsilon(\mathrm{S}) = 7.20$, was derived from the equivalent width of the $\lambda\lambda$8693.14, 8693.93, 8694.63 triplet. The same lines give a similar value for 20 Peg, $\log\varepsilon(\mathrm{S}) = 7.28$.

Calcium. We derived the calcium abundance $\log\varepsilon(\mathrm{Ca}) = 6.38$ from six lines; this abundance for 20 Peg is $\log\varepsilon(\mathrm{Ca}) = 6.44$.

Titanium. The mean titanium abundance derived from seven TiII lines is $\log\varepsilon(\mathrm{Ti}) = 4.75$, approximately 0.67 dex below the value derived for 20 Peg from TiI lines [9]. Note that our estimate of the microturbulence velocity from the TiII lines was the lowest compared to the values derived from other ions ($\xi_t = 5.4$ km/s); Table 3); nevertheless, calculations with this velocity result in a titanium abundance that is higher by only 0.09 dex.

Chromium. Two chromium lines for CrI and CrII demonstrated similar chromium abundances; the average of the two values is $\log\varepsilon(\mathrm{Cr}) = 5.65$.

Nickel, zinc, yttrium. Tables 1 and 4 indicate that the abundances of these elements were determined using only one or two lines. The abundances calculated from the NiI and NiII lines differ fairly strongly (by 0.6 dex), while their mean value is $\log\varepsilon(\mathrm{Ni}) = 6.34$, close to that obtained earlier for 20 Peg ($\log\varepsilon(\mathrm{Ni}) = 6.32$). Roughly the same is true for yttrium, whose abundances in 30 LMi and 20 Peg are $\log\varepsilon(\mathrm{Y}) = 2.34$ and $\log\varepsilon(\mathrm{Y}) = 2.41$. The difference between the $\log\varepsilon(\mathrm{Y})$ abundances corresponding to the two listed equivalent widths for the YII λ5087.42 line (Table 1) is 0.05 dex. The only zinc

line we observed gives the abundance $\log\varepsilon(\mathrm{Zn}) = 4.81$.

We thus conclude that there are no major differences between the abundances of elements we have analyzed in the atmospheres of both the giants 30 LMi and 20 Peg.

6. DISCUSSION

Let us consider Table 4. Its fourth column compares our abundance estimates for the atmosphere of 30 LMi with the solar values according to Grevesse and Noels [19]: $[\mathrm{X}] = \log\varepsilon(\mathrm{El})_* - \log\varepsilon(\mathrm{El})_\odot$, where we have used weighted mean values for 30 LMi, $\log\varepsilon(\mathrm{El})$, for elements observed in different ionization states. We find the largest deficiency compared to the solar value (-0.27 dex) for titanium and the largest excess for zinc ($+0.21$ dex); note that the titanium abundance is fairly certain, whereas the zinc abundance was derived from a single line (Table 1). It follows from Table 4 that the abundances of oxygen, sulfur, and nitrogen for 30 LMi show slight deficiencies (0.11–0.16 dex), whereas the abundances of other elements are near-solar. Even without plotting the data, a careful inspection of the fourth column of Table 4 shows that 30 LMi does not demonstrate the abundance trend with atomic number that is observed for classical Am stars or δ Scuti stars. The same seems to be true for 20 Peg, although we studied fewer elements for that star than for 30 LMi.

Finally, the fifth column of Table 4 compares our elemental abundances and those of Berthet [2], $\Delta\log\varepsilon = [\log\varepsilon(\mathrm{El}) - \log\varepsilon(\mathrm{Fe})]_{\mathrm{author}} - [\log\varepsilon(\mathrm{El}) - \log\varepsilon(\mathrm{Fe})]_{[2]}$; as usual, the elemental abundances are considered relative to iron, the most reliable value, to minimize the influence of possible errors in the stellar-atmosphere parameters. Comparing these two sets of results, we find the largest difference for calcium: our estimates give a $\log\varepsilon(\mathrm{Ca})$ value that is 0.24 dex higher than the estimate of [2], whereas the calcium abundances for 20 Peg from the two sources are nearly the same. Our carbon and nickel abundances for 30 LMi are 0.13 dex higher than the values of Berthet [2]; our nickel abundance for 20 Peg [3] is also slightly higher (by 0.07 dex). Our abundances of yttrium, chromium, and titanium for 30 LMi are lower than those of Berthet [2] by 0.08, 0.09, and 0.14 dex, respectively. We derived an even lower yttrium abundance for 20 Peg than Berthet [3] (by -0.42 dex, with this estimate being based on the single YII λ5087 line), and a higher abundance of titanium (by $+0.47$ dex); however, in contrast to 30 LMi, the titanium abundance of 20 Peg was determined from TiI lines.

7. CONCLUSIONS

The main results of our study of the giant 30 LMi are the following. We have determined the star's atmospheric parameters: its effective temperature $T_{\mathrm{eff}} = 7210$ K, gravity $\log g = 3.34$, and microturbulence velocity $\xi_t = 5.8$ km/s.

We have derived the abundances of thirteen elements in the atmosphere of 30 LMi, including the first abundance estimates for nitrogen, oxygen, sodium, silicon, sulfur, and zinc. The abundances of carbon ($\log\varepsilon(\mathrm{C}) = 8.57$), sodium ($\log\varepsilon(\mathrm{Na}) = 6.26$), silicon ($\log\varepsilon(\mathrm{Si}) = 7.57$), calcium ($\log\varepsilon(\mathrm{Ca}) = 6.38$), chromium ($\log\varepsilon(\mathrm{Cr}) = 5.62$), iron ($\log\varepsilon(\mathrm{Fe}) = 7.51$), nickel ($\log\varepsilon(\mathrm{Ni}) = 6.34$), and yttrium ($\log\varepsilon(\mathrm{Y}) = 2.34$) are close to the solar values. The abundances of oxygen ($\log\varepsilon(\mathrm{O}) = 8.76$), sulfur ($\log\varepsilon(\mathrm{S}) = 7.20$), and nitrogen ($\log\varepsilon(\mathrm{N}) = 7.81$) provide evidence for slight deficiencies of these elements, by -0.11, -0.13, and -0.16 dex, respectively. A larger underabundance (by -0.27 dex) is demonstrated by titanium ($\log\varepsilon(\mathrm{Ti}) = 4.75$). The deficiency of titanium is the most obvious peculiarity of 30 LMi compared to the Sun. We have detected an overabundance of zinc (by $+0.21$ dex).

In conclusion, our spectroscopic study of the giant 30 LMi has found no significant anomalies in the chemical composition of the star's atmosphere; in particular, we have found no peculiarities characteristic of Am stars or δ Scuti stars.

ACKNOWLEDGMENTS

This study was partially supported by the International Science Foundation (grant UIC200).

REFERENCES

1. T. M. Rachkovskaya, Izv. Krym. Astrofiz. Obs. **80**, 3 (1988).
2. S. Berthet, Astron. Astrophys. **227**, 156 (1990).
3. S. Berthet, Astron. Astrophys. **251**, 171 (1991).
4. S. Berthet, Astron. Astrophys. **253**, 451 (1992).
5. B. Hauck, Astron. Astrophys. **155**, 371 (1986).
6. D. W. Kurtz, Astrophys. J., Suppl. Ser. **32**, 651 (1976).
7. M. Kunzli and P. North, Astron. Astrophys., Suppl. Ser. **127**, 277 (1998).
8. T. M. Rachkovskaya, Astron. Zh. **77**, 264 (2000) [Astron. Rep. **44**, 227 (2000)].
9. T. M. Rachkovskaya, Astron. Zh. **79**, 841 (2002) [Astron. Rep. **46**, 760 (2002)].
10. N. E. Piskunov, F. Kupka, T. A. Ryabchikova, *et al.*, Astron. Astrophys., Suppl. Ser. **112**, 525 (1995).
11. W. L. Wiese, M. W. Smith, and B. M. Glennon, NSRDS–NBS 4 **1**, 34 (1966).
12. I. F. Bikmaev, T. A. Ryabchikova, H. Bruntt, *et al.*, Astron. Astrophys. **389**, 537 (2002).

13. F. Thevenin, Astron. Astrophys., Suppl. Ser. **82**, 179 (1990).
14. Kurucz, CD-ROM No. 13 (1993).
15. B. Hauck and M. Mermilliod, Astron. Astrophys., Suppl. Ser. **129**, 431 (1998).
16. I. Rentzsch-Holm, Astron. Astrophys. **312**, 966 (1996).
17. Y. Takeda, Publ. Astron. Soc. Jpn. **49**, 471 (1997).
18. L. I. Mashonkina, V. V. Shimanskiĭ, and N. A. Sakhibullin, Astron. Zh. **77**, 893 (2000) [Astron. Rep. **44**, 790 (2000)].
19. N. Grevesse and A. Noels, in *Proceedings of the 6th Ann. October Astrophys. Conference in College Park, Maryland, 1995,* Ed. by S. S. Holt and G. Sonneborn (Astron. Soc. Pac., San Francisco, 1996), p. 117; ASP Conf. Ser. **99**, 117 (1996).

Translated by N. Samus'

Astronomy Reports, Vol. 47, No. 10, 2003, pp. 873–882. Translated from Astronomicheskiĭ Zhurnal, Vol. 80, No. 10, 2003, pp. 945–955.

Spectral–Temporal Evolution of Low-Frequency Pulsations in the Microwave Radiation of Solar Flares

V. V. Zaitsev[1], A. G. Kislyakov[1,2], S. Urpo[3], A. V. Stepanov[4], and E. I. Shkelev[2]

[1] *Applied Physics Institute, Russian Academy of Sciences, ul. Ul'yanova 46, Nizhni Novgorod, 603950 Russia*

[2] *Lobachevskiĭ State University, ul. Gagarina 23, Nizhni Novgorod, 603950 Russia*

[3] *Metsähovi Radio Observatory, Metsähovintie 114, FIN-02540, Kylmälä, Finland*

[4] *Main Astronomy Observatory, Russian Academy of Sciences, Pulkovo sh. 65, St. Petersburg, 196140 Russia*

Received February 18, 2003; in final form, May 8, 2003

Abstract—Low-frequency pulsations of 22 and 37 GHz microwave radiation detected during solar flares are analyzed. Several microwave bursts observed at the Metsähovi Radio Observatory are studied with time resolutions of 100 and 50 ms. A fast Fourier transformation with a sliding window and the Wigner–Ville method are used to obtain frequency–time diagrams for the low-frequency pulsations, which are interpreted as natural oscillations of coronal magnetic loops; the dynamical spectra of the pulsations are synthesized for the first time. Three types of low-frequency fluctuations modulating the flare microwave radiation can be distinguished in the observations. First, there are fast and slow magneto-acoustic oscillations with periods of 0.5–0.8 s and 200–280 s, respectively. The fast magneto-acoustic oscillations appear as trains of narrow-band signals with durations of 100–200 s, a positive frequency drift $d\nu/dt = 0.25$ MHz/min, and frequency splitting $\delta\nu = 0.01$–0.05 Hz. Second, there are natural oscillations of the coronal magnetic loops as equivalent electrical circuits. These oscillations have periods of 0.5–10 s and positive or negative frequency drift rates $d\nu/dt = 8 \times 10^{-3}$ Hz/min or $d\nu/dt = -1.3 \times 10^{-2}$ Hz/min, depending on the phase of the radio outburst. Third, there are modulations of the microwave radiation by short periodic pulses with a period of 20 s. The dynamical spectra of the low-frequency pulsations supply important information about the parameters of the magnetic loops: the ratio of the loop radius to its length $r/L \approx 0.1$, the plasma parameter $\beta \approx 10^{-3}$, the ratio of the plasma densities outside and inside the loop $\rho_e/\rho_i \approx 10^{-2}$, and the electrical current flowing along the loop $I \approx 10^{12}$ A. © *2003 MAIK "Nauka/Interperiodica".*

1. INTRODUCTION

Observations of solar and stellar flares in the radio, optical, and X-ray provide numerous examples of pulsating radiation occurring on time scales ranging from milliseconds to tens of seconds and minutes [1–7]. Coronal magnetic loops are frequently sources of solar flares [8]. It has been suggested that the flare microwave radiation of late-type stars may likewise arise in sources resembling coronal magnetic loops [7]. We can consider the coronal magnetic loops to be magnetohydrodynamic (MHD) wave resonators. The MHD oscillations modulate the parameters of the coronal magnetic loop, in particular, the mirror ratio $\sigma = B_{max}/B_{min}$, density of trapped and untrapped particles, etc. This results in a modulation of the radiation with the period of the MHD oscillations.

Along with MHD pulsations, there is another mechanism for the modulation of the observed radiation. The footpoints of coronal magnetic loops are usually located at the junctions of several supergranulation cells. Converging flows of photospheric plasma strengthen the magnetic fields in these junctions. Under the action of the loop magnetic field, the plasma flows generate strong electrical currents (to 10^{11}–10^{12} A), which flow through the corona from one loop footpoint to the other and close in the photosphere. Consequently, we can treat the current-carrying magnetic loop as an equivalent LCR circuit. The natural oscillations of these circuits have periods of several seconds and high quality factors $Q \geq 10^3$, and can also modulate the radiation generated in the magnetic loops [6].

Analysis of quasiperiodic oscillations of the flare radiation provides an effective diagnostic for active regions, since the period, Q-factor, and modulation depth depend on the physical parameters and size of the regions of energy release. Various techniques for analyzing pulsations are available, in particular, Fourier analysis of time profiles [6, 9–11], statistical analysis of the intervals between pulses [12, 13], autocorrelation methods [14], analysis of the dimensions of a strange attractor [15–19], wavelet analysis [18, 19], and methods of symbolic dynamics [19].

1063-7729/03/4710-0873$24.00

Mean parameters of the LF pulses

Frequency interval, Hz	1.2–1.5	1.5–1.8
Number of pulses	20	28
Repetition period, s	287 ± 7	205 ± 6
Pulse duration, s	210 ± 6	110 ± 4
Frequency deviation, Hz	0.32 ± 0.02	0.3 ± 0.016
Frequency drift, Hz/min	$+0.25 \pm 0.01$	$+0.25 \pm 0.01$
Frequency splitting, Hz	0.01–0.05	

The identification of low-frequency (LF) oscillations is the main difficulty in the analysis and interpretation of solar and stellar pulsations, since various MHD waves frequently display approximately the same modulation period. We can remove this ambiguity if we know the dynamical spectra of the pulsations; that is, the dependence of the spectral energy density on the frequency and time. Here, there is a full analogy with the sporadic radio emission of the Sun: as a rule, it is virtually impossible to determine the type of solar radio burst using data on the intensity at a single frequency, but this can easily be done using the dynamical spectrum of the radio burst.

The main objective of the present work is to study the spectral–temporal evolution of LF pulsations modulating the microwave radiation of solar flares. For this purpose, we apply a "sliding window" Fourier analysis (the SWF method) and the nonlinear Wigner–Ville (WV) method [20–22]. These methods enable us to obtain the dynamical spectra of the LF pulsations, which makes possible the identification of MHD oscillations generated in active regions, calculation of their Q-factors, and determination of other parameters important for source diagnostics. The WV method is the most effective for analyses of modulations using quasi-monochromatic signals with time-variable frequencies, and also for high-resolution analyses of frequency–time structures [22]. For these cases, the SWF method is less effective than the WV method, since averaging in the window results in a decrease of the spectral density of components with frequencies that vary within the window. However, the nonlocal character of the WV method becomes important when studying long-term signals [22]. Due to this effect, the intense (or "noisy") portion of the data can be manifest in various regions of the dynamical spectrum, leading to the suppression of comparatively weak components of the signal. Therefore, both methods (WV and SWF) are necessary in order to eliminate possible artifacts and provide high spectral–temporal resolution. Wavelet analysis is effective for studies of pulse trains, although information on low-frequency, quasiperiodic modulations is lost. Note that the SWF method is a standard technique, whereas the WV transform has not been applied in astronomy research previously, although it has been successfully used in geophysics, oceanology, acoustics, and so on.

In Section 2, we analyze the time profiles of several solar microwave bursts and determine the dynamical spectra of the LF modulation of these bursts using the SWF and WV transforms. In Section 3, we compare the results obtained by the different methods and discuss their possible physical interpretation.

2. LOW-FREQUENCY MODULATION OF THE MICROWAVE RADIATION OF SOLAR FLARES

To analyze the LF modulation of the microwave radiation of solar flares, we used digital records of the time profiles of radio bursts at 22 and 37 GHz obtained at the Metsähovi Observatory (Finland). The widths of the antenna beam pattern at these frequencies are $4.0'$ and $2.4'$, respectively. The time resolution was either 0.05 or 0.1, depending on the observational regime. The sensitivity of the receiver was about 0.1 sfu, which corresponds to a resolution of $\sim$100 K in antenna temperature. The digital data on the flux of the microwave bursts were used for a computer analysis of the dynamical spectra of the LF modulation of the radio emission.

We present here results for three time profiles of radio bursts: (1) one observed at 37 GHz during 1244–1446 UT on May 19, 1990 with a time resolution of 0.1 s, (2) a second observed at 37 GHz during 1341–1511 UT on March 24, 1991 with a time resolution 0.05 s, and (2) two more observed at 22 GHz during 0820–1050 UT on August 28, 1990 with a time resolution of 0.1 s. We have identified several types of LF pulsations with frequencies $\nu \lesssim 1$ Hz modulating the microwave radiation. We interpret these pulsations as fast and slow magneto-acoustic waves, i.e., signals with a linear frequency modulation (chirp signals) and periodic pulse trains. Similar LF modulations have been detected in other microwave bursts. In addition, we have detected extremely intense activity at frequencies $\nu \lesssim 0.1$ Hz, which requires a special analysis due to the high noise level in this spectral interval.

2.1. Event of May 19, 1990

Figure 1a depicts the May 19, 1990 burst. The time profile demonstrates a typical shape, with a gradual rise and fall (GRF), with the maximum flux being about 10 sfu. This profile exhibits weak (several

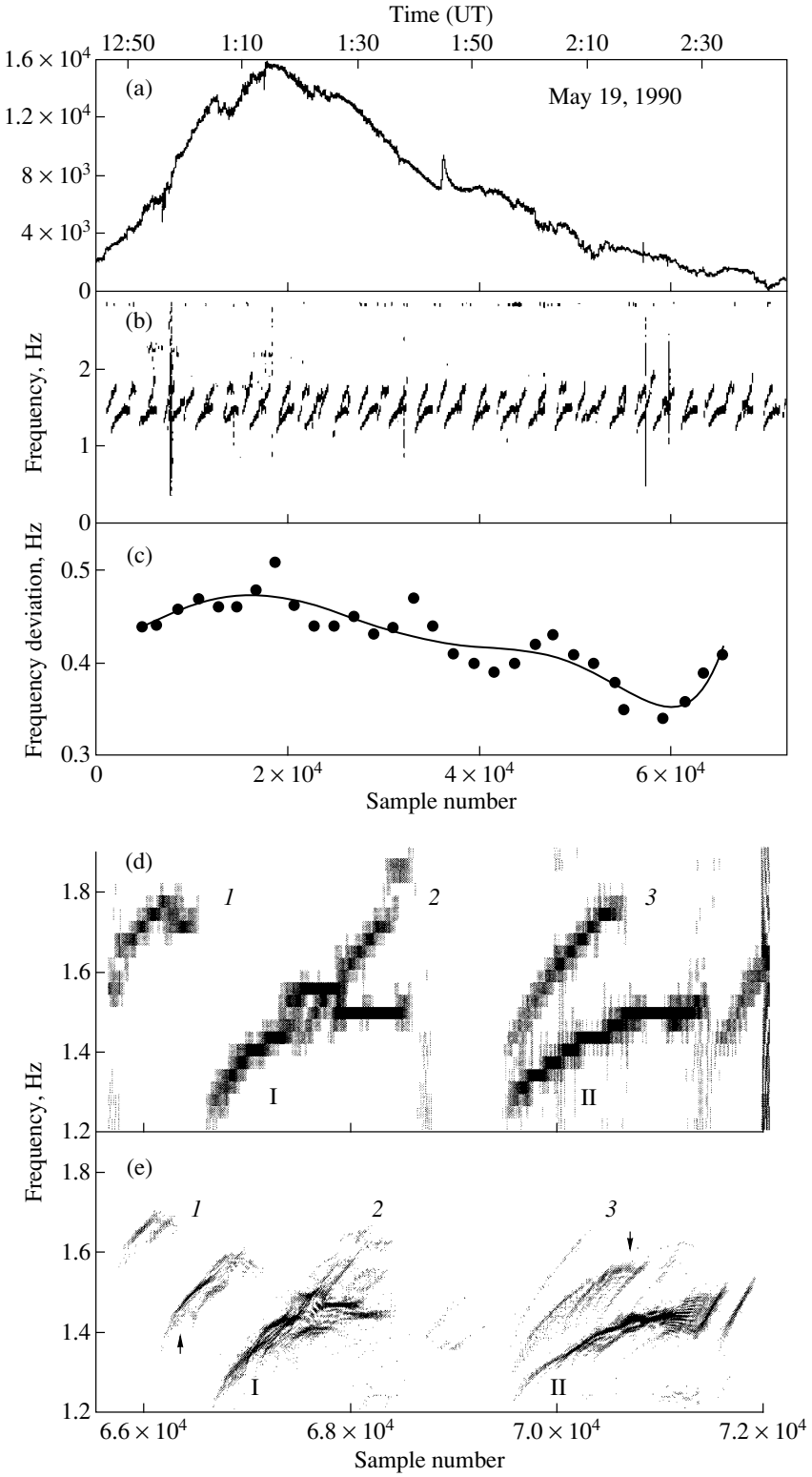

Fig. 1. (a) Microwave burst detected on May 19, 1990 at 1244–1444 UT at 37 GHz. There are weak LF fluctuations of the intensity. (b) Fragment of the dynamical spectrum of the LF fluctuations at 1–2 Hz. There are drifting chirp tracks in two frequency intervals: 1.2–1.5 Hz and 1.5–1.8 Hz. (c) Time dependence of the frequency deviation in the chirp tracks at 1.5–1.8 Hz over the course of the burst. (d) Dynamical spectra of the two chirp signals obtained via the SWF method. The numbers 1–3 denote pulses in the frequency range 1.5–1.8 Hz, while the Roman numerals I–II denote pulses in the range 1.2–1.5 Hz. (e) WV diagram for the same pulses. The frequency–time resolution here is higher, making it possible to distinguish individual features of the pulses and their frequency separation. The arrows mark interference.

percent) amplitude fluctuations with fairly complex time variations. The dynamical spectrum of the LF pulsations obtained via the SWF method is presented in Fig. 1b. This spectrum has the form of a train of frequency-drifting periodic tracks in the interval 1.2–1.8 Hz, which persist during the entire burst (longer than one hour). The tracks of LF pulsations appear in two frequency intervals: 1.2–1.5 Hz and 1.5–1.8 Hz. Figure 1c shows the temporal behavior of the frequency deviations for the tracks in the interval 1.5–1.8 Hz. Figures 1a and 1b demonstrate a clear correlation between the time profiles of the frequency deviations and the microwave intensity. The deviation increases with increasing burst intensity and reaches its maximum at the peak of the radio emission. As the burst intensity decreases, the frequency deviation, on average, demonstrates a similar behavior. This correlation provides evidence for a solar origin of the LF modulation shown in Fig. 1b. Note also that the repetition period of the tracks at 1.2–1.5 Hz is close to the period of the well known 5-min oscillations observed in the radio and optical emission of the Sun. We also studied another GRF event, namely the June 22, 1989 (1257–1442 UT) solar microwave burst at 37 GHz. This burst was also modulated by a train of chirp tracks similar to those presented in Fig. 1b. Their repetition period was likewise about 5 min, and the frequency deviation was correlated with the mean temporal behavior of the burst intensity in the same way.

All the tracks (chirp pulses) in Fig. 1b exhibit a positive frequency drift. The tracks of the lower band (1.2–1.5 Hz) display frequency splitting. This phenomenon is clearly visible in the dynamical spectrum of the individual LF pulses presented in Fig. 1d (SWF method) and Fig. 1e (WV method). Figure 1e also shows a drifting band in the vicinity of the arithmetic mean of the track frequencies presented in Fig. 1d. This band appears due to the nonlinearity of the Wigner–Ville transform, which leads to the appearance of combination frequencies. On the other hand, note the high frequency–time resolution of the WV method, which here exceeds that of the SWF method (i.e., fast Fourier transform) by about an order of magnitude. Consequently, we can see in the WV spectrum frequency splitting of the tracks at 1.2–1.5 Hz that is not resolved in the fast Fourier transform (compare Figs. 1d and 1e). The frequency splitting varies in the range 0.01–0.05 Hz, with an instantaneous LF bandwidth of about 0.01 Hz. The mean parameters of the May 19, 1990 LF pulses are presented in the Table.

We can see in the Table that the repetition period and mean duration of the LF pulses at 1.2–1.5 Hz exceed those at 1.5–1.8 Hz by factors of 1.4 and 2.6, respectively. However, the frequency deviations and drift rates remain the same in both frequency ranges.

2.2. March 24, 1991 Event

Figure 2a presents the time profile of the microwave burst of March 24, 1991 detected at 37 GHz. According to the Metsähovi data, the burst took place in the active region S25W03. There are two intensity peaks with durations of 2–3 min each, followed by a gradual intensity decrease over about 30 min. The maximum flux in the impulsive phase of the burst was 700 sfu.

The dynamical spectrum of the LF pulsations modulating the March 24, 1991 microwave radiation is shown in Fig. 2b. This spectrum was obtained using the SWF method and consists of three components.

(1) A narrow-band signal whose frequency grows linearly from $\sim$0.4 to $\sim$0.45 Hz (a chirp signal). The frequency drift rate is $d\nu/dt = 1.5 \times 10^{-3}$ Hz/min. This type of modulation is observed at the preflare stage of the event.

(2) A high-Q chirp signal at frequencies of 0.5–0.1 Hz with a negative frequency drift rate of $d\nu/dt = -1.3 \times 10^{-2}$ Hz/min, which exceeds the rate in the preflare stage by an order of magnitude. This modulation appears during the impulsive phase of the burst, and disappears when the intensity of the radiation decreases to its preflare level.

(3) A chirp signal with a positive frequency drift $d\nu/dt = 8 \times 10^{-3}$ Hz/min that follows the chirp signal with a negative frequency drift. The Q-factors of the chirp signals are determined in the WV transform and are $Q = f/\Delta f \simeq (0.7–2.5) \times 10^3$.

In the event of March 24, 1991, there was a clear correlation between the appearance of chirp signals with positive or negative frequency drifts and the time profile of the microwave burst. Therefore, we argue that the observed LF modulation has a solar origin with a high probability. Note also that we have detected numerous segments of chirp signals with positive and negative frequency drifts in other microwave bursts observed at Metsähovi at 37 GHz, for example the events of March 23, 1991 (1230 UT), May 7, 1991 (1030 UT), May 11, 1991 (1325 UT), and others. The frequencies of the chirp signals were in the range 0.1–1.5 Hz.

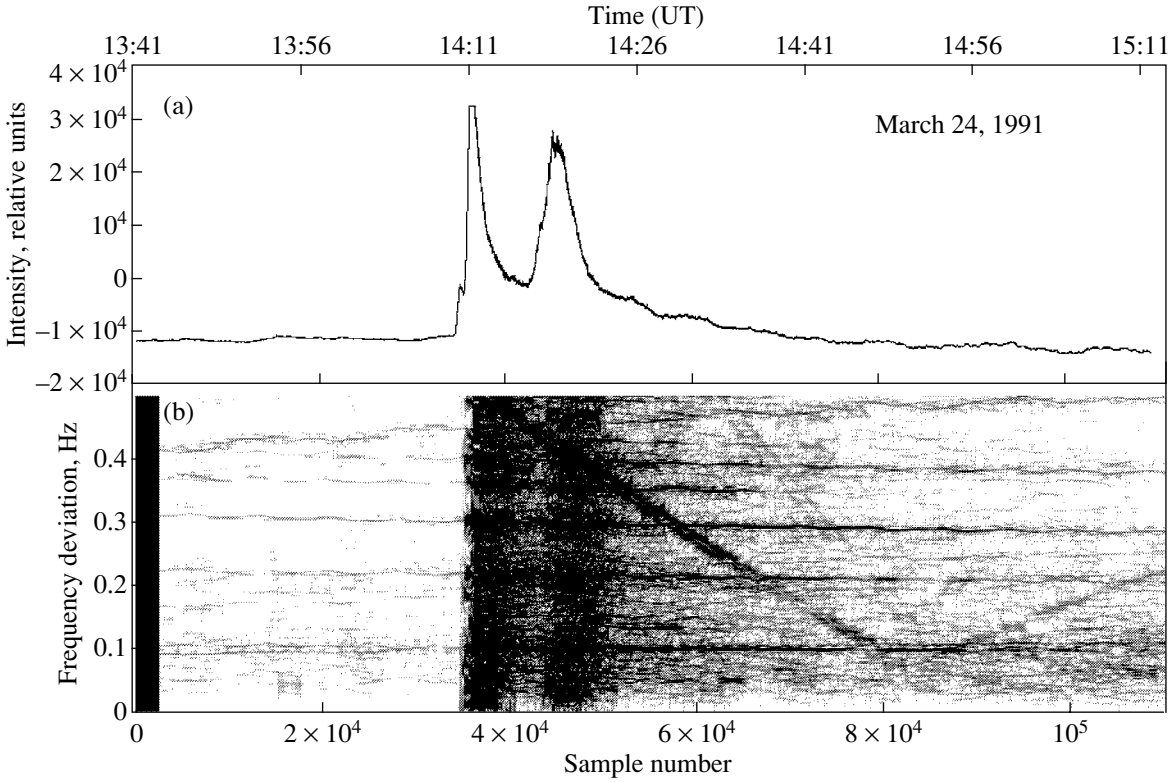

Fig. 2. Microwave burst of March 24, 1991 at 1341–1511 UT: (a) time profile for 37 GHz and (b) fragment of the dynamical spectrum of the LF pulsations obtained using the SWF method. There is a clear chirp signal with a frequency of about 0.4 Hz and a weak positive frequency drift. At the burst maximum, a strong chirp signal with a negative frequency drift, $d\nu/dt = -1.3 \times 10^{-2}$ Hz/min, appears at a frequency of 0.5 Hz. When the intensity falls to its preflare level, this signal is replaced by a chirp signal with a positive frequency drift.

2.3. August 28, 1990 Event

We can see in Fig. 3a that the August 28, 1990 event (37 GHz, 0900–1050 UT) demonstrates two nearly identical bursts with the form of a short impulse (duration about 2 min) followed by a gradual decrease in the radiation over ~40 min. The second burst follows about one hour after the first. Each stage of the decrease in radiation displays appreciable intensity fluctuations during the time intervals 0910–0920, 0940–0950, 1015–1025, and 1040–1050 UT. We used the SWF method for the spectral analysis of these fluctuations. Figure 3b shows the corresponding dynamical spectrum of the LF modulation of the burst intensity. There are segments of equidistant spectral lines parallel to the time axis in the intervals of increased intensity fluctuations indicated above. These spectral lines are associated with the periodic pulse train, with its repetition period being ~20 s, which corresponds to intervals between the spectral lines of $\Delta\nu \simeq 0.05$ Hz in Fig. 3b. The coincidence of the spectral lines with the occurrence of increased fluctuations in the radiation intensity provides evidence for a solar origin of the detected pulse modulation. Here, the modulation is apparently associated with an additional periodic injection of fast particles into the region of radio emission.

3. DISCUSSION

Using the SWF and WV methods, we have obtained dynamical spectra of the LF modulations of the solar flare radiation and detected the following modulations in the frequency 0.1–2.0 Hz.

(1) Chirp pulse trains with durations of 100–200 s and a frequency drift rate of ~0.25 Hz/min that repeat periodically during the entire microwave burst (May 19, 1990 event).

(2) High-Q quasi-monochromatic signals in the range 0.1–0.5 Hz, with gradually increasing or decreasing frequency. The maximum frequency drift rate is $|d\nu/dt| \approx 1.3 \times 10^{-2}$ Hz/min (March 24, 1991 event).

(3) Modulation by a periodic pulse train with a repetition frequency of about 0.05 Hz (August 28, 1990 event).

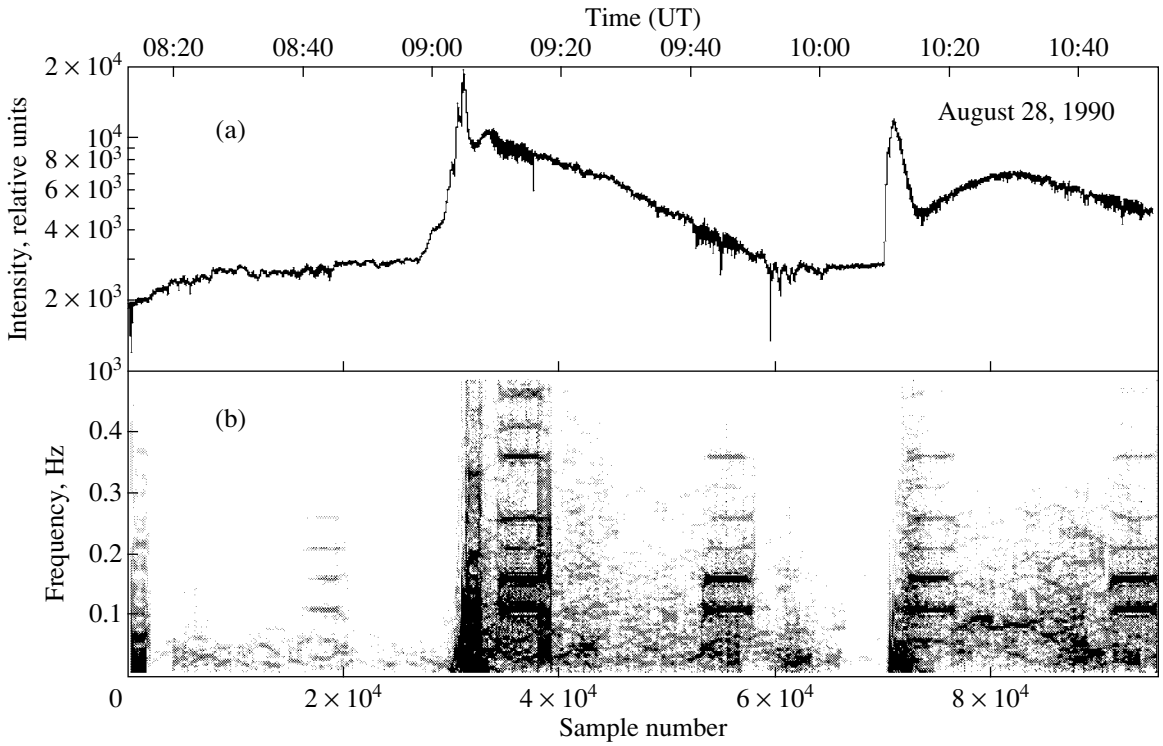

Fig. 3. Microwave burst of August 28, 1990 at 0900–1050 UT: (a) time profile for 22 GHz and (b) dynamical spectrum for the LF pulsations obtained using the SWF method, which takes the form of equidistant bands parallel to the time axis, indicating modulation by periodic pulses. The presence of these bands is clearly correlated with intervals of intense fluctuations in the solar radio emission. The modulation period is 20 s.

3.1. Solar or Terrestrial Origin?

There are terrestrial sources that can modulate solar radio emission or generate pulsed signals similar to those detected in the solar radio emission. These include fluctuations in the tropospheric absorption of radio signals, as well as interference produced by radar stations, broadcasting stations, and communication and satellite systems. In addition, there could also be instrumental sources of noise, such as penetrating signals from local generators and modulation of the received signal by vibrations in the antenna-drive mechanisms.

The properties of the observed LF modulation (the regular frequency drift, frequency splitting, periodic pulse trains) indicate that the modulation cannot be due to the effect of fluctuations in the atmospheric absorption. Otherwise, this would contradict the well-known data on fluctuations of the atmospheric radio emission at millimeter wavelengths (see [25, 26]).

The Metsähovi Observatory carries out continuous monitoring of "parasite" signals. The most significant interference is due to mobile phone stations, although their frequencies, 900 and 1800 MHz, are far from the 22 and 37 GHz observing frequencies. In Finland, there are also communication systems that use 8 mm signals; however, these systems have low power and are not directed toward the observatory. The penetration of signals from local generators (oscillators and generators in the controlling systems, etc.) is improbable, since every electronic device is carefully tested before and after mounting it in the tower of the radio telescope. Such complex behavior of the antenna vibrations, resulting in the appearance of various chirp signals during tracking of the Sun, likewise seems improbable. We have detected a number of quasiperiodic signals with constant frequencies in the burst data that could be due to instrumental effects. We have not considered these signals in our interpretation of the solar observations.

We can summarize the arguments in favor of a solar origin for the observed LF modulation of the solar radio emission as follows.

(1) ***May 19, 1990 event***. Each individual pulse in Fig. 1b displays appreciable differences in its shape, duration, mean frequency, and frequency drift rate. This makes a man-made origin doubtful. In addition, as we indicated above, there is a clear correlation between the pulse-frequency deviation and solar-burst intensity. Similar behavior was observed in studies of the radio burst of June 22, 1989, with the individual chirp pulses also demonstrating individual features. Finally, we note the coincidence of the pulse-

repetition periods with the well-known 5 min period of the photospheric oscillations.

(2) ***March 24, 1991 event***. The LF modulation presented in Fig. 2b could, in principle, be due to corresponding regular vibrations of the radio telescope during tracking of the solar active region. However, both the sign and magnitude of the frequency drift rate display an obvious correlation with the time profile of the microwave burst intensity and do not correlate with any properties of the antenna position (passage through the solar culmination, etc.).

(3) ***August 28, 1990 event***. The characteristic features of the dynamical spectrum of the LF pulsations (the equidistant lines in Fig. 3b) appear during periods of increased fluctuations in the intensity of the microwave radiation. Similar behavior was noted during analysis of an event on September 1, 1990 event in the same active region that was involved in the August 28, 1990 event, although the pulse period was somewhat shorter, $\sim$18 s. If these pulses were radar or communication noise, they would also appear in recordings without any solar signals, and their period would likely be constant.

All these arguments support our conclusion that the LF modulation for which dynamical spectra are presented in Figs. 1b, 1d, 1e, 2b, and 3b has a solar origin.

It was noted above that we observed a regular infra-low-frequency modulation at $\nu \lesssim 0.1$ Hz. To eliminate the influence of these "zero frequencies" on the dynamical spectra obtained using the WV method, a technique for filtering out these frequencies, as well as strong interference impulses, has been proposed [27]. Nevertheless, the frequency range $\nu \lesssim 0.1$ Hz is of particular interest and requires a special analysis, since it can potentially supply us with useful information about certain new forms of LF modulation.

We suggest that MHD vibrations of the coronal magnetic loops that are the sources of the microwave radiation could represent one source of the modulation of the solar-flare microwave radiation observed at 0.1–2.0 Hz. The high Q-factors of the order of 200–4×10^3 observed for the LF pulsations support this hypothesis. This would be quite natural for coronal magnetic loops, which are, as is shown below, high-Q MHD resonators.

3.2. Eigenmodes of Coronal Magnetic Loops

To first approximation, we can analyze the natural oscillations of coronal magnetic loops by modeling the loop as a homogeneous plasma cylinder of length L and radius r whose ends are fixed, reflecting the freezing in of the footpoints of the magnetic loop. The approximation of a homogeneous plasma cylinder is applicable when the height of the magnetic loop is lower than the characteristic scale height of the solar atmosphere. As a rule, this approximation is valid for magnetic flare loops.

Let us assume that the plasma density inside the loop is ρ_i, the temperature is T_i, and the magnetic field B_i is directed along the cylinder axis. We denote the plasma parameters outside the cylinder as ρ_e, T_e, and B_e. For the simple case of a thin ($r/L \ll 1$), dense ($\rho_\mathrm{e}/\rho_\mathrm{i} \ll 1$), axially symmetric cylinder, fast and slow magneto-acoustic waves can be excited, with the frequencies (see, for example, [28])

$$\omega_+ = (k_\perp^2 + k_{||}^2)^{1/2}(c_\mathrm{si}^2 + c_\mathrm{Ai}^2)^{1/2}, \qquad (1)$$

$$\omega_- = \frac{k_{||} c_\mathrm{si} c_\mathrm{Ai}}{(c_\mathrm{si}^2 + c_\mathrm{Ai}^2)^{1/2}}. \qquad (2)$$

Here, $k_\perp = \lambda_\mathrm{i}/r$ is the transverse wave number, where λ_i are the roots of the equation $J_0(\lambda_\mathrm{i}) = 0$ (J_0 is the Bessel function); $k_{||} = s\pi/L$ ($s = 1, 2, 3, \ldots$) is the longitudinal wave number obtained from the freezing-in condition for the ends of the cylinder; $c_\mathrm{s} = (\gamma p/\rho)^{1/2}$ is the speed of sound, where p is the plasma pressure and γ is the ratio of specific heats; and $c_\mathrm{A} = B/\sqrt{4\pi\rho}$ is the Alfven speed.

The fast magneto-acoustic (FMA) wave can experience strong attenuation due to radiation of the FMA waves into the plasma surrounding the cylinder. The rate of this radiative damping is given by the formula [29]

$$\gamma_+ = \frac{\pi}{2}\omega_+ \left(\frac{\rho_\mathrm{e}}{\rho_\mathrm{i}} - \frac{k_{||}^2}{k_\perp^2}\right), \quad \frac{\rho_\mathrm{e}}{\rho_\mathrm{i}} > \frac{k_{||}^2}{k_\perp^2}. \qquad (3)$$

However, when the plasma inside the cylinder is sufficiently dense ($\rho_\mathrm{e}/\rho_\mathrm{i} < k_{||}^2/k_\perp^2$), there is no radiative damping. In this case, there is total reflection (the FMA waves become "trapped"), and the cylinder becomes an "ideal" FMA resonator.

In addition to the fast and slow magneto-acoustic waves, there can be Alfven waves in the cylinder, with their frequency being

$$\omega_\mathrm{A} = k_{||} c_\mathrm{Ai}, \qquad (4)$$

as well as a kink mode (kink waves) with the frequency

$$\omega_k = k_{||}\left(\frac{\rho_\mathrm{i} c_\mathrm{Ai}^2 + \rho_\mathrm{e} c_\mathrm{Ae}^2}{\rho_\mathrm{i} + \rho_\mathrm{e}}\right)^{1/2}. \qquad (5)$$

Finally, a coronal magnetic loop carrying a current is an equivalent electrical circuit with the natural

oscillation frequency [6, 23]

$$\omega_{\rm LCR} = \frac{\sqrt{2}}{\left(\ln\frac{8L}{\pi r} - \frac{7}{4}\right)^{1/2}} \frac{I_0}{\sqrt{4\pi\rho_{\rm i}} c r^2}, \qquad (6)$$

where I_0 is the mean electrical current flowing through the cross section of the magnetic loop, which is determined by the balance between the electrical losses in the circuit and the power of the photospheric electromotive force associated with the photospheric convection that is applied to the loop footpoints. The frequency $\omega_{\rm LCR}$ increases with time if the energy of the electrical current is accumulated in the loop, and decreases when this energy is dissipated (for example, during a flare). We can see that $\omega_{\rm LCR}$ is of the same order as the frequency ω_+ of the FMA vibrations.

3.3. Data Analysis

To identify the LF pulsations observed in the microwave bursts, we adopt the following mean parameters for the flare magnetic loops [8]: plasma number density inside the loop $n \approx (1{-}5) \times 10^{10}$ cm^{-3}, temperature $T \approx 5 \times 10^6$ K, magnetic field $B \approx 100{-}500$ G, loop length $L \simeq 5 \times 10^9$ cm, and loop radius $r \approx 2 \times 10^8$ cm. We then obtain the following periods for the LF pulsations: for fast magneto-acoustic waves, $T_+ = \omega_+/2\pi \simeq 2.6 r/c_{\rm Ai} \approx 1{-}10$ s; for LCR oscillations, $T_{LCR} = 2\pi/\omega_{\rm LCR} \simeq T_+ \approx 1{-}10$ s; for Alfven and kink modes, $T_{\rm A} \simeq T_{\rm k} \simeq 2L/c_{\rm Ai} \approx 20{-}100$ s; and for slow magneto-acoustic waves, $T_- = 2\pi/\omega_- \simeq 2L/c_{\rm si} \approx 270$ s. Comparing these values with the observed dynamical spectra of the LF pulsations, we can draw the following conclusions.

For the **May 19, 1990 event**, the observed LF pulsations with periods 0.5–0.8 s and Q-factors of the order of 10^2 are in the best consistency with the fast magneto-acoustic pulsations of the coronal magnetic loop. The Q-factor of the LCR mode with similar periods is much higher ($Q = 10^3{-}10^4$), and this mode is not likely to be associated with the observed modulation. The excitation of FMA oscillations simultaneously in the two frequency intervals 1.2–1.5 Hz and 1.5–1.8 Hz implies that the flare process occurs in two coupled loops with nearly identical parameters. The periodic repetition of the FMA trains every 287 and 205 s in the first and second frequency intervals, respectively, could be associated with slow magneto-acoustic waves that are generated simultaneously with the FMA oscillations and modulate the loop parameters. The Alfven and kink modes have considerably shorter periods (20–100 s) and are therefore less likely to contribute to the periodic repetition of the FMA trains than are slow magneto-acoustic waves.

We explain the observed frequency splitting in the FMA oscillations by the excitation of FMA waves with two wave numbers: $k_{||} = \pi/L$ and $k_{||} = 2\pi/L$. It follows from Eq. (1) for the FMA frequency that the frequency splitting is determined by the ratio of the loop radius to its length,

$$\frac{\delta\omega_+}{\omega_+} = \frac{3}{2}\left(\frac{\pi}{2.4}\right)^2\left(\frac{r}{L}\right)^2. \qquad (7)$$

For an average frequency splitting of $\delta\nu_+ = \delta\omega_+/2\pi \simeq 0.025$ Hz, (7) yields $r/L \simeq 0.08$ for the frequency interval 1.2–1.5 Hz; that is, the coronal magnetic loop turns out to be fairly thin.

We can obtain important information about the ratio of the gas to the magnetic pressure in the loop, $\beta = 8\pi n_{\rm i} k_{\rm B} T_{\rm i}/B_{\rm i}^2$ (where $k_{\rm B}$ is the Boltzmann constant), from the ratio of the frequencies of the slow and fast magneto-acoustic waves, (1) and (2):

$$\frac{\omega_-}{\omega_+} = \frac{\pi}{2,4}\sqrt{\frac{5}{3}}\frac{r}{L}\beta^{1/2}. \qquad (8)$$

We obtain from Eq. (8) $\beta \simeq 0.4 \times 10^{-3}$ for the frequency interval 1.2–1.5 Hz in Fig. 1e. In this case, β is fairly small, corresponding to a relatively strong magnetic field during the May 19, 1990 event.

Finally, the absence of appreciable attenuation of the FMA oscillations during the microwave burst provides a limit for the ratio of the external to the internal plasma density [see Eq. (3) for the FMA damping]:

$$\frac{\rho_{\rm e}}{\rho_{\rm i}} < \frac{k_{||}^2}{k_\perp^2} = \left(\frac{\pi}{2,4}\frac{r}{L}\right)^2. \qquad (9)$$

Equation (9) yields $\rho_{\rm e}/\rho_{\rm i} \lesssim 1.1 \times 10^{-2}$ for the frequency range 1.2–1.5 Hz of the dynamical spectrum in Fig. 1b. This means that the plasma inside the magnetic loop is much denser than the plasma outside the loop. This conclusion is in good agreement with the common hypothesis that the magnetic loops contain a significant portion of the total coronal material. Thus, the dynamical spectrum of the LF pulsations of the May 19, 1990 event enables us to draw important conclusions on the parameters of the magnetic flare loops.

In the **March 24, 1991 event**, we have probably observed for the first time natural oscillations of a current-carrying magnetic loop as an equivalent electrical circuit (predicted earlier in [6]). These oscillations have the frequencies $\sim (1{-}10)$ Hz and high $Q \simeq 10^3$-factors, and exhibit a slow increase in their frequency before the flare and a decrease in their frequency during the flare. The increase in the electrical current and accumulation of nonpotential magnetic field energy inside the loop before the flare, followed by the dissipation of current energy during the flare, can provide a natural explanation for this behavior.

Equation (6) enables us to calculate the electrical current in the loop. Assuming $n \simeq 5 \times 10^{10}$ cm^{-3} and $r \simeq 2 \times 10^8$ cm, we find from (6) that $T_{\rm LCR} \simeq 30/I_{11}$ s, where $I_{11} = 10^{-11} I_0$ A. In the March 24, 1991 event, $T_{\rm LCR} \simeq 2.5$–10 s; therefore, we obtain an electric current $I_0 \simeq 3 \times (10^{11}$–$10^{12})$ A. Solar magnetograms [30] show that the electrical currents in active regions at photospheric levels can be 10^{11}–10^{12} A.

The March 24, 1991 event shows that the electrical current decreases by a factor of five during the flare. This means that a considerable portion of the energy accumulated in the electrical circuit ($\mathcal{E} = \tilde{L} I_0^2 / 2c^2 \simeq 10^{31}$ erg, where $\tilde{L}$ is the circuit inductance) is dissipated during the flare.

The **August 28, 1990 event** shows modulation of the microwave radiation by a periodic pulse train with a repetition period of about 20 s. A periodic acceleration of electrons, with the period being determined by the LCR period of the loop, can take place during this event. Fast electrons in the coronal magnetic loop can generate microwave radiation via the gyrosynchrotron mechanism. The large-scale electric fields generated at the footpoints of the loop and modulated by the LCR oscillations can provide the origin of the acceleration [31].

4. CONCLUSIONS

(1) By applying the SWF and WV methods in a frequency–time analysis of low-frequency modulations of the microwave radiation of solar flares, we have obtained the dynamical spectra of these modulations and identified these spectra with natural oscillations of coronal magnetic loops acting as MHD resonators.

(2) The dynamical spectra demonstrate the presence of fast and slow magneto-acoustic waves with periods 0.5–0.8 s and 200–280 s that are excited in the magnetic loops during the flares. In addition, there are natural oscillations of the magnetic loop as an equivalent electrical circuit. These oscillations have periods of 2–10 s. We have also observed modulation of the microwave radiation by a periodic train of short pulses with a repetition period of ~20 s. These pulses could result from the periodic acceleration of particles during the solar flare.

(3) The dynamical spectra supply us with important information about the physical parameters of the magnetic flare loops. For the May 19, 1990 event, we have estimated the ratio of the loop radius to its length $r/L \simeq 0.1$, the ratio of the external to the internal plasma densities $\rho_{\rm e}/\rho_{\rm i} \lesssim 10^{-2}$, the plasma parameter $\beta \simeq 10^{-3}$, and the electrical current $I_0 \approx 10^{12}$ A.

ACKNOWLEDGMENTS

The authors are grateful to Yu.P. Lebedev for creating the first version of a computer program for the Wigner–Ville pulsation analysis. We are also grateful to V.E. Shaposhnikov for his assistance and helpful discussions. This work was supported by a collaboration agreement between the Russian and Finnish Academies of Sciences, by the Russian Foundation for Basic Research (project codes 01-02-16435, 02-02-16239, 00-1596674, and 02-02-04005), and CRDF project no. RPO-841. The authors also acknowledge the support of the State Science and Technology Program "Astronomy," the Program of the Presidium of the Russian Academy of Sciences "Nonstationary Phenomena in Astronomy" and the Program of support for leading scientific scools.

REFERENCES

1. M. P. Haghes and R. L. Harkness, Astrophys. J. **138**, 239 (1963).
2. H. F. van Beek, L. D. de Feiter, and C. de Jager, Space Res. **14**, 447 (1974).
3. C. Slottje, Nature **275**, 520 (1978).
4. D. J. Mullan, R. B. Herr, and S. Bhattachayya, Astrophys. J. **391**, 265 (1992).
5. T. S. Bastian, J. Bookbinder, G. Dulk, and M. Davis, Astrophys. J. **353**, 265 (1990).
6. V. V. Zaitsev, A. V. Stepanov, S. Urpo, and S. Pohjolainen, Astron. Astrophys. **337**, 887 (1998).
7. A. V. Stepanov, B. Kliem, V. V. Zaitsev, *et al.*, Astron. Astrophys. **374**, 1072 (2001).
8. R. J. Bray, L. E. Gram, C. J. Durrant, and R. E. Longhhead, *Plasma Loops in the Solar Corona* (Cambridge Univ. Press, Cambrige, 1991).
9. E. W. Cliver, M. D. Hurst, F. L. Welfer, and M. P. Bleiweiss, Solar Phys. **48**, 307 (1976).
10. A. Mongeney and M. Pick, Astron. Astrophys. **224**, 242 (1989).
11. R. Y. Zhao, A. Mongeney, and M. Pick, Astron. Astrophys. **241**, 183 (1991).
12. G. Trottets, A. Kerdraon, A. O. Benz, and R. Treumann, Astron. Astrophys. **93**, 129 (1981).
13. M. J. Aschwanden, A. O. Benz, and M. Montello, Astrophys. J. **431**, 432 (1994).
14. M. J. Aschwanden, A. O. Benz, B. R. Dennis, and M. R. Kundu, Astrophys. J., Suppl. Ser. **90**, 631 (1994).
15. J. Kurths and M. Karlicky, Solar Phys. **119**, 399 (1989).
16. J. Kurths, A. O. Benz, and M. J. Aschwanden, Astron. Astrophys. **248**, 270 (1991).
17. H. Isliker and A. O. Bentz, Astron. Astrophys. **285**, 663 (1994).
18. J. Kurths, U. Schwarz, and A. Witt, *Coronal Magnetic Energy Releases* (Springer, Berlin, 1995); Lect. Notes Phys. **444**, 159 (1995).

19. U. Schwarz, J. Kurths, B. Kliem, *et al.*, Astrophys. J., Suppl. Ser. **127**, 309 (1998).
20. E. P. Wigner, Phys. Rev. **40**, 749 (1932).
21. J. Ville, Cables Transm. **2A**, 61 (1948).
22. L. Cohen, Proc. IEEE **77**, 72 (1989).
23. V. V. Zaitsev, A. G. Kislyakov, A. V. Stepanov, *et al.*, Izv. Vyssh. Uchebn. Zaved., Ser. Radiofiz. **44**, 38 (2001).
24. V. V. Zaitsev, A. G. Kislyakov, S. Urpo, and E. I. Shkelev, Izv. Vyssh. Uchebn. Zaved., Ser. Radiofiz. **44**, 756 (2001b).
25. A. G. Kislyakov, V. I. Nosov, and L. I. Tsvetkov, Kinemat. Fiz. Neb. Tel **6**, 36 (1990).
26. I. I. Zinchenko and A. G. Kislyakov, in *Proceedings of I All-Union School-Symposium on Millimeter Wave Propagation in the Atmosphere* [in Russian] (Nauka, Moscow, 1983), p. 310.
27. E. I. Shkelev, A. G. Kislyakov, and S. Yu. Lupov, Izv. Vyssh. Uchebn. Zaved., Ser. Radiofiz. **45**, 433 (2002).
28. V. V. Zaitsev and A. V. Stepanov, Issled. Geomagn. Aeronom. Fiz. Solntsa **37**, 3 (1975).
29. B. G. Meerson, P. V. Sasorov, and A. V. Stepanov, Solar Phys. **558**, 165 (1978).
30. A. B. Severny, Space Sci. Rev. **3**, 451 (1965).
31. V. V. Zaitsev, in *Proceedings of VII Russian-Finnish Symposium on Radioastronomy* (St. Peterburg, 1999), p. 59.

Translated by V. Badin

Astronomy Reports, Vol. 47, No. 10, 2003, pp. 883–887. Translated from Astronomicheskiĭ Zhurnal, Vol. 80, No. 10, 2003, pp. 956–960.

Measuring the Position of the Polarization Plane of Solar Coronal Emission during Eclipse Observations

M. M. Molodensky, V. L. Merzlyakov, and L. I. Starkova

Institute of Terrestrial Magnetism, Ionosphere, and Radiowave Propagation, Russian Academy of Sciences, Troitsk, Moscow oblast, 142190 Russia

Received September 15, 2002; in final form, May 8, 2003

Abstract—We analyze the suitability of digital equipment with CCD arrays for polarization measurements of solar coronal emission during eclipses. The effect of errors in the method on the derived plane of polarization is estimated. In principle, precise measurements of the plane of polarization can be used to determine the amplitude and direction of the current of a heliospheric plasma sheet. The errors in ordinary nondigital photometric measurements (5%) are too large to enable the resolution of a number of problems having to do with the three-dimensional structure of the solar corona. © *2003 MAIK "Nauka/Interperiodica"*.

1. INTRODUCTION

The first studies of the plane of polarization of solar corona emission were initiated in 1971 by Koutchmy and Schatten [1], who detected considerable deviations of the plane of polarization (the direction of predominant oscillations of the electric vector) from the direction tangent to the limb. It was initially believed that this effect could not be explained, since it had been reliably established that the emission of the K corona is due to Thomson scattering of photospheric photons by free coronal electrons. Later, in 1973, Molodensky [2] demonstrated that the scattering of photons by moving electrons results in a rotation of the polarization plane (due to the aberration of light in the coordinate system comoving with the electron flux). In principle, this effect can be used to measure the velocity of the electrons that are the main carriers of the electric current in the plasma. Since the velocity of the ions can be determined very accurately from the Doppler shifts of spectral lines, the deviation of the polarization plane is a valuable source of information about the difference between these two velocities, i.e., about the coronal current density. With this aim in view, new measurements of the plane of polarization were carried out in [3, 4]. The most important conclusion of these works is that the polarization deviations are below 1° in the inner corona at $r < 1.5R_\odot$, which is comparable to the measurement errors.

Pak *et al.* [5] measured deviations of the plane of polarization during the eclipse of September 11, 1999, taking into account observational experience accumulated by that time: a Lyot coronograph scheme with a polaroid installed in the pupil ($D = 9$ mm) was implemented, and red filters were used to exclude the background sky. They obtained an image of the corona in which the deviations of the plane of polarization display fine structure with sizes up to 30″ and deviation angles of 3°–5° [5].

Let us estimate the electric current that can be derived from the deviation of the polarization plane in the corona. As was shown by Molodensky [2], this deviation is $\delta = v_t/c$, where v_t is the velocity component tangential to the limb. If the ions do not participate in the motion, the current density formed by the electron motion is

$$j_t = nev_t. \tag{1}$$

Note that this is the estimated maximum current, since the ion motion decreases the current (so that $j_t = 0$ if the whole plasma moves).

According to Koutchmy *et al.* [4], the accuracy of measurements of deviations of the polarization plane can reach 0.5°. Therefore, let us take $\delta = 10^{-2}$ and assume that $n = 10^6$ cm^{-3} in the outer corona at $h > 0.5R_\odot$. As a result, we obtain

$$j_t = 10^5 \mathrm{CGS} = 3 \times 10^{-5}\ \mathrm{A/cm^2}.$$

If the diameter of the current cross section is 10^8–10^9 cm, the total current should be

$$j_t S = 3(10^{11} - 10^{13})\ \mathrm{A}. \tag{2}$$

This is just the value that is typical for flares of class 2–3 V.

The total current in a heliospheric sheet is of the same order of magnitude. At a distance of $r = 10R_\odot$, the magnetic field of the heliospheric sheet is $B = 1$ G. Consequently, $J = 3 \times 10^{12}$ A. The corresponding value of δ should increase. In the case under consideration, $\delta \sim 1$ rad, which is easily

1063-7729/03/4710-0883$24.00

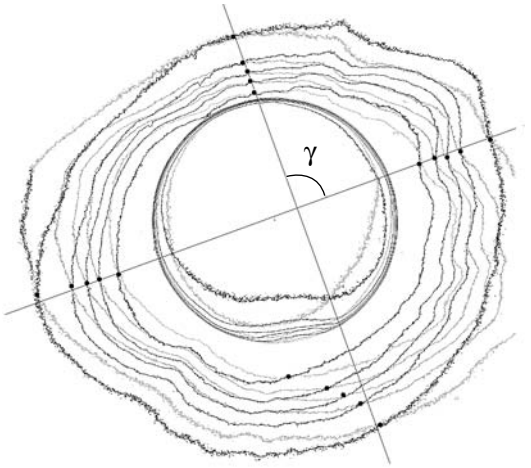

Fig. 1. Set of polarization isophotes for the 1973 eclipse (data of S. Koutchmy).

measurable if there is no influence from the Earth's atmosphere.

In addition, note the following characteristic features.

(1) The current of the heliospheric sheet is perpendicular to the solar surface, so that the total velocity $\mathbf{v} = \mathbf{v}_t$ leads to the deviation of the polarization plane.

(2) The sign of the deviation δ determines the sign of the current j_φ. Therefore, measurements of δ enable us to distinguish between configurations of the field. The model of Pneuman and Kopp [6] describes a heliospheric-sheet configuration whose current j has the same direction as the current of the initial dipole. The corresponding magnetic-field configuration is an acute-angle structure directed from the solar center. On the other hand, as was noted by Koutchmy [7], the Lorentz force in this case is directed toward the solar center, so that, instead of "stretching" the height scale kT/mg, the Lorentz force increases the effective value of g, and the corresponding height scale decreases. The characteristic scales of the main coronal structures (helmets) exceed this value. Consequently, the sign of the heliospheric-sheet current is opposite to the sign of the initial dipole current [8].

Extra-atmospheric observations of the polarization at $r \leq 30R_\odot$ (for example, by LASCO-2 on the SOHO satellite) are quite promising for studies of heliospheric plasma sheets.

We should also note that the appreciably greater deviations observed in the outer corona cannot be interpreted in this way. This would lead to currents that are two to three orders of magnitude greater than those obtained above.

The nature of these deviations is completely different: they are due to the effect of the Earth's atmosphere. Therefore, it is important to study the ring glow observed during eclipses. Having in mind the extra-atmospheric coronal studies carried out SOHO and other satellites, we present discussions of the role of such studies for determining the polarization in the far corona $r \sim 10{-}20R_\odot$, which is of fundamental importance.

2. POLARIZATION ISOPHOTES

Let I_0 and I_p be the intensities of the unpolarized and polarized radiation, respectively, θ the angle between the direction tangent to the limb and the direction of transmission of the polaroid, and $\delta(r,\theta)$ the deviation of the polarization plane from the tangential direction. The intensity of the radiation transmitted by a polaroid oriented at an angle φ to a given direction is

$$I_\varphi(r,\theta) = \frac{1}{2}I_0(r,\theta) + I_p(r,\theta)\cos^2(\theta+\delta-\varphi). \quad (3)$$

The isophotes obtained by rotating the polaroid are described as

$$I_{\varphi_i} = C_i,$$

where φ_i is polaroid position i. If we consider two positions, we obtain two isophote equations:

$$I_0 + I_p + I_p\cos 2(\theta+\delta-\varphi_i) = 2C, \quad (4)$$
$$I_0 + I_p + I_p\cos 2(\theta+\delta-\varphi_k) = 2C.$$

For any fixed C, relations (4) can be treated as a system of equations specifying the points of intersection of the corresponding polarization isophotes. As follows from (4) with $I_p \neq 0$,

$$\cos 2[\theta+\delta-\varphi_i] = \cos 2[\theta+\delta-\varphi_k] \quad (5)$$

or

$$\theta = -\delta + \frac{1}{2}(\varphi_i+\varphi_k) + n\frac{\pi}{2}, \quad n = 0,1,2,3. \quad (6)$$

As follows from (6) with $\delta \equiv 0$, one of the directions, specified by θ at $n = 0$, coincides with the bisectrix of the angle between φ_i and φ_k. There are four such directions, each separated from the neighboring ones by $\pm\pi/2$. This is true of the case

$$\delta(r,\theta) \equiv 0 \quad (7)$$

and does not depend on I_0 and I_p. This is the main advantage of using isophotes [3].

This property of the polarization isophotes was chosen as the basis for checking the influence of the CCD arrays on the polarization.

In particular, a large amount of observational data on the white-light corona were obtained by Koutchmy using a film-recording polarimeter during the eclipse of June 30, 1973 in Mossoro (Chad, Africa). This equipment was successfully used for the first time during an eclipse in 1972 [3]. As many as 350 frames

were recorded on 35-mm color film, with a polaroid being rotated 3° between frames. Accordingly, the orientation of the polaroid was changed by 90° between the first and thirtieth frames. The intersections for frames 1 and 27 are presented in Fig. 1. We can see that the angle γ is close to 90°. We consider this to be the best available method for the analysis and verification of a large amount of data obtained using a film-recording polarimeter.

Figure 1 shows that the deviations of the polarization plane are localized to the place where the inner corona is illuminated. The lunar disk is also illuminated in this same place. Since the brightness of the corona varies by several orders of magnitude, it is quite a challenging problem to exclude such illumination. Pak *et al.* [5] were apparently the first to use a Lyot diaphragm to suppress the bright glow near the limb during measurements of the polarization in the outer corona.

3. ESTIMATES OF THE MEASUREMENT ACCURACY

The accuracy of the measurements is important in a number of studies of structure. This is true not only for eclipse observations, but also for measurements by the LASCO 1–3 satellites. For example, typical photometric errors, $\sim 5\%$, are too large to enable unambiguous localization of polar plumes; this can be done only using more accurate measurements.

The digital cameras that are now in use do not require a photographic process, providing hope that they will enable the solution of certain old problems. The most important question is the sensitivity of the CCD arrays to polarization (standard film does not display such sensitivity). The aim of the measurements described below is to study a modern digital camera from the viewpoint of its applicability to polarization measurements (in particular, the solar corona).

Our receiver is described in [9], and the polarized radiation was formed in the following way. A parabolic mirror fabricated from a dielectric with refractive index $n \sim 1.5$ reflects the light from a point source located at its focus. The equation describing the mirror surface is (Fig. 2)

$$z = r^2, \qquad \mathbf{r} = \mathbf{i}x + \mathbf{j}y, \tag{8}$$

so that the light reflected from the surface is linearly polarized, with the direction of oscillations of the electric vector being perpendicular to $\mathbf{r}$. Reflection from the mirror surface (8) occurs at various angles. As $r \to 0$, the angle of incidence $\theta_i \to 0$ (and the angle of reflection is θ_r), and the degree of polarization $P \to 0$. When $\theta_i \sim 56°$, $\tan\theta_i = n$ ($r = r_{\max}$) and $P \to 1$. Further, as $\theta_i \to \pi/2$, the degree of polarization again decreases, so that $P = 0$ as $\theta_i = \pi/2$. This is quite close to the pattern of polarization observed for the solar corona, in terms of the position angle of the plane of polarization, the presence of a local maximum ($P \to 1$ at $r \to r_{\max}$), and the decrease in polarization at $r > r_{\max}$ and $r < r_{\max}$.

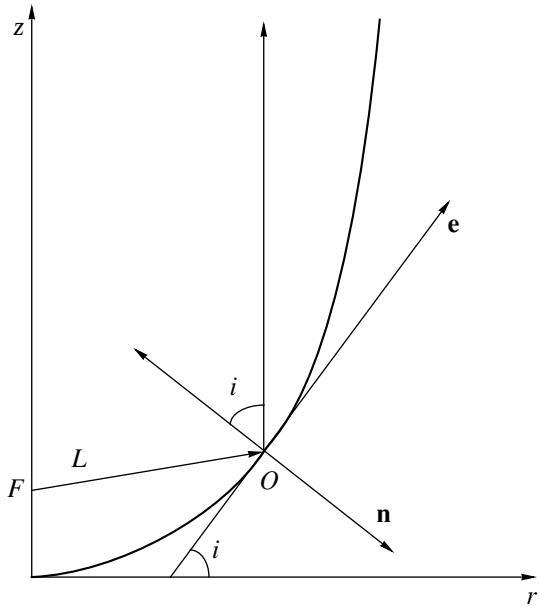

Fig. 2. Sketch of a reflecting surface in a section containing its symmetry axis. The reflecting surface is a parabola with its focus at point F, where a light source is located. A ray arrives at point O at the angle i.

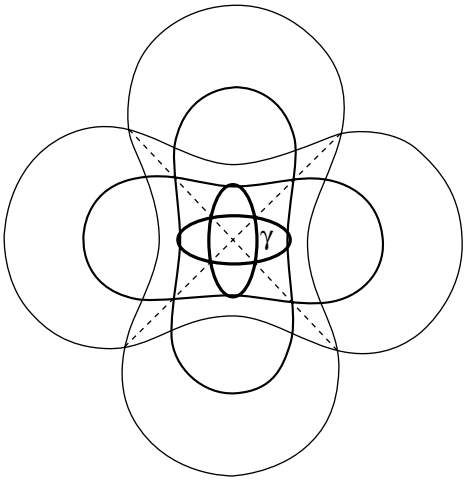

Fig. 3. Polarization isophotes calculated using (13) and (14) at an intersection forming the angle $\gamma = 90°$.

As is shown in Fig. 2, the light ray L leaving the focus F arrives at the surface $z = r^2$ at the point O. Next, after reflection from the surface, it propagates parallel to the z axis. The unit normal vector at O is designated $\mathbf{n}$. The angle between the tangent line and

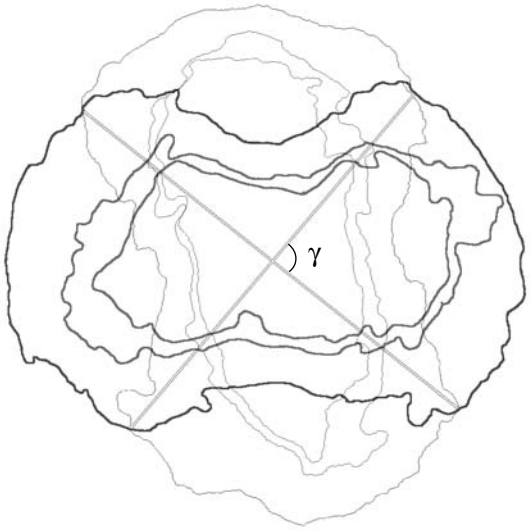

Fig. 4. Intersection of isophotes for a mirror fabricated from a dielectric (with index of refraction $n \sim 1.5$) obtained using a telescope and a digital Nikon Coolpix 850 camera.

the z axis is obviously

$$i = \arctan 2r, \tag{9}$$

while the unit tangent vector is $\mathbf{e} = \mathbf{e}_r \cos\psi + \mathbf{e}_z \sin\psi$ and $\mathbf{n} = -\mathbf{e}_r \sin\psi + \mathbf{e}_z \cos\psi$. The angle of incidence of the ray L is i (Fig. 2).

The coefficients of reflection for a wave with electric vector $\mathbf{E}$ in the plane of incidence and the direction perpendicular to this plane are [10]

$$R_1 = \frac{\tan^2(i-t)}{\tan^2(i+t)}, \quad R_2 = \frac{\sin^2(i-t)}{\sin^2(i+t)}, \tag{10}$$

where

$$\frac{\sin i}{\sin t} = n, \quad t = \arcsin\left(\frac{\sin i}{n}\right). \tag{11}$$

The corresponding degree of polarization is

$$P = \frac{1}{\bar{R}}(R_1 - R_2), \tag{12}$$

$\bar{R} = \frac{1}{2}(R_1 + R_2)$, and the intensity of the light transmitted through the analyzer (polaroid) is

$$I_\varphi = \left[\frac{\bar{R}}{2} + (R_2 - R_1)\sin^2(\varphi_1 - \varphi)\right]\frac{1}{\rho^2}, \tag{13}$$

where $\tan\varphi_1 = x/y$ is the angle between the y axis and the direction of transmission of the polaroid.

The polarization isophotes are given by the expression

$$I_\varphi = C_i, \tag{14}$$

where C_i are constants.

The curves calculated using (13) and (14) are presented in Fig. 3, while those obtained using the Nikon-850 digital camera are shown in Fig. 4. The intensities of these isophotes are within 40–240 arbitrary units. The illumination intensities C_i (in arbitrary units) and the angles γ between the lines joining the points of intersection of the isophotes for various angles of the polaroid are summarized in the following table, together with the rms errors $\delta\gamma$ of the angle γ:

C_i	80	100	140	160
γ	87.7°	89.1°	88.3°	89.5°
$\delta\gamma$	1.5°	1.6°	1.8°	2.0°

As this table shows, the angle γ is close to 90° (and the rms errors are $\delta\gamma = 1.5°–2°$).

Ordinary measurements of the plane of polarization with three orientations of the polaroid have accuracies up to $\sim 10°$ [11]. Such errors are much greater than the values of $\delta\gamma$ obtained above. Consequently, the Nikon digital camera satisfies the requirements of polarization observations.

Apart from the errors associated with the possible sensitivity of CCD arrays to polarization, the quantity $\delta\gamma$ includes the effects of the primary objective of the telescope (LOMO-750), the ocular, and the adjustable objective of the Nikon-850 camera. The lenses of the ocular and camera objective have considerable curvatures, so that it would not be surprising if these elements introduced some linear polarization. Fortunately, the errors in the intersection of the polarization isophotes proved to be small. This may be due to the fact that the image was transmitted near the optical axis.

Finally, we note that some of the isophotes (Fig. 4) are quite irregular, since the coefficient of reflection depends strongly on the coordinates (due to the nonuniformity of the dielectric surface). However, this does not affect the intersections of the isophotes (as was noted above, relation (6) depends on neither I_0 nor I_p).

4. CONCLUSIONS

Our estimates show that a current with amplitude 10^{12} A can be formed by the motion of electrons with speeds $v = 10^7$ cm/s, a plasma density 10^8 cm^{-3}, and a ray cross section of $10^8 \times 10^8$ cm^2. The corresponding deviation of the plane of polarization is $v/c\,(\mathrm{rad}) = 3 \times 10^{-4} \times 57° = 0.02°$, which is far smaller than the accuracy of the measurements.

The coronal electron density decreases quite rapidly, so that $n = 10^5$ cm^{-3} at $r = 3R_\odot$ [12]. Consequently, the current velocity for the same current density in a heliospheric plasma sheet is 10^{10} cm/s, and the deviation of the polarization plane is $v/c = 1/3\text{rad} \sim 19°$. Such deviations can be measured by modern detectors. The density continues to decrease at larger distances. The corresponding increase in the current velocity is followed by a decrease in the degree of polarization, since the F corona begins to play a larger role. This hinders determination of the plane of polarization. For example, in the case of ordinary photometry, a mean error of 5% prevents measurement of the plane of polarization if the degree of polarization is less than 5%, i.e., at $r > 4R_\odot$. In other words, it is impossible to determine the plane of polarization using photographic methods at large distances, where the plasma densities are small.

The use of CCD arrays changes this situation. The high signal-to-noise ratios that are characteristic of these devices provide hope that it will be possible to measure the currents in heliospheric plasma sheets.

ACKNOWLEDGEMENTS

We are grateful to Prof. S. Koutchmy of the Paris Astrophysical Institute for his interest in this present work.

REFERENCES

1. S. Koutchmy and K. Schatten, Solar Phys. **17**, 117 (1971).
2. M. M. Molodensky, Solar Phys. **28**, 465 (1973).
3. A. K. Kishonkov and M. M. Molodensky, Solar Phys. **42**, 341 (1975).
4. S. Koutchmy, M. M. Molodensky, G. M. Nikol'skii, and B. P. Filippov, Astron. Zh. **70**, 563 (1993) [Astron. Rep. **37**, 286 (1993)].
5. E. D. Pak, I. S. Kim, *et al.*, Astron. Zh. **78**, 839 (2001).
6. G. W. Pneuman and R. A. Kopp, Solar Phys. **18**, 258 (1971).
7. S. Koutchmy, private communication (2001).
8. M. M. Molodensky and S. Koutchmy, in *Solar Jets and Coronal Plumes,* Ed. by G. Tan-Duc (ESA Publ. Div. ESTEC, Noordwijk, 1999), p. 317.
9. S. Koutchmy, M. M. Molodensky, L. I. Starkova, *et al.*, Pis'ma Astron. Zh. **23**, 939 (1997) [Astron. Lett. **23**, 818 (1997)].
10. M. Born and E. Wolf, *Principles of Optics*, 4th ed. (Pergamon Press, Oxford, 1969; Nauka, Moscow, 1973).
11. M. A. Vashakidze, *Proc. of the Res. of Solar Eclipse Sep. 21, 1941 Expedition* [in Russian] (Akad. Nauk SSSR, Moscow, 1941), p. 186.
12. C. W. Allen, *Astrophysical Quantities*, 3rd ed. (Athlone, London, 1973; Mir, Moscow, 1977).

Translated by Yu. Dumin